Changes in Extratropical Cyclone Dynamics in the North Atlantic in a Warming Climate

A Dissertation
Submitted in Partial Fulfillment of the
Requirements for the Degree of Doctor rerum naturalium (Dr. rer. nat.)

to the Department of Earth Sciences
of Freie Universität Berlin

by

Edgar Dolores Tesillos

Berlin, October 2022

Supervisor: Prof. Dr. Stephan Pfahl
Second examiner: Prof. Dr. Joaquim Pinto

Day of defense: 12.10.2022

Si me dijeran: pide un deseo
Preferiria un rabo de nube
Un torbellino en el suelo
Y una gran ira que sube
Un barredor de tristezas
Un aguacero en venganza
Que cuando escampe
Parezca nuestra esperanza...

Silvio Rodriguez,1980

Abstract

Extratropical cyclones are a major control of weather and climate in the mid-latitudes. Climate model simulations have been used to analyze the influence of global warming on extratropical cyclone dynamics. This study addresses the still open questions of whether cyclones will become more intense, what dynamic processes are responsible for these changes, and how this could impact the North Atlantic region.

This study investigates extratropical cyclone dynamics over the two periods 1990-2000 and 2091-2100 using the Community Earth System Model Large Ensemble (CESM-LE) dataset. We analyze the storm response in the extended winter and summer seasons in the North Atlantic (NA) region. A Lagrangian cyclone detection is used to analyze the occurrence and spatial distribution of storm tracks. The evolution of cyclonic structures in a warming climate is studied with cyclone-centered composites. Likewise, a potential vorticity (PV) perspective is adopted to study the changes in the cyclone wind field near the surface. A trajectory analysis illuminates the contribution of diabatic processes to future changes of cyclone-associated PV anomalies.

Firstly, through comparison with ERA-Interim reanalysis data, we find that the CESM-LE captures the current spatial distribution of intense cyclones adequately. Robust changes in cyclone occurrence and properties are found in the NA region for the end of the century. For instance, cyclone frequency decrease in a warming climate, whereas precipitation intensity increases. Projected intensity changes are generally small.

Secondly, the structure of those cyclones whose intensities fall within the 90^{th} percentile is studied via a composite analysis. Winter storm tracks of these most intense cyclones respond to climate warming with an eastward shift. This shift increases the risk of strong winds and extreme precipitation in western Europe. In winter, extratropical cyclones also exhibit structural changes that amplify precipitation intensity downstream and low-level wind flow to the southeast of the cyclone center.

In present-day climate, PV inversion reveals the relevance of upper-level PV anomalies for contributing to the poleward wind flow to the east of the cyclone center. The simulated future intensification of this poleward flow is related to a strengthening of the low-level PV anomaly associated with amplified diabatic heating in combination with a dipole change in the upper-level PV anomaly pattern.

Furthermore, a Lagrangian trajectory analysis is adopted to explicitly identify changes in air mass advection that result in the PV anomalies at lower and upper levels. At upper levels, the decreased PV anomaly to the south of the cyclone center results from a combined effect of a decreased climatological PV in the NA region and a shift in the origin of the air masses. Increased diabatic heating along backward trajectories leads to an amplification of positive PV anomalies near the cyclone center at both lower and upper levels.

Finally, a scaling method is used to analyze the dynamic and thermodynamic contributions to cyclone-related precipitation changes on a storm-scale for the 10% most intense cyclones. Thermodynamic contributions dominate the precipitation increase over the coma-shaped main area of precipitation, while changes in the vertical wind (dynamic) contribute to enhanced frontal precipitation and a weakening of the precipitation to the west of the cyclone center.

In conclusion, diabatic processes, specifically enhanced latent heat release, will primarily shape the anatomy of intense extratropical cyclones in the North Atlantic region in a warming climate. Therefore, a better representation of the diabatic process in climate simulations can help to constrain better the future dynamics of intense cyclones and their social impacts.

Contents

1 Introduction

1.1 Present-day and projected future changes of the mid-latitude cyclones

Extratropical cyclones develop under conditions of baroclinic instability (Charney, 1947, Hoskins and Valdes, 1990, Catto, 2016, Schultz et al., 2019). This is a fluid dynamical instability generated in rotating stratified fluids. Thus, a strong horizontal temperature gradient and the planetary rotation are necessary to generate baroclinic instability (Holton and Hakim, 2012). The difference in solar heating between the equator and the poles produces a strong temperature gradient in the midlatitudes. Once the potential energy stored in the midlatitudes has been converted into kinetic energy by baroclinic instability, it will then grow up longitudinally until it creates trains of cyclones and anticyclones (Catto, 2016, Shaw et al., 2016). Baroclinic growth means the interaction of two layers (counterpropagating Rossby Waves), one at the surface and the other at upper levels (Catto, 2016).

Extratropical or mid-latitude cyclones strongly modulate weather and climate in the mid-latitudes (Chang et al., 2002, Hoskins and Hodges, 2002, Hawcroft et al., 2012, Pfahl and Wernli, 2012, Tamarin-Brodsky and Kaspi, 2017). For example, as the cyclones control cloud amounts, they regulate the radiation received by the extratropics. Besides, the cyclones transport heat and moisture poleward, an essential part of the global atmospheric circulation. Storm tracks are the areas where extratropical cyclones are most likely to form, propagate, dissipate, as well as contribute the most energy and momentum transport (Chang et al., 2002, Shaw et al., 2016). The storm tracks in each hemisphere generally reach their maximum in eddy kinetic energy during the winter season when the equator-to-pole temperature gradients are strongest (Chang et al., 2002).

Extratropical cyclones passing across the midlatitudes generate specific weather conditions (Catto, 2016). Cyclones and associated fronts produce locally up to 90% of annually accumulated precipitation (Catto et al., 2012, Hawcroft et al., 2012) and also contribute significantly to extreme precipitation events (Catto and Pfahl, 2013, Pfahl et al., 2014, Martius et al., 2016).

In addition, cyclones can lead to the formation of strong winds (Browning, 2004, Leckebusch et al., 2006, Priestley and Catto, 2022). The economic losses due to these winds have been shown to scale approximately with the third power of the near-surface wind speed (Klawa and Ulbrich, 2003, Roberts et al., 2014). The strongest near-surface winds typically occur in the dry intrusion region behind the cold front and the cold conveyor belt, sometimes associated with sting jets (Clark and Gray, 2018), as well as in the warm region to the south-east of the storm center, ahead of the cold front (Hewson and Neu, 2015, Slater et al., 2017). Laurila et al. (2021) found that the strongest winds move from the warm sector to behind the cold front during the cyclone intensification and the

maximum occurs almost at the same time as the minimum value of MSLP.

Several conceptual models have been developed to describe cyclone types and structures, such as the Norwegian cyclone model (Bjerknes, 1919) and the Shapiro and Keyser (1990) conceptual model. A distinctive difference between these two models is that the Shapiro–Keyser model substitutes the occlusion process with the frontal T-bone structure (warm and cold fronts become aligned perpendicular to each other) and only in the late stages of cyclone lifecycle, some narrowing of the warm sector is depicted (Schultz et al., 2019). Airstreams linked to cyclones are described in a three-dimensional conceptual model that incorporates warm and cold conveyor belts (Browning, 1990, Wernli and Davies, 1997, Madonna et al., 2014). The relevance of the warm conveyor belt is described by Pfahl et al. (2014); they found that the cyclone precipitation can be mainly attributed to the WCB activity. A broader review of the cyclone airstreams is performed in section 1.3.

A helpful variable to analyze mid-latitude atmospheric dynamics and the development of cyclones is Potential Vorticity (PV) (e.g., Hoskins et al., 1985). PV is a conserved quantity under adiabatic conditions; its rate of change at a given location is then determined by advection. Any further changes can be attributed to the generation or destruction of PV by non-conservative processes, like diabatic processes (latent heating (LH) and radiative heating) and frictional forcing (Bluestein, 1992, Catto, 2016). A qualitative framework to understand the relation between PV and extratropical cyclone dynamics and the role of LH is through three anomalous components in the PV-associated cyclone circulation: a positive upper-tropospheric PV anomaly, a positive potential temperature anomaly at the surface, and a positive lower-tropospheric PV anomaly (Davis and Emanuel, 1991, Davis, 1992). Diabatic processes primarily generate the positive lower-tropospheric PV anomaly, in particular, latent heat release during cloud formation (Stoelinga, 1996, Ahmadi-Givi et al., 2004, Büeler and Pfahl, 2017), and this anomaly can thus be regarded as a proxy for the influence of such diabatic processes on cyclone dynamics. Lower-tropospheric PV anomalies are dominant factors in the development of many intense cyclones (Dacre and Gray, 2013, Willison et al., 2013, Büeler and Pfahl, 2017, Catto et al., 2019). The relative contributions of these anomalies to the wind field and the cyclone intensity can be determined by applying PV inversion techniques (Davis and Emanuel, 1991, Davis, 1992, McTaggart-Cowan et al., 2003, Tochimoto and Niino, 2016, Flaounas et al., 2021). A further review of the cyclone evolution base on PV thinking is presented in section 1.2.

The ability of climate models to capture mid-latitude cyclone development, occurrence and structure has been investigated in previous studies (e.g., Catto et al., 2010, 2015, Hawcroft et al., 2016). For instance, Hawcroft et al. (2016) found that the climate model HiGEM overestimates the precipitation of intense cyclones in comparison with the ERA-Interim reanalysis and the Global Precipitation Climatology Project (GPCP) dataset. An equatorward bias of the storm tracks and underestimation of cyclone intensity in both hemispheres is found in CMIP3 and CMIP5 models (Chang et al., 2012, 2013).

Anthropogenic climate change is expected to lead to changes also in the spatial distribu-

tion and properties of extratropical cyclones. Projections from climate models have been analyzed to identify such cyclone changes in a warming climate (Pinto et al., 2009, Ulbrich et al., 2009, Pinto et al., 2013, Zappa et al., 2013, Tamarin-Brodsky and Kaspi, 2017, Day et al., 2018, Raible et al., 2018, Sinclair et al., 2020, Brogli et al., 2021, Reboita et al., 2021). While future changes in the North Pacific and, in particular, the Southern Ocean are, to first order, characterized by a poleward shift of storm tracks (O'Gorman, 2010), the pattern of projected changes in the North Atlantic region is more complex (Ulbrich et al., 2009, Zappa et al., 2013). Another region of high uncertainties is the Artic (Sepp and Jaagus, 2011, Day et al., 2018).

Such changes in the spatial distribution and intensity of cyclones are thought to result from a "tug of war" (Shaw et al., 2016) between different processes, such as changes in horizontal temperature gradients and baroclinicity, vertical stability, tropopause height and latent heat release (O'Gorman and Schneider, 2008, IPCC, 2014, Pfahl et al., 2015). In particular, the increase in atmospheric moisture content in a warming climate results in an increase also of latent heat release and, therefore, might intensify cyclones. It has been shown using the aquaplanet General Circulation Model (GCM) that a stronger SST gradient in the midlatitudes generally leads to stronger storm tracks that are shifted slightly poleward (Brayshaw et al., 2008). Besides, idealized simulations show more favourable background conditions for the growth of planetary-scale waves via planetary-scale baroclinic instability under a polar amplification (Moon et al., 2022). Such a potential intensification may, however, be compensated by other factors such as an increase in static stability (which is also linked to the moisture increase, in particular in lower latitudes where the atmospheric stratification is closer to a moist adiabatic) (Mbengue and Schneider, 2013, Catto et al., 2019). Additionally to the changes in the spatial distribution of storm tracks, the amplitude of the seasonal cyclone of storm tracks intensity is also projected to increase (O'Gorman, 2010).

One way to identify the influence of altered LH on cyclone dynamics is via the PV framework. As the PV anomaly in the lower troposphere is primarily related to diabatic processes, increased LH is expected to result in an intensification of this anomaly. Accordingly, an increase in lower-tropospheric PV in midlatitude cyclones has been detected in idealized model simulations (Pfahl et al., 2015, Büeler and Pfahl, 2019, Sinclair et al., 2020) and climate change studies with regional models (Marciano et al., 2015, Michaelis et al., 2017, Zhang and Colle, 2018). In the latter, high-resolution models, the relevance of the diabatic processes during cyclone intensification in a warmer climate is more evident. Tamarin and Kaspi (2017) and Tamarin-Brodsky and Kaspi (2017), using PV inversion, showed that such diabatically induced low-level PV increases contribute to an enhanced poleward motion of cyclones as the climate warms. Therefore, increased atmospheric water vapour and stronger upper-level winds are linked to the poleward propagation in a warmer climate (Tamarin-Brodsky and Kaspi, 2017). Nevertheless, it is not clear how (diabatic) PV changes link to structural changes in other impact-relevant cyclone properties such as low-level wind velocity (Marciano et al., 2015). This is one of the central questions of the present study.

Generally, there is a decrease in extratropical cyclone intensity projected in the Northern Hemisphere as the climate warms, which reduces the wind hazards associated with extratropical cyclones (Chang et al., 2012, Zappa et al., 2013, Li et al., 2014, Kar-Man Chang, 2018, Catto et al., 2019). Nevertheless, there may still be specific regions in the mid-latitudes that will experience an increase in wind hazards (Gastineau and Soden, 2009), such as central and western Europe (Pinto et al., 2007, Donat et al., 2010, Mölter et al., 2016). In addition, uncertainty in such estimated wind changes arises from the fact that global climate models cannot explicitly represent high wind-producing mesoscale circulation structures such as sting jets (Martínez-Alvarado et al., 2018).

Furthermore, a deviation from the general weakening tendency has been found for extreme cyclones, whose frequency may also increase (Hawcroft et al., 2018), with a more evident signal for western parts of central Europe (Leckebusch and Ulbrich, 2004, Leckebusch et al., 2006). This signal also varies between seasons, for example, more severe Autumn storms may reach Europe as the planet warms (Baatsen et al., 2015). Previous studies have also shown a reduction of Vb cyclones, which have a high impact over the Mediterranean region (Messmer et al., 2020).

Other effects of extreme cyclones in a warming climate are related to storm surges (Lin et al., 2019) and extreme coastal erosion (Harley et al., 2017).

Whereas the storm track activity response has been extensively explored in previous studies, there are larger uncertainties about changes in cyclone structure in a warmer climate (Catto et al., 2019, Sinclair et al., 2020). Information on structural changes in extratropical cyclone winds and other properties can be obtained with the help of composite analyses (e.g., Bengtsson et al., 2009, Catto et al., 2010, Dacre et al., 2012, Yettella and Kay, 2017, Pinto and Ludwig, 2020). Structural changes to precipitation distribution have been identified, with the heaviest precipitation concentrated near the center and to the east of the cyclone intensifying in a warmer climate (Yettella and Kay, 2017, Catto et al., 2019). The largest precipitation increase is observed in summer in the Northern Hemisphere, which suggests a significant role of thermodynamics in the cyclone-precipitation response (Yettella and Kay, 2017).

With respect to structural changes in the wind pattern associated with cyclones, idealized modelling experiments point to a broadening of the cyclones' strong wind footprint (Sinclair et al., 2020). In contrast, composite changes from other regional model studies are relatively noisy (Michaelis et al., 2017), which might be partially related to limited statistics. Here this will be addressed with the help of extensive ensemble simulations providing multiple samples also of intense and extreme North Atlantic cyclones and their future changes.

Uncertainties in cyclone intensity changes in the North Atlantic are attributed to the relatively coarse spatial resolution of climate models (Willison et al., 2015, Seiler et al., 2018). For instance, this limited resolution limits the ability of models to capture various factors that may influence future extratropical cyclone changes along the United States

(US) East Coast and western Atlantic (Colle et al., 2015), such as the Atlantic storm track sensitivity to the Gulf Stream SST gradient, latent heating within these storms, and dynamical interactions at the jet level. Other studies suggest that orography plays an important role in the equatorward bias and the zonal orientation of the North Atlantic storm track in climate models. Improved parameterizations of low-level drag may be a solution to this inaccuracy (Pithan et al., 2016).

1.2 Potential vorticity framework

An important variable to analyze mid-latitude atmospheric dynamics is the PV (e.g., Hoskins et al., 1985). Ertel's PV, in Cartesian coordinates, is defined as

$$q = \frac{1}{\rho}\vec{\eta} \cdot \nabla\theta \tag{1}$$

where $\vec{\eta}$ is the three-dimensional absolute vorticity vector, ρ is the air density, θ is potential temperature, and ∇ is the three-dimensional Nabla operator. Using isentropic coordinates and assuming hydrostatic balance, Eq. 1 can be expressed as

$$q = -g(\zeta_\theta + f)\frac{\partial\theta}{\partial p} \tag{2}$$

where $\zeta_\theta = \left(\frac{\partial v}{\partial x} - \frac{\delta u}{\partial y}\right)_\theta$ is the vertical component of relative vorticity, f is the Coriolis parameter and $\frac{\partial\theta}{\partial p}$ is the lapse rate of potential temperature.

Following the motion, PV is conserved under adiabatic and frictionless conditions. Thus, if one parameter in Eq. 2 changes, then the others must adjust. It is called PV because there is the "potential" for generating vorticity by changing latitude or stability. Since $\frac{\partial\theta}{\partial p}$ is negative for synoptic-scale motions, PV is positive in the northern hemisphere and negative in the southern hemisphere. PV is generally counted in the PV unit (PVU), where 1 PVU $= -10^{-6} m^2 s^{-1}$.

Some implications of PV conservartions are shown in Fig. 1.1. For instance, in Fig. 1.1a, if we keep the latitude fixed, convergence (divergence) will lead to a change of relative vorticity ζ_θ and thus a change in stability $\frac{\partial\theta}{\partial p}$. But if we keep stability constant, parcels changing latitude will lead to a change of f and absolute vorticity and thus a change of relative vorticity ζ_θ. Thus, under constant stability, parcels moving south (north) will experience an increase (decrease) in relative vorticity (Fig. 1.1b). Moreover, under constant relative vorticity, parcels moving south (north) will experience an increase (decrease) in stability.

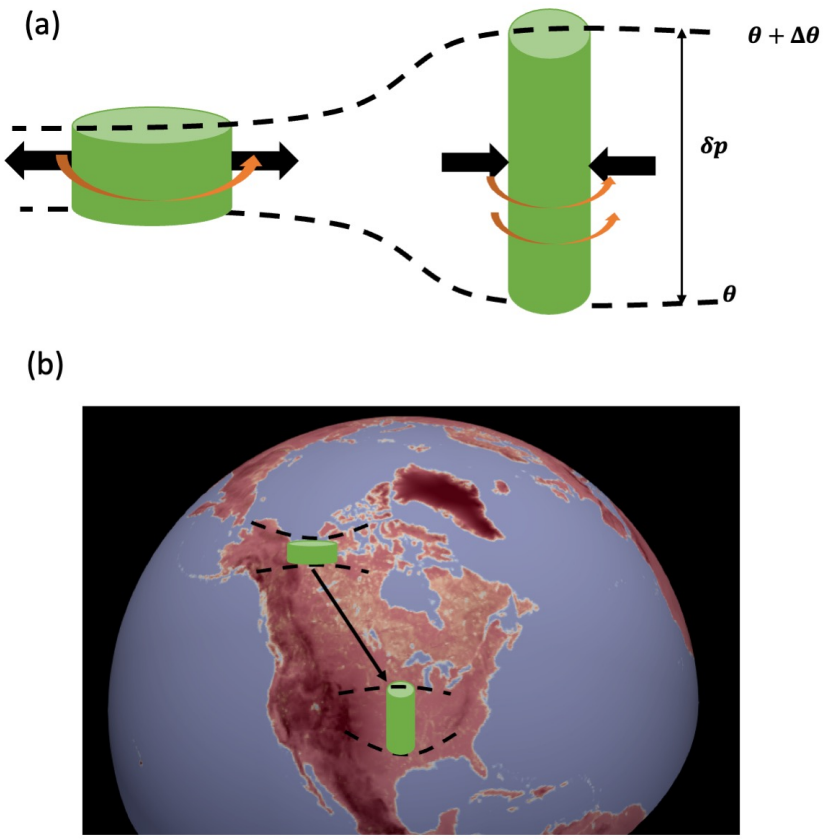

Figure 1.1: Air moving adiabatically between potential temperature surfaces (θ and $\theta + \Delta\theta$), separated by a pressure interval δP and conserving potential vorticity.

Another property of the PV is its invertibility. This property refers to the fact that if the distribution of PV (x,y,p) is known, we can infer about the distribution of other variables such as θ, u, v. However, we need to know more than just the PV distribution to compute the above parameters. Thus, PV inversion has to follow some conditions (Bluestein, 1992):

1. The distribution of PV is known.
2. θ on the domain boundaries is defined.
3. A balance condition can be applied that relates the mass and momentum fields within the domain (e.g., geostrophic or gradient balance).

A common balance condition for the study of the cyclone dynamics is to consider the smallness of the irrotational wind (e.g., Davis, 1992). The horizontal velocity field is written in terms of the Helmholtz decomposition.

$$\vec{V} = \vec{V}_\psi + \vec{V}_\chi = -\hat{k} \times \vec{\nabla}\psi + \vec{\nabla}\chi \tag{3}$$

Where $\vec{V}_\psi$ is called the nondivergent component and $\vec{V}_\chi$ the irrotational component. $\hat{k}$ is the unit vector in the vertical, ψ is the streamfuntion and χ the velocity potential. The nondivergent component describes swirling flow (divergence free). In contrast, the irrotational component refers to purely divergent flow (vorticity free).

The spatial distribution of PV and potential temperature allow us to identify the tropospheric structure (e.g., Fig. 1.2). In mid-latitudes, a value of 2 PVU is usually applied to define the dynamical tropopause. Values of PV < 2 PVU are generally linked with tropospheric air, and values of PV > 2 PVU are generally linked with stratospheric air. Fig. 1.2 shows that the pressure of the 350 K isentrope varies little with latitude, although it is located in the stratosphere at high latitudes and in the troposphere at low latitudes. The 300 K isentropic surface slopes abruptly and is usually located in the troposphere.

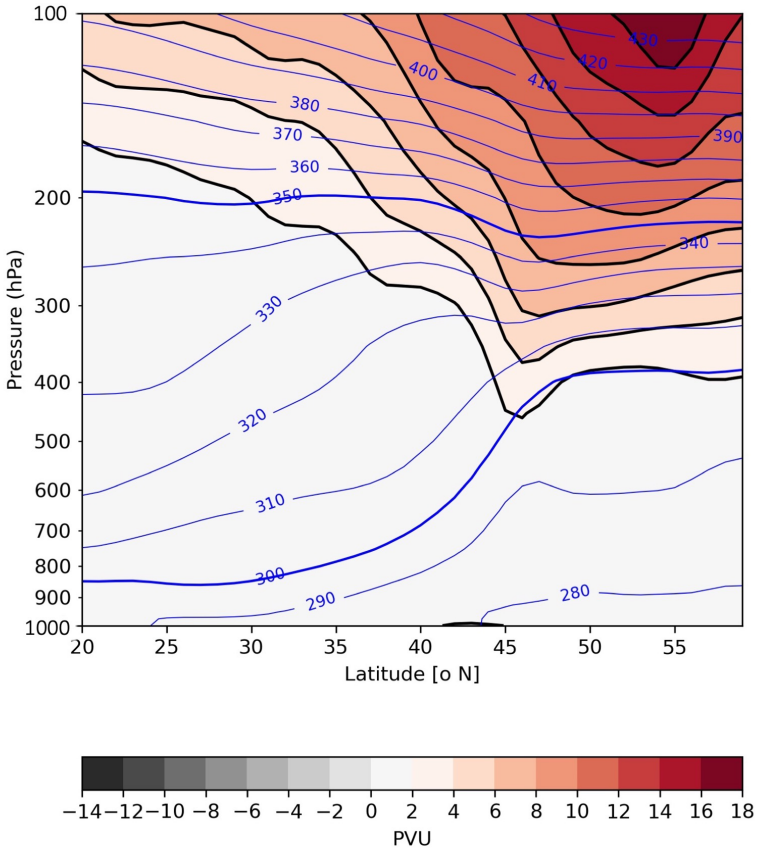

Figure 1.2: Latitude-pressure cross-section of PV (shading) and potential temperature (blue contours) at 226 W for 06Z 08 April 2022.

PV anomalies can be obtained as deviation from a climatological mean PV distribution (e.g., Davis and Emanuel, 1991, Davis, 1992, Steinfeld, 2019). Fig. 1.3 shows the thermal

structure and wind response to PV anomalies in the upper troposphere. A positive PV anomaly is associated with cyclonic wind and has isentropic surfaces that bow towards the anomaly in the troposphere and stratosphere. Thus, they are related to increased static stability. A negative PV anomaly is associated with anticyclonic wind and has isentropic surfaces that bow away from the anomaly in the troposphere and the stratosphere. Thus, they are related to decreased static stability.

Therefore, steep gradients in PV are associated with jets, steep stability gradients, and tropopause folds. Upper-level PV anomalies will tend to propagate westward, as long waves do through advection of planetary vorticity (f).

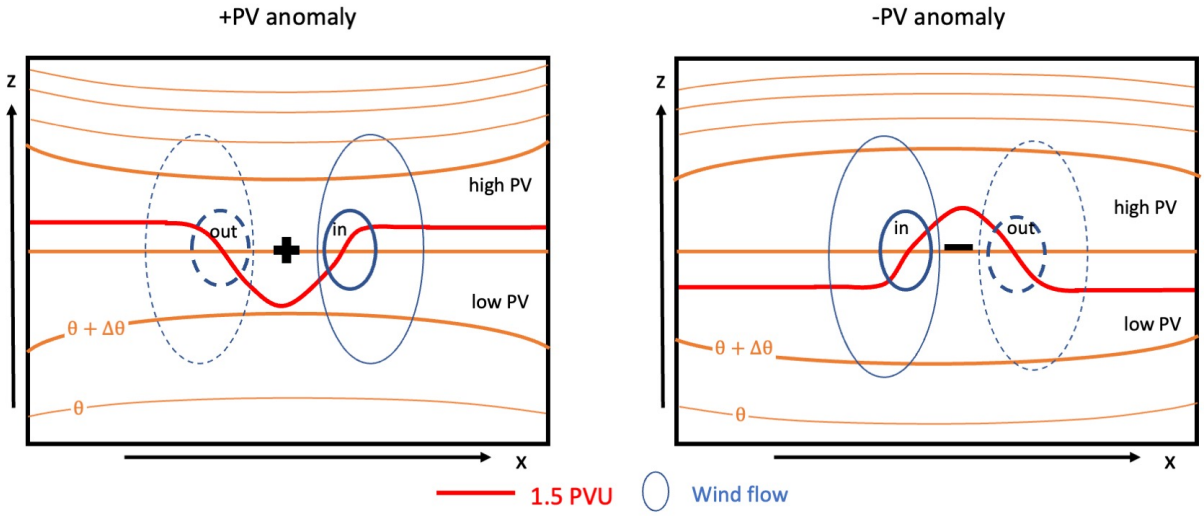

Figure 1.3: PV anomalies, thermal structure and wind flow.

PV anomalies are also found in the lower troposphere. Moreover, a warm temperature anomaly at the lower boundary behaves like a positive PV anomaly. The associated cyclonic circulation produces southerly winds downstream of the positive PV anomaly; thus, they are linked with warm advection. While northerly winds upstream of the positive PV anomaly are associated with cold advection. The disturbance has a net effect of propagating eastward.

From the PV perspective, the development of cyclones depends on a prolonged period of mutual amplification of upper and lower level PV anomalies. However, we know that upper-level PV anomalies and lower level PV anomalies propagate like Rossby waves in opposite directions. Thus, how does cyclogenesis occur in the PV thinking? We describe the cyclogenesis using the PV perspective in the following.

As a first stage, we can consider an upper tropospheric +PV anomaly travelling over a baroclinic surface zone (Fig. 1.4). The upper-level anomaly has a cyclonic wind anomaly

and extends throughout some depth of the troposphere. The influence of the upper-level +PV anomaly is to deform the sea level circulation through horizontal temperature advection.

In the second stage, the warm air advection acts on the surface isentropes to create a warm anomaly; this anomaly creates a circulation that penetrates the tropopause. The warm surface anomaly will have a reflection on the upper levels (e.g., 300 hPa) field by inducing a cyclonic circulation that will strengthen the +PV anomaly through equatorward +PV advection on the east side of the PV anomaly. This will cause the upper PV anomaly to propagate eastward, contrary to its inclination to propagate westward.

Thereafter, the invigorated upper-level anomaly exerts an invigorated influence on the low-level isentrope field. Since the upper-level +PV anomaly lies upstream of the surface warm anomaly, this maximizes thermal advection where the maxima in warm anomalies already exist. Thus, the upper level +PV-induced warm and cold advection aid in strengthening the lower level +PV feature and acts together to allow the PV to propagate eastward.

Thus, when the upper and lower PV anomalies are nearby, they can be mutually amplified and have a "phase locking", which allows them to propagate together. Upshear (westward) tilt of the cyclone with height is a requisite condition for this process to occur. Thus it is beneficial for systems to have upshear tilt for maximum intensification (Fig. 1.4).

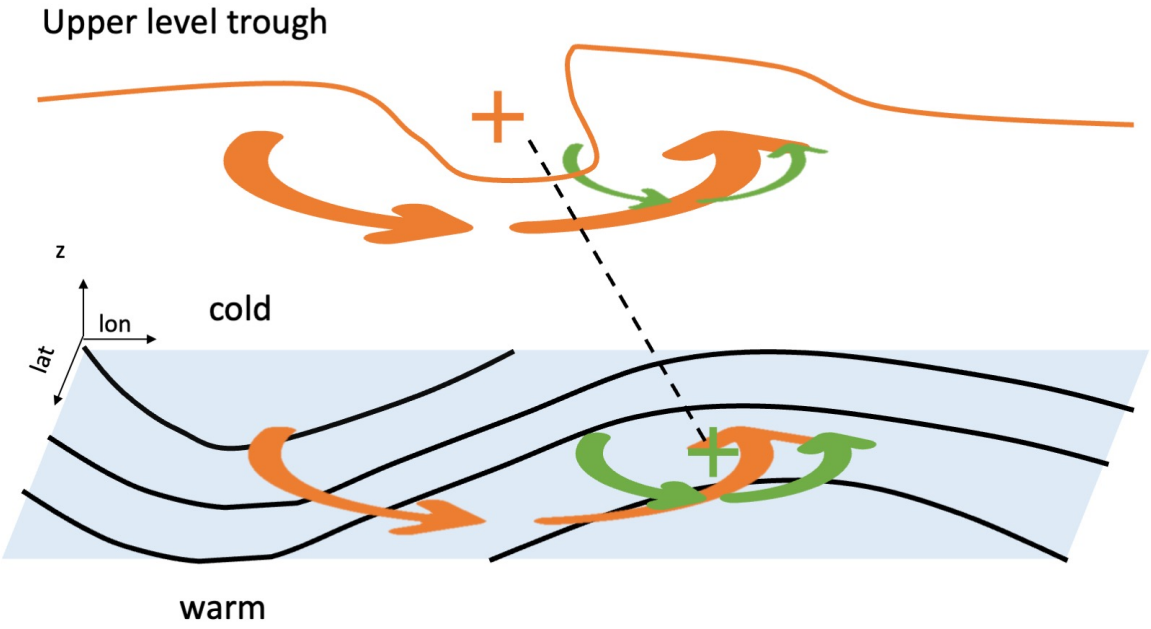

.

Figure 1.4: Interaction of upper and lower PV anomalies for cyclogenesis in a dry atmosphere. Adapted from Colle et al. (2015)

The evolution of PV following the horizontal motion on isentropic surface can be derived from Eq. 2 (Holton and Hakim, 2012):

$$\frac{\tilde{D}q}{Dt} = \frac{\partial q}{\partial t} + V \cdot \nabla_\theta q = \frac{q}{\sigma}\frac{\partial}{\partial \theta}(\sigma\dot{\theta}) + \sigma^{-1}k \cdot \nabla_\theta \times \left(F_r - \dot{\theta}\frac{\partial V}{\partial \theta}\right) \tag{4}$$

where $\dot{\theta}$ denotes the time derivative of the potential temperature, F is the three-dimensional frictional force per unit mass, and $\sigma = -g\frac{\partial p}{\partial \theta}$.

Here, it is shown that PV changes can be attributed to diabatic ($\dot{\theta} \neq 0$) and frictional processes ($F \neq 0$). The generation of PV anomalies is generally driven by different processes depending on the atmospheric level (Büeler and Pfahl, 2017):

1. Upper-level PV anomalies are due primarily to differential advection (separation from a PV reservoir).
2. Lower level PV anomalies can be created by:
   - Differential diabatic heating (e.g., cloud and precipitation processes in extratropical cyclones)
   - Friction (this includes orography, e.g., lee cyclogenesis).

Neglecting the friction term and considering only the vertical component, Eq. 4 can be expressed on pressure levels:

$$\frac{D}{Dt}(q) \equiv -g(\zeta + f)\frac{\partial \dot{\theta}}{\partial p} \tag{5}$$

PV is increased (decreased), where the vertical gradient of diabatic heating is positive (negative). Diabatic heating in the mid-troposphere causes PV destruction in the upper troposphere and PV creation in the lower troposphere (Fig. 1.5).

Thus, the diabatic processes may change the magnitude of the PV anomalies associated with the cyclone evolution. A PV diagnostic equation has been developed by Büeler and Pfahl (2017) to quantify the fraction of the lower-tropospheric PV anomaly in an extratropical cyclone that results from latent heat (LH) due to cloud-condensational processes:

$$\langle q_{diab}(z)\rangle_{effarea} = \int_{z_1}^{z} \left\langle \frac{1}{\rho}\left(\eta_x\frac{\partial \dot{\theta}}{\partial x} + \eta_y\frac{\partial \dot{\theta}}{\partial y} + \eta_z\frac{\partial \dot{\theta}}{\partial z}\right)\frac{1}{w}dz \right\rangle_{w \geq W, effarea} \tag{6}$$

where $q_{diab}(z)$ is the diabatic PV, ρ is the density, η_x, η_y and η_z are the x, y, and z components of the absolute vorticiy, $\dot{\theta}$ is the potential temperature tendency, and w is the vertical wind velocity (for more details see: Büeler and Pfahl, 2017, 2019)

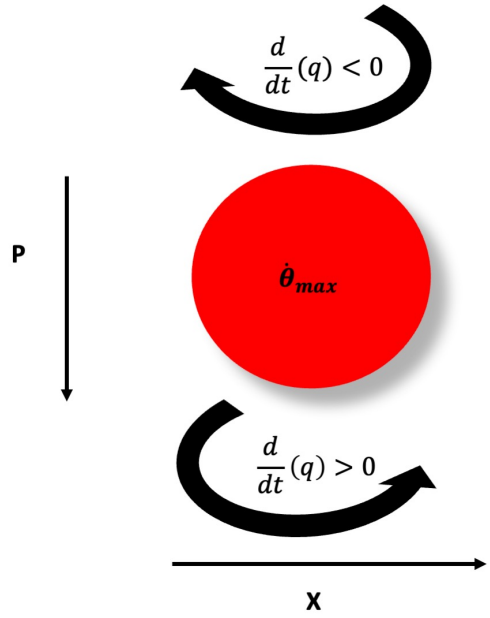

Figure 1.5: PV anomalies driven by diabatic procces at mid levels. Adapted from Martin (2006).

LH release is usually linked to ascent downstream of a positive PV anomaly (Wernli et al., 2002, Madonna et al., 2014). The influence of the diabatic process in the cyclone intensification can be summarized by level (Bluestein, 1992, Grams et al., 2011, Büeler and Pfahl, 2017):

1. Weaken upper tropospheric PV (PV destruction).
    - Steepen the PV gradient downstream of the positive PV anomaly
    - Shorten the wavelenght between the trough and downstream ridge
    - Increase height gradient
    - Strengthen upper level jet
2. Enhance lower tropospheric PV (PV generation).
    - Enhance "phase lock" stage.
    - Reduce static stability in low levels.
    - Intensification of cyclone (Fig. 1.6).

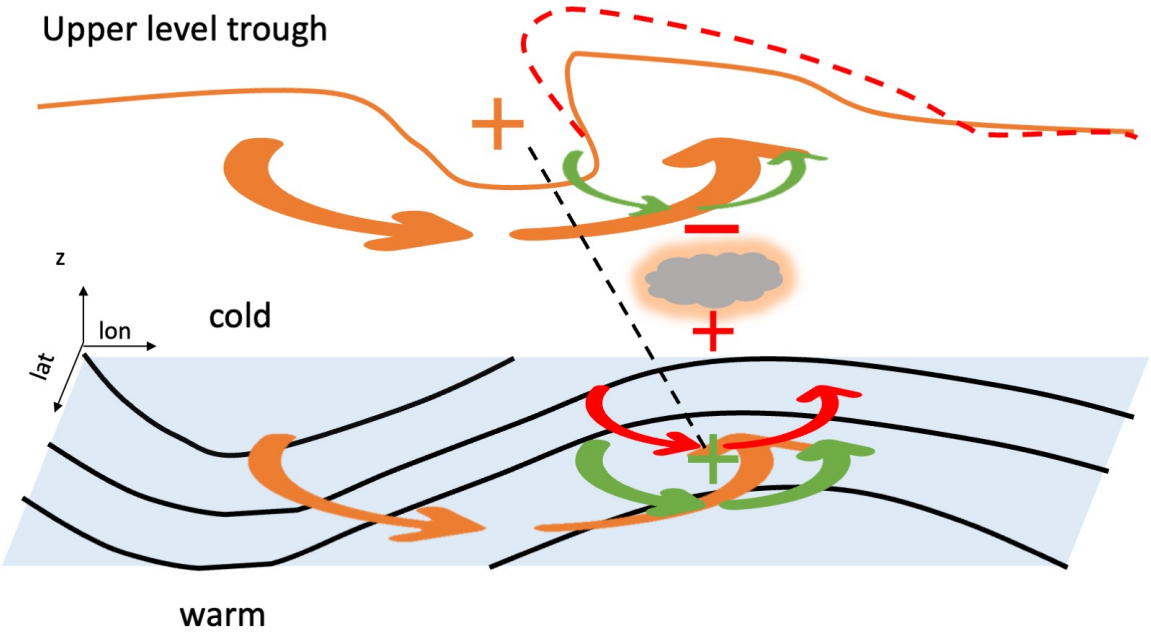

Figure 1.6: Interaction of upper and lower PV anomalies for cyclogenesis in a moist atmosphere. Adapted from Colle et al. (2015)

1.3 Extratropical cyclone airstreams

By analysing the system relative flow on isentropic surfaces around mid-latitude the cyclones, the presence of three different airstreams is evident: the warm conveyor belt (WCB), the dry intrusion (DI) and the cold conveyor belt (CCB) (Harrold, 1973, Carlson, 1980, Browning, 1986, Madonna et al., 2014). Fig. 1.7 shows the region and the typical trajectory of these airstreams.

WCBs are trajectories of moist air parcels near the surface ahead of cold fronts that experience rapid slantwise ascent with latent heat release (Shaw et al., 2016). The WCB represent the most important flow for the generation of clouds and precipitation in extratropical cyclones (Madonna et al., 2014), and it plays a crucial role for extreme precipitation events in the mid-to-high latitudes (Pfahl and Wernli, 2012). In the Northern Hemisphere, WCBs are more frequent in winter than in summer, with two preferential regions of ascent in the western North Atlantic and North Pacific (Binder et al., 2016, Madonna et al., 2014). PV is typically strongly modified along WCB's by smaller scale, microphysical processes, such as condensation of water vapour at low levels and depositional growth of snow at upper levels (Binder et al., 2016).

WCBs influence the tropospheric PV distribution in different ways. Before the ascent, the

airstreams, on average, have relatively low PV, followed by a steep PV increase during the first part of the ascent and a decrease in the second part. In the post-ascent phase, some trajectories reach more than 2 PVU (Madonna et al., 2014). The intense WCB-related cloud-diabatic processes can produce a strong positive PV anomaly in the lower and middle troposphere. At upper levels, diabatic PV destruction leads to low PV values in the WCB outflow. These produce significant negative PV anomalies in the tropopause region, which can interact with the extratropical waveguide and thereby substantially influence the downstream flow (Binder et al., 2016). Additionally, this process may also influence the formation of atmospheric blocking downstream (Steinfeld and Pfahl, 2019). Dacre and Gray (2013) found that latent heat release in the warm conveyor belt region plays an essential role in the development of east Atlantic cyclones.

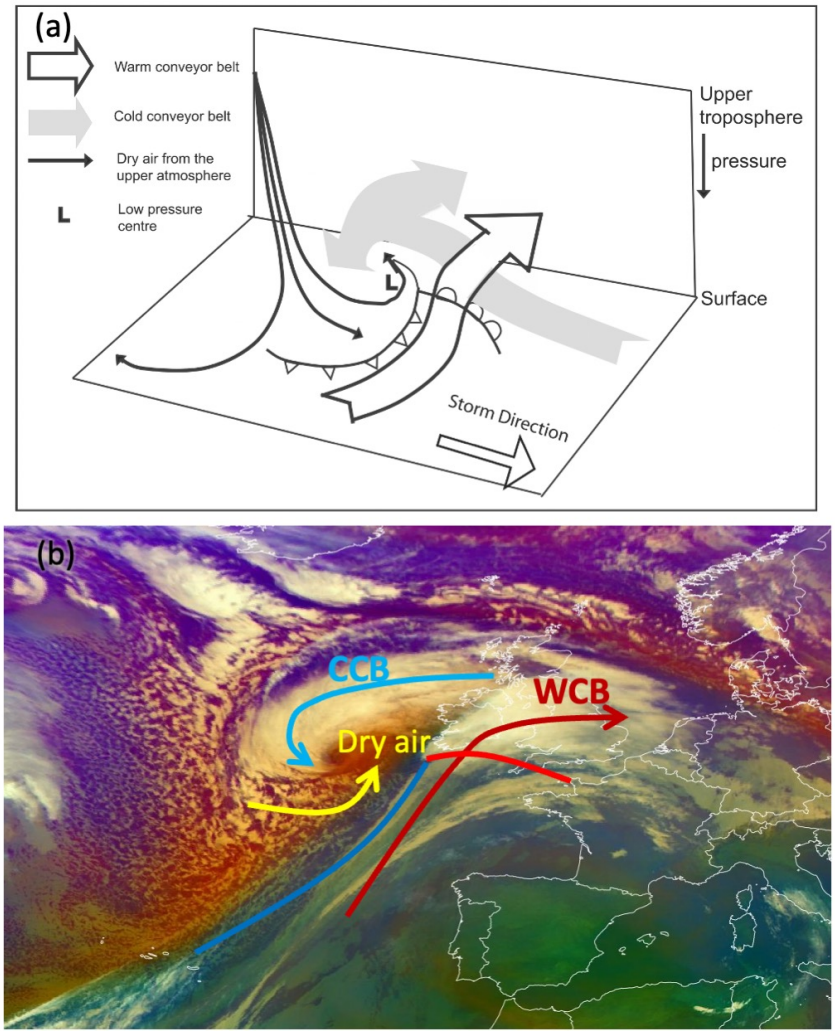

Figure 1.7: (a) Schematic illustration of warm conveyor belt (WCB), cold conveyor belt (CCB), and dry intrusion (DI) (taken from Catto, 2016). (b) Satellite image of the extratropical cyclone Eunice with airstream activity (Febraury 18, 2022, https://view.eumetsat.int/productviewer).

The CCB is characterised by a westward flow relative to the cyclone propagation at low levels parallel to and on the cold side of the warm front (Catto et al., 2010, Schemm and Wernli, 2014). Two branches are linked to the CCB; the main path slopes cyclonically at low levels around the cyclone center (Schultz, 2001). This branch is often related to strong low-level winds along the bent-back front forming a low-level jet (Schemm and Wernli, 2014). A second branch turns anticyclonically and ascends into the cloud head. Schultz (2001) mentioned that this branch represents a transition airstream between the WCB and the cyclonic branch of the CCB.

DIs are cold, dry airstreams descending behind the cyclone from the tropopause to middle and low levels (Browning, 1997, Catto et al., 2010, Raveh-Rubin, 2017). At lower levels, DIs tend to fan out cyclonically or anticyclonically. A cloud-free region is generated due to low moisture content (Catto et al., 2010, Raveh-Rubin, 2017), which can be identified in satellite images as "dry slots" with a hammer-head shape (Fig. 1.7b). The cyclonic descending flow might travel along the cold front and produce instability and potential for severe weather (Browning, 1997). Convection associated with the DIs is found in regions where they overrun moist air by releasing potential instability and favouring strong winds, precipitation and thunderstorms (e.g., Raveh-Rubin and Wernli, 2016). However, DIs can also weaken the WCB-rain band as the DIs underrun the northern part of the WCB and by evaporating precipitation from the cloud head (Raveh-Rubin, 2017).

1.4 Outline and aim of the Thesis

The intensity and position of storm tracks might respond to climate warming over the next century and affect mid-latitude weather extremes. In addition, several open questions remain with regard to structural changes in wind and precipitation patterns around cyclones and the underlying dynamical process that may cause such changes.

As we have discussed before, due to its conservation and invertibility properties, PV emerges as an important variable to investigate such dynamical changes in a warmer climate (e.g., Hoskins et al., 1985). Also, airstreams such as WCBs can modify the PV distribution, and their analysis may thus help explaining PV changes in cyclones in a warming climate. Thus, investigating the future position and evolution of the airstreams linked to extratropical cyclones is crucial to understanding changes in cyclone dynamics.

In this study, an analysis of extratropical cyclone dynamics over the North Atlantic is performed by using the Community Earth System Model Large Ensemble (CESM-LE) simulations, comparing two periods, 1990-2000 and 2091-2100. A PV framework and airstreams approach is adopted to analyze dynamical processes associated with altered wind and precipitation patterns around such cyclones. The objectives of this work are as follows.

Objectives:

A Identify the most significant projected changes of cyclone structure in CESM-LE simulations as the climate warms (Chapter 4).

B Evaluate the PV anomalies that modify the cyclone circulation and its intensity (Chapter 5).

C Adopting a Lagrangian perspective, investigate the impact of changes in diabatic processes in cyclone-related airstreams on the configuration of PV anomaly patterns (Chapter 6).

D Examine the dynamic contribution to projected future precipitation changes within cyclones (Chapter 7).

The content of this thesis is structured as follows. In Chapter 2, we describe the main methods and the CESM-LE dataset. Chapter 3 presents an evaluation and a review of storm track changes simulated in the CESM-LE. In Chapter 4, the changes in properties of intense cyclones are studied in more detail using composite analysis. In Chapter 5, a Piecewise Potential Vorticity Inversion (PPVI) technique is applied to extreme cyclones to investigate the associated wind changes. Chapter 6 provides a Lagrangian perspective of extreme cyclone changes in a warming climate. In Chapter 7, the dynamic and thermodynamic contributions to the precipitation change associated with intense cyclones are examined. Conclusions and outlook on future work are provided in Chapter 8.

Parts of the contents and figures of this thesis have already been published in the following article:

Dolores-Tesillos, E., Teubler, F., and Pfahl, S.: Future changes in North Atlantic winter cyclones in CESM-LE – Part 1: Cyclone intensity, potential vorticity anomalies, and horizontal wind speed, Weather Clim. Dynam., 3, 429–448, https://doi.org/10.5194/wcd-3-429-2022, 2022.

E.D.-T. contributed to the design of this study, performed the analysis, produced the figures, drafted the manuscript, discussed the results and edited the manuscript.

2 Data and methods

In this chapter, the data and main methods are described. Furthermore, a general review of the projected global mean temperature and precipitation change is presented and compared with previous studies to evaluate our dataset. Additional methods have been implemented to address more specific tasks and will be described in the following chapters.

2.1 Data

We use 6-hourly output from 10 members of the CESM-LE-ETH model ensemble, which were restarted from Community Earth System Model Large Ensemble (CESM-LE) simulations (Kay et al., 2015). The members differ by a small random perturbation to their initial air temperature field on the order of 10^{-14} K. Each member has a horizontal resolution of 0.94^o x 1.25^o, latitude and longitude, respectively. The vertical coordinate is a hybrid sigma-pressure system with 30 levels. Two periods are analyzed: 1990-2000 for the present-day climate and 2091-2100 for future climate. Historical forcing (Lamarque et al., 2010) was applied in the present-day period and Representative Concentration Pathway 8.5 (RCP8.5) forcing (Meinshausen et al., 2011, Lamarque et al., 2011) in the future period. The simulations have been re-run for these periods (using restart files from the original simulations) to obtain more comprehensive six-hourly output fields, such as vertical velocity on model levels. Note that the re-runs are not bit-identical to the original CESM-LE simulations. In the following, for simplicity, this dataset will be denoted as CESM-LE.

In order to perform a basic model evaluation and analyze the projected change in the mean climate, we selected 10 ensemble members to analyze the global mean temperature, horizontal wind and precipitation change. The motivation for this overview is to show how the environment in which cyclones develop might change, and to compare these mean changes with previous studies. The global average surface temperature of the members and for each study period is shown in Fig. 2.1, indicating an increase of temperature by about 5^o K.

Since baroclinic instability is the primary driver of extratropical cyclones, future changes in the horizontal temperature gradients in both the upper and lower troposphere, as well as changes to the vertical temperature gradients, will modify the storm tracks location and intensity (Tamarin and Kaspi, 2017, Catto et al., 2019). Hence, as a first step and basis for the subsequent analysis of cyclones, the zonal mean temperature is compared between the present and future analysis periods (Fig. 2.2a). Temperature is projected to increase in the entire troposphere. However, the largest changes are projected over the polar region and in the tropical upper troposphere, reducing the horizontal equator-polar gradient in the lower troposphere and enhancing the meridional temperature gradient at upper levels. In the Northern Hemisphere, the effect of the warmer upper tropical

atmosphere increases the baroclinicity and produces a poleward shift of storm tracks; however, the artic amplification (artic surface warming) decreases the baroclinicity and produces an equatorward shift (Shaw et al., 2016, Tamarin and Kaspi, 2017). In order words, the net effect is not evident. However, some researchers (e.g., Shaw et al., 2016) have mentioned that the poleward shift depends on the season and is less robust in the winter.

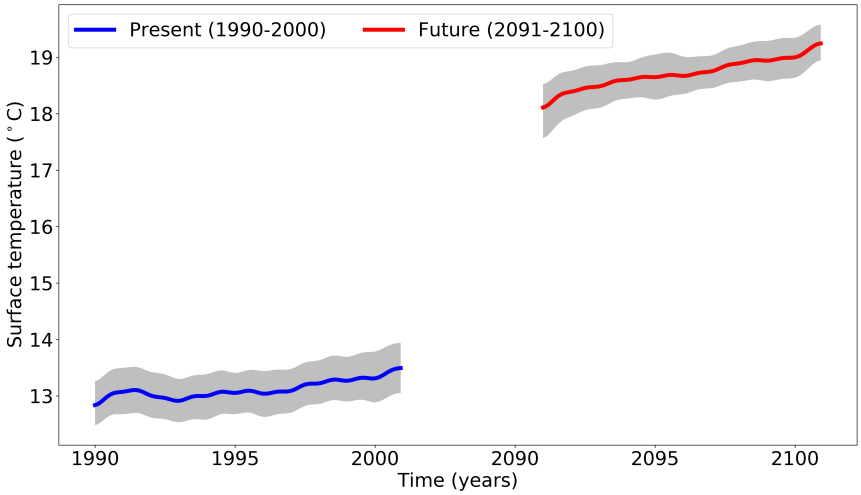

Figure 2.1: Time series of global surface temperature in two periods: 1990-2000 and 2091-2100. Ensemble mean and spread of ensemble members 1-10. Note that the x-axis is not continuous

The jet stream is related to meridional temperature gradients via the thermal wind balance, and influences the translation speed and direction of cyclones (Shaw et al., 2016). Therefore, future changes in jet speed are related to storm track changes. We review the jet stream changes through the zonal wind (Fig. 2.2b). We notice that the most robust changes are projected in the southern hemisphere, with the largest wind speed increases in the subtropics and mid-latitudes at upper levels. The jet stream moves upwards and slightly poleward; this poleward shift in the southern hemisphere as a result of climate change is consistent with previous studies (e.g., Tamarin and Kaspi, 2017). In contrast, there is no clear poleward shift in the northern hemisphere, which points out the necessity to further study this "tug of war" impact on the cyclone dynamic in a warming climate.

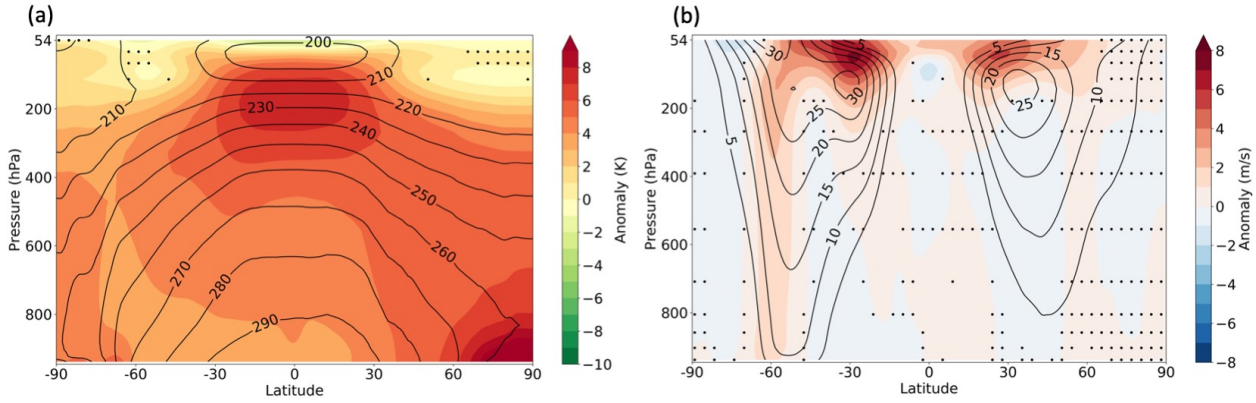

Figure 2.2: (a)Zonal mean temperature (present-day climate, contours, K) and response (future-present, colour shading, K). (b)Zonal mean wind speed (contours, K) and response (colour shading, K). Black dots denote regions of ensemble disagreement on the sign of change, i.e. less than 80% of the ensemble members indicate a change of the same sign. Periods: 1990-2000 and 2091-2100. Ensemble mean of members 1-10.

Climate warming is expected to go along with an increase in the atmospheric moisture content (to first order following the Clausius-Clapeyron equation) and thus with more precipitation (Sherwood et al., 2010). To analyze changes in mean precipitation, we have split the seasons between extended winter (October to March) and summer (April to September) (Fig. 2.3). The most significant precipitation increase is found over tropical and midlatitude areas (Fig. 2.3b and 2.3d). The latter is directly related to cyclones, as a substantial fraction of mid-latitude precipitation occurs in connection with these systems (Pfahl and Wernli, 2012, Yettella and Kay, 2017)

In winter, the precipitation increase is evident over most parts of the midlatitude. However, some European regions, such as the Iberian Peninsula and the Mediterranean region, will have less precipitation (Fig. 2.3a). On the other hand, in summer, the Atlantic basin and most of the European region will have less precipitation (Fig. 2.3c). A more significant reduction of precipitation is projected over the Iberian Peninsula and the Mediterranean region. These results show a seasonal and regional variability of the precipitation change in a warming climate.

The tendency of higher precipitation in the mid-latitudes and a consequent increase in latent heat release might enhance cyclone intensity in a future warming climate (Catto et al., 2019). This effect adds to the opposing influences of changes in the horizontal and vertical temperature gradients, which makes the prediction of the storm track response to future climate change very challenging (Shaw et al., 2016).

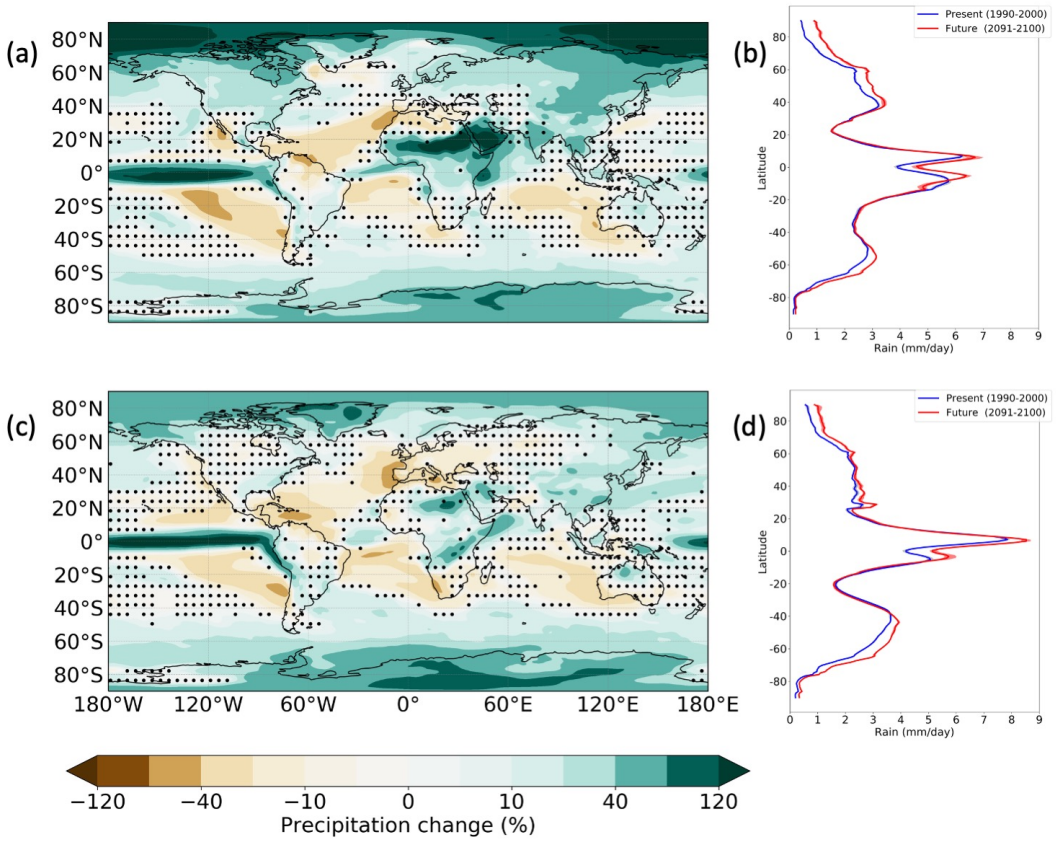

Figure 2.3: (a,c) Precipitation response (colour shading, %) and (b,d) Zonal mean precipitation (mm/hh) with spread of ensemble members 1-10 in the NH winter (c,d, October-March) and in the NH summer (a,b, April-September). Black dots denote regions of ensemble disagreement on the sign of change, i.e. less than 80% of the ensemble members indicate a change of the same sign. Periods: 1990-2000 and 2091-2100. Ensemble mean of members 1-10.

2.2 Cyclone identification and tracking

Cyclones are identified with an updated version of the sea-level pressure (SLP) contour method developed by Wernli and Schwierz (2006), as described in Sprenger et al. (2017) and illustrated exemplarily in Fig. 2.4. Cyclone centers are defined as local minima in the SLP field. Starting from every SLP minimum, closed isobars are identified at intervals of 0.5 hPa, and the outermost contour that does not exceed 7500 km in length is used as the outer boundary of the system. Cyclones that are close to each other (e.g., binary cyclones with two local SLP minima) are merged as long as the outermost closed contour's length does not exceed 7500 km, and only the deepest SLP minimum of each cyclone is kept and used for cyclone tracking. Successive SLP minima are connected to form a cyclone track if they occur within a specific search area determined by the previous cyclone trajectory.

As in Pfahl et al. (2015), only cyclone tracks are taken into account in the following with a minimum lifetime of 24h and an SLP difference of at least 1 hPa between the minimum and the outermost contour at each time step.

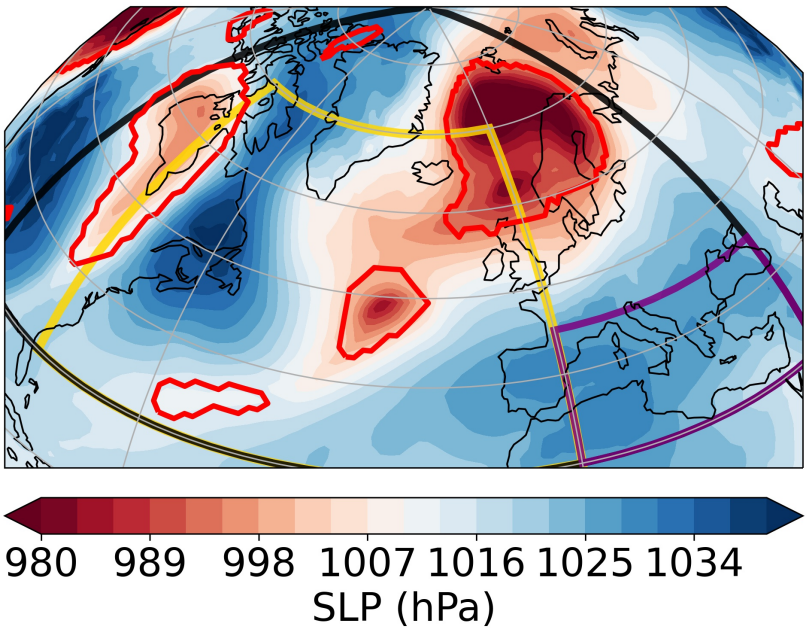

Figure 2.4: Example sea level pressure contouring method for one-time step. SLP (shading) and identified cyclones identified (red contours). The black box corresponds to the North Atlantic (NA) region, the yellow box to a sub-domain in the NA and the purple box to the Mediterranean region.

Following Neu et al. (2013) the track density is defined as the number of tracks passing a grid cell (with repeated entries of the same track being counted as one). Then, a regridding procedure is applied to project the trajectories onto a regular 1^o x 1^o grid, using a gridding tool developed by Škerlak (2014), spatially smoothed with a smoothing radius of R = 500 km.

In this study, we focus on analysing future cyclone changes over the North Atlantic region (longitude: -100° to 40° and latitude: 30° to 90°, black contour in Fig. 2.4), the sub-North Atlantic basin (longitude: -80 to 0 and latitude: 30 to 70, yellow contour in Fig. 2.4) and Mediterranean region (longitude: 0 to 40 and latitude: 30 to 45, purple contour in Fig. 2.4) for the extended boreal winter season (October-March) and extended boreal summmer season (April-September). We associate a cyclone track to the domain if it has at least one location inside the domain. Therefore, our analysis is based on more than 35,800 storms in the 11 winters and more than 40,800 storms in the 11 summers of present-day climate, and more than 30,800 storms in the 10 winters and more than 37,500 storms in the 10 summers of future climate, pooling the data from all 10 ensemble members.

3 Storm tracks over the North Atlantic in a Warming Climate

This section describes the climatology of storm tracks in the CESM-LE simulations compared to ERA-Interim data in both hemispheres. Subsequently, projected changes in storm tracks, cyclone intensity and cyclone precipitation in a warmer climate at the end of the century over the North Atlantic are presented for the warm and cold season.

3.1 Data and methods

ERA-Interim Reanalysis

To assess the ability of CESM-LE to simulate observed cyclone track density and statistics, the historical simulations (1990–2000) are compared with the ERA-Interim reanalysis (Dee et al., 2011) for the period 1979-2010.

3.2 Model evaluation

Figure 3.1 shows the storm track density from ERA-Interim for the Northern Hemisphere (extended winter: October to March and summer: April to September) and the Southern Hemisphere (extended winter: April to September and summer: October to March). In the Northern Hemisphere (NH), most of the cyclones are found over the North Atlantic, North Pacific and Eastern Asia. A region of high cyclone frequency extends from the east coast of the USA to northern Europe. The cyclone density maximum is located to the south of Greenland. The Mediterranean region is another area with enhanced cyclone activity. This storm track distribution is similar to previous studies (e.g. Wernli and Schwierz, 2006, Ulbrich et al., 2009, Neu et al., 2013, Zappa et al., 2013).

We can also observe a seasonal difference in the cyclone activity. For example, in winter, cyclone activity is larger over the North Atlantic and North Pacific and the Mediterranean. On the contrary, cyclones frequencies are higher in summer over Eastern Asia and the Iberian Peninsula (Fig 3.1a).

In the Southern Hemisphere (SH), the most considerable cyclone activity is between 50 ^{o} and 70^o latitude. The cyclones travel around Antarctica in summer and winter. During winter, the cyclone frequency increases, and there is more activity in the Pacific.

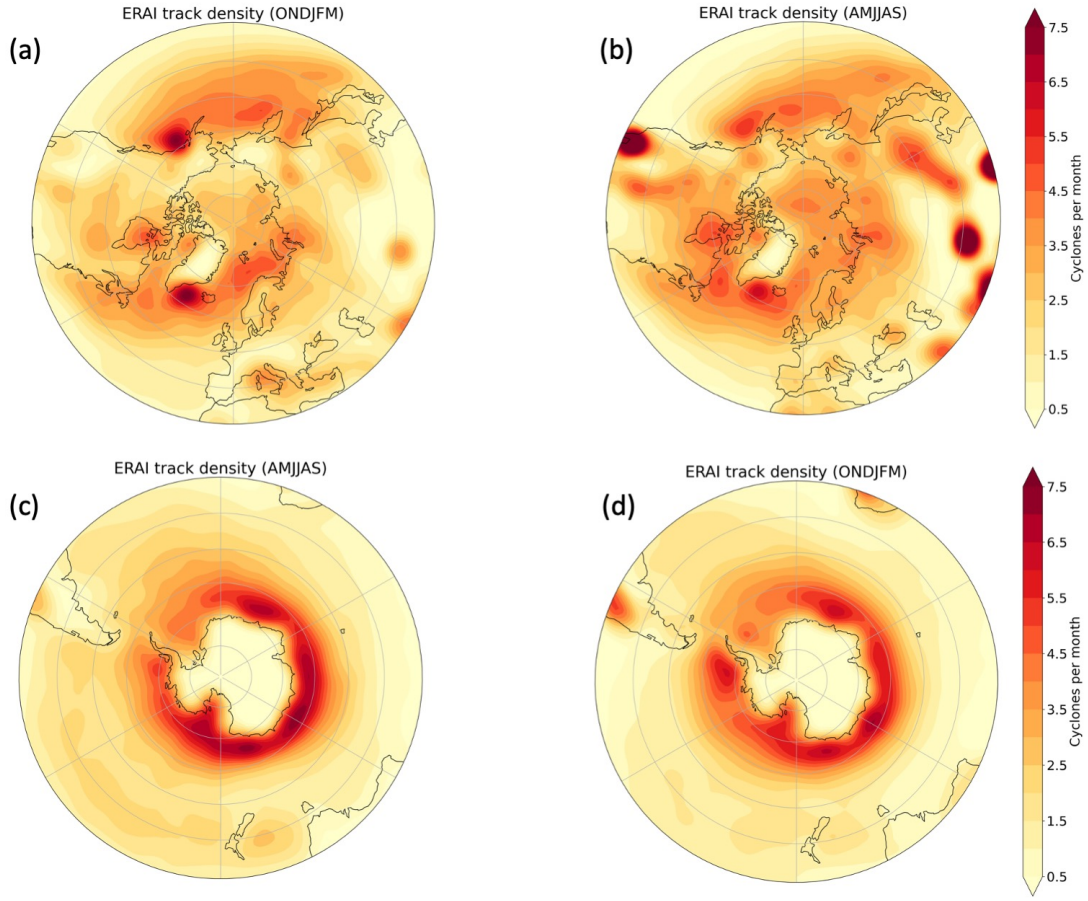

Figure 3.1: Cyclone track density in Era-Interim (1979-2010) in the Northern Hemisphere (a) winter and (b) summer and in the Southern Hemisphere (c) winter and (d) summer.

The CESM-LE model bias for the winter and summer months is shown in figure 3.2. The bounded domains in black, yellow and purple represent the North Atlantic, sub-North Atlantic and Mediterranean regions, respectively. In general, in the North Atlantic basin, the model tends to produce more cyclones over the US East Coast, between Iceland and Norway, around Greenland, Southern Spain and parts of Eastern Europe. However, there is a predominant underestimation of cyclone frequencies over the ocean. These results are again similar to previous studies based on the CESM-LE model (e.g. Day et al., 2018, Raible et al., 2018). Nevertheless, the CESM-LE storm track is not oriented too zonally over the North Atlantic, which is in contrast to many CMIP5 climate models (see Zappa et al., 2013).

To interpret this bias, it is essential to keep in mind that this analysis also includes weak cyclones, which may cause noisy results in some regions. This is particularly evident during the summer season. During summer, the overestimation increases in almost all the regions. The most remarkable difference is over southern Spain and the eastern Mediterranean, where the overestimation is even more than 3 cyclones per month. Probably, this overestimation is due to shallow cyclones with a short lifetime occurring in warm

conditions (Tous et al., 2016). This behaviour is clear in the life cycle of cyclones in the summer in the Northern Hemisphere (Fig. 3.3): the larger bias occurs for cyclones with a lifetime of fewer than 2 days, with the largest overestimation in the Mediterranean region (Fig. 3.3f) and the smallest overestimation in the sub-North Atlantic domain (excluding the Mediterranean region, Fig. 3.3d) for cyclones with a short lifetime.

In the Southern Hemisphere, the bias is smaller than in the Northern Hemisphere and has a less noisy spatial pattern. CESM-LE tends to produce more cyclones close to the polar region and below 60^o latitude equatorward the model produces fewer cyclones with the exception over land (e.g. southern America) (Fig. 3.1). The pattern is well-defined during the summer, where there is a clear belt of underestimation between 50^o and 60^o latitude.

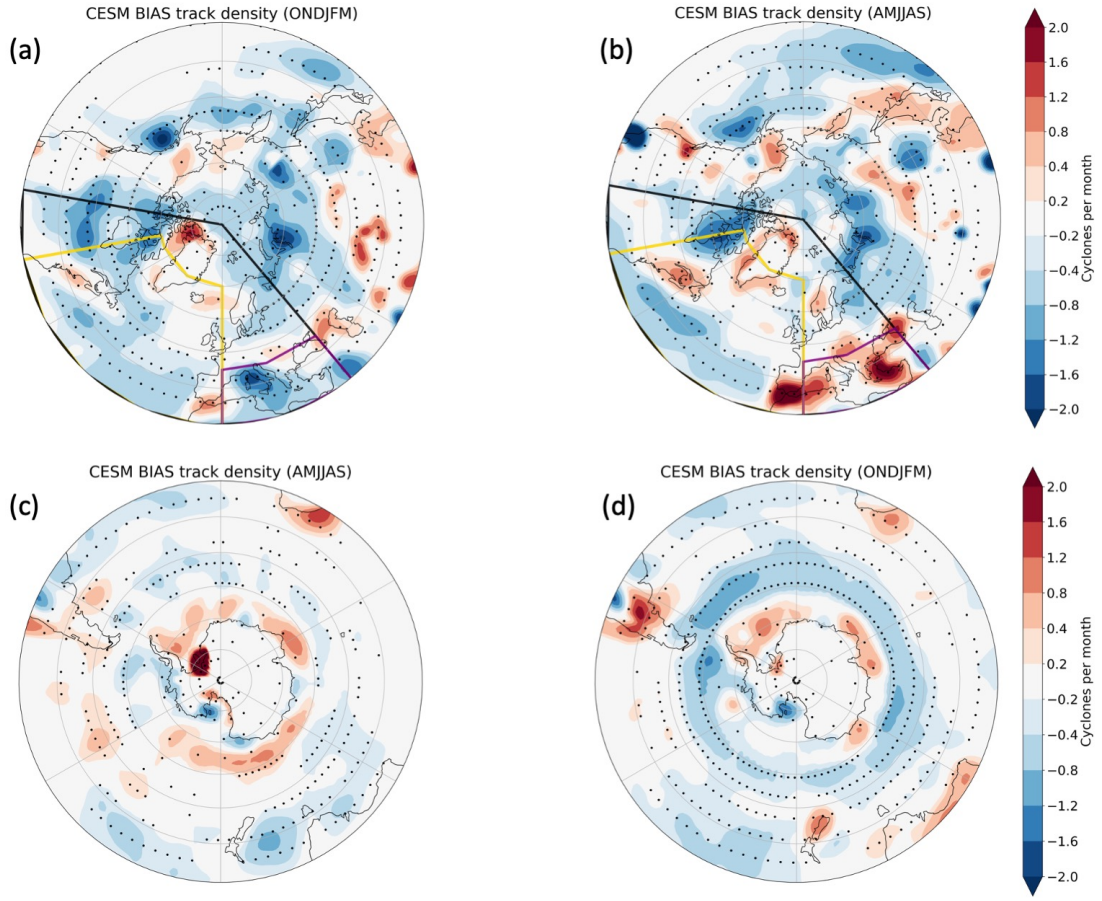

Figure 3.2: Mean track density bias of CESM-LE (1990-2000) relative to ERA-Interim (1979-2010) in the Northern Hemisphere (a) winter and (b) summer and in the Southern Hemisphere (c) winter and (d) summer. Black dots denote regions of ensemble agreement on the sign of bias, i.e. more than 80% of the ensemble members indicate a bias of the same sign. The boxes in (a) and (b) define the region of the North Atlantic (black box), sub-North Atlantic (yellow box) and the Mediterranean (purple box).

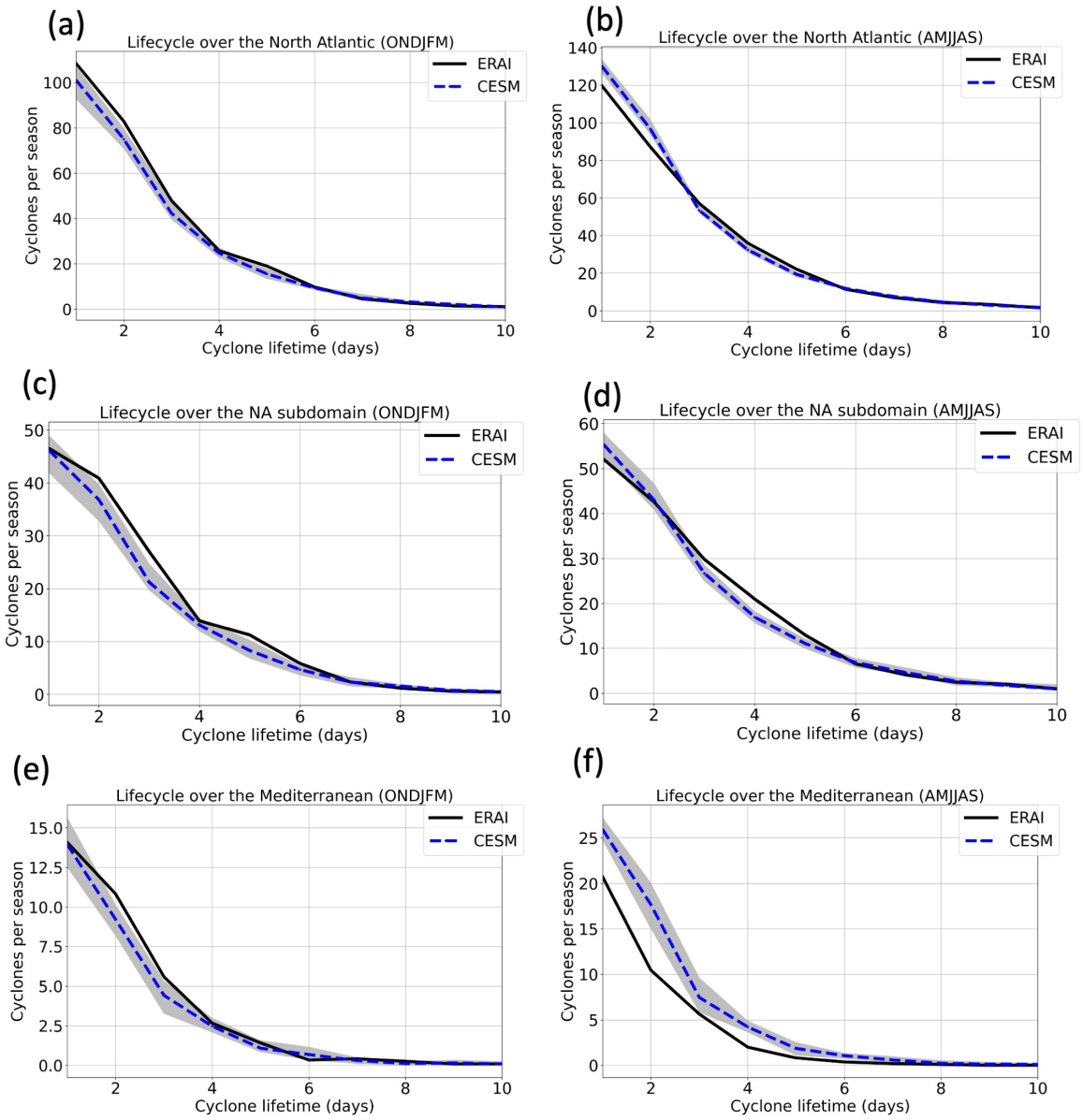

Figure 3.3: Statistical cyclone count as a function of lifetime in ERA-Interim (1979-2010) and CESM-LE (1990-2000). Ensemble mean and spread of ensemble members 1-10 (grey colour shading) for summer (a,c,e) and winter (b,d,f) in the North Atlantic (a,b, black box in Fig. 3.2), sub-North Atlantic (c,d, yellow box in Fig. 3.2) and Mediterranean region (e,f, purple box in Fig. 3.2).

3.3 Storm tracks response over the North Atlantic

In the same way as for the model evaluation in section 3.2, but now with a focus on the North Atlantic basin, we show the mean track density for present-day (1990-2000) extended winter (October-March) and summer (April-September) as well as its projected future change in cyclones per month (Figs. 3.4a,b and 3.4c,d). The cyclone activity response in a warmer climate at the end of the century [future (2091-2100) - present (1990-2000)] is particularly variable over the North Atlantic region (Fig. 3.4c,d). Despite this variability, there are some evident changes.

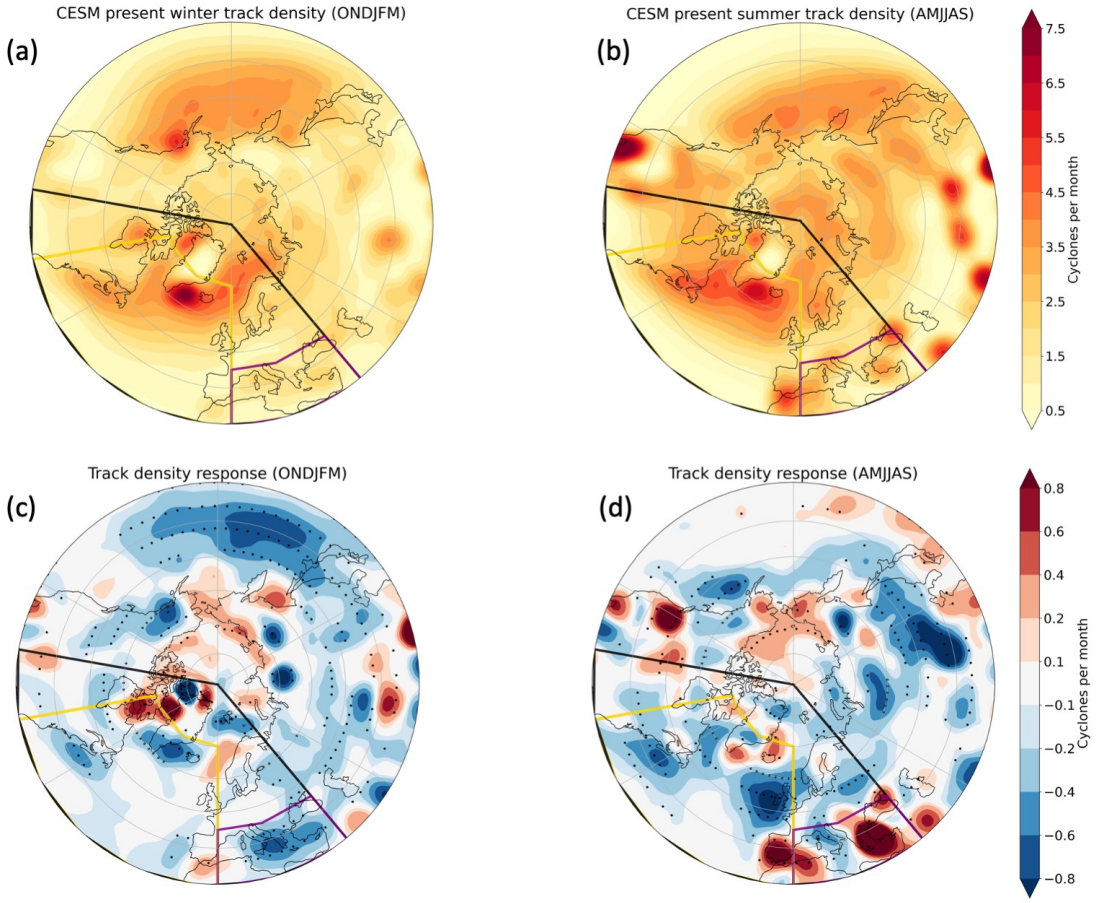

Figure 3.4: (a,b) Track density (1990-2000) and (c,d) mean track density response [Future (2091-2100) - Present (1990-2000)] for CESM-LE in (a,c) winter and (b,d) summer over the Northern Hemisphere. Black dots denote regions of an ensemble agreement on the sign of change, i.e. more than 80% of the ensemble members indicate a change of the same sign. The boxes define the region of the North Atlantic (black box), sub-North Atlantic (yellow box) and the Mediterranean (purple box).

In winter, the cyclone frequency decreases over the main storm track region, the US East Coast, southern Greenland, and the Mediterranean region. Figure 3.5a indicates that this decrease is mainly related to cyclones with a short life of 2 days or less. A similar

reduction in cyclone frequencies has been reported in other studies using the CESM-LE Model (e.g., Day et al., 2018, Raible et al., 2018) and other CMIP5 models (Zappa et al., 2013). Figure 3.4a also indicates more substantial cyclone frequency changes at higher latitudes around Greenland, in particular an increase in cyclone frequency to the west and north of Greenland. A slight increase is also found north of the United Kingdom and west of the Scandinavian peninsula. Zappa et al. (2013) show a more evident increase over the United Kingdom, based on their multi-model analysis, which is less evident in figure 3.4a. This difference may be due to a specific signature in CESM-LE simulations. Still, it might also be related to differences in the cyclone tracking scheme (note that Zappa et al. (2013) used the Hodges scheme for cyclone identification and tracking (Hodges, 1999)) and to the fact that we considered the months October-March while Zappa et al. (2013) analyzed December-February. The sensitivity of the climate change signal of the cyclones to the choice of the tracking method was analyzed in detail by Ulbrich et al. (2013), who found that the projected changes are more robust for strong than for weak cyclones.

In summer, the cyclone frequency decreases over the U.S. East Coast and the United Kingdom. Similar reductions at the southern flank of the storm track region have been mentioned in other studies (e.g., Zappa et al., 2013, Day et al., 2018, Priestley and Catto, 2022) and support a general poleward shift. Other regions that present less cyclone activity are Italy and Eastern Europe. On the other hand, the cyclone frequency shows a noticeable increase over the east coast of Greenland, and most pronouncedly over the Iberian Peninsula and the eastern Mediterranean, which has not been mentioned in previous studies. Note, however, that CESM has a substantial high bias in the cyclone frequency over the Mediterranean region in summer (see again Fig. 3.2b), such that these projected changes have to be interpreted with care.

In general, during winter, the frequency of cyclones decreases over the North Atlantic and the Mediterranean region. This signal is easier to see in the lifecycle figures (Fig. 3.5). In contrast, in summer, the cyclone frequency over the Mediterranean region increases (Fig. 3.5f). This increase is mostly caused by cyclones with a lifetime between 1 to 3 days, which probably are week cyclones forming under warm conditions (Alpert et al., 2004, Campins et al., 2011, Tous et al., 2016). Besides, the model tends to overestimate the frequency of cyclones with a short life in these areas (Figs. 3.2 and 3.3). In addition, we might expect more warmer-related low-pressure generation under a warmer environment in summer.

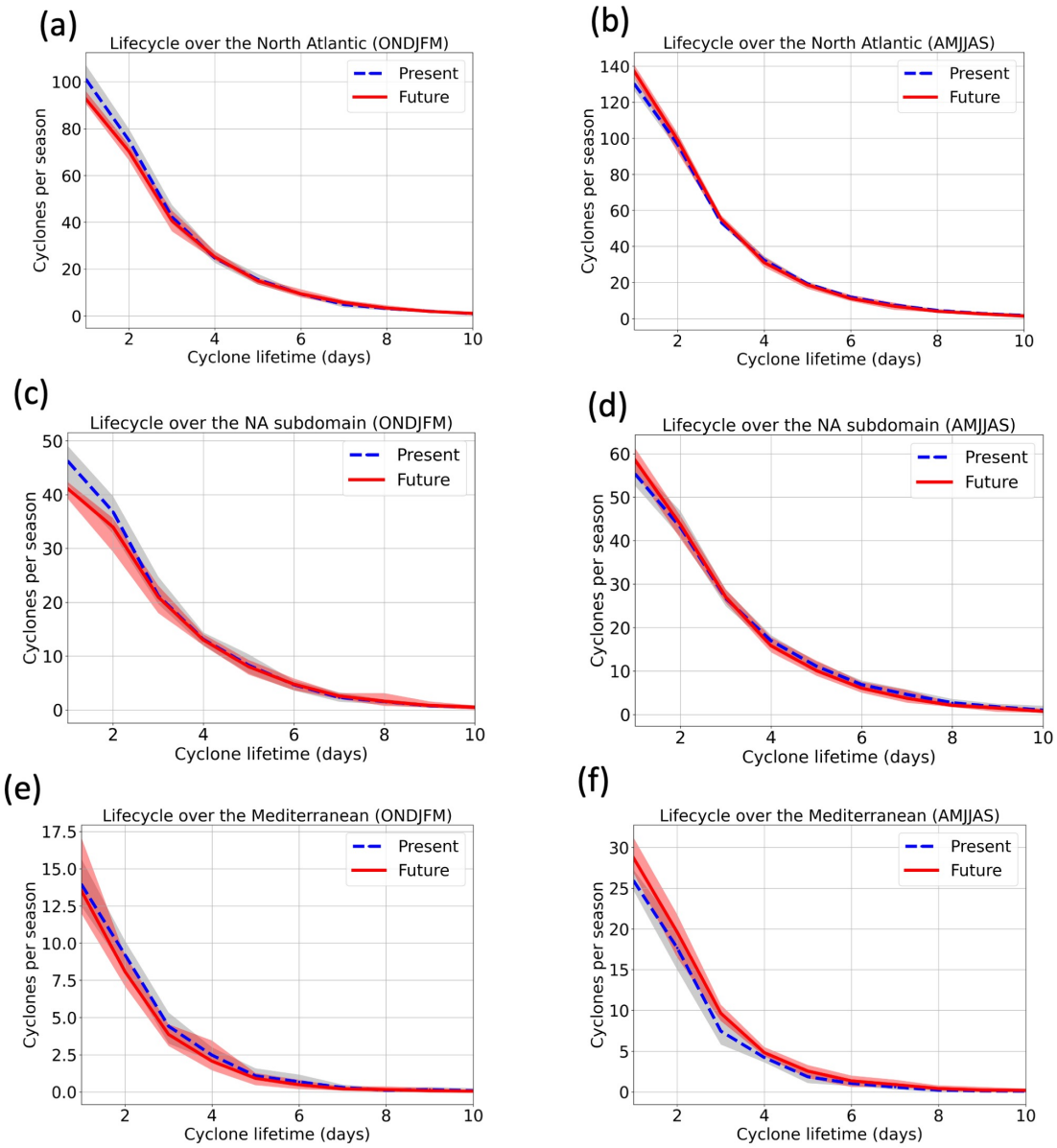

Figure 3.5: Statistical cyclone count as a function of lifetime in present (1990-2000) and future (2091-2100) simulations. Ensemble mean and spread of ensemble members 1-10 for summer (a,c,e) and winter (b,d,f) in the North Atlantic (a,b, black box in Fig. 3.4), sub-North Atlantic (c,d, yellow box in Fig. 3.4) and the Mediterranean region (e,f, purple box in Fig. 3.4).

3.4 Cyclone intensity response over the North Atlantic

As a measure of extratropical cyclone intensity, we use the relative vorticity at 850 hPa (RV850) averaged over a radius of 250 km around the location of the sea level pressure minimum for each time step during the cyclone lifetime (see Fig. 3.6). We select the North Atlantic basin, the black bounded domains in Figs. 3.1 and 3.2), to study the cyclone intensity response.

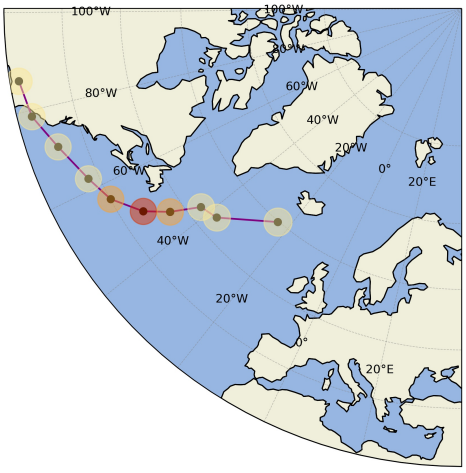

Figure 3.6: Example showing the averaging radius of 250 km along the cyclone track.

The spatial pattern of projected future changes in cyclone intensity is shown in figure 3.7a,b. In winter, extratropical cyclones are projected to become less intense over the main storm track and the Mediterranean region but more intense over the Norwegian Sea, northern Scandinavia and to the west and north of Greenland. Also, over Central Europe, there is an area of a slight increase in cyclone intensity. However, less than 8 of 10 ensemble members agree on the sign of this change.

In summer, cyclone intensity is projected to increase over parts of the northern part of the North Atlantic. The most pronounced cyclone intensity increase is located over the Baffin Bay and between Greenland and Iceland. A weakening of cyclones is projected over the more southerly part of the North Atlantic, with exceptions over the Iberian Peninsula and in the western Mediterranean region.

Fig. 3.7c,d shows the frequency distribution of cyclone intensity for the entire North Atlantic regions in present-day and future climate. The distributions are similar (no substantial change in cyclone intensity) and for most intensities, the frequency slightly decreases between present-day and future climate. In winter, there is only a subtle increase in the frequency of intense cyclones. The future-climate 90^{th} percentile of cyclone intensity is close to its present-day value, but the 99^{th} percentile slightly increases in the future. The presence of stronger winter cyclones in a warming climate has been suggested by Pinto et al. (2007) and Zappa et al. (2013); however, this result is less evident in our

analysis.

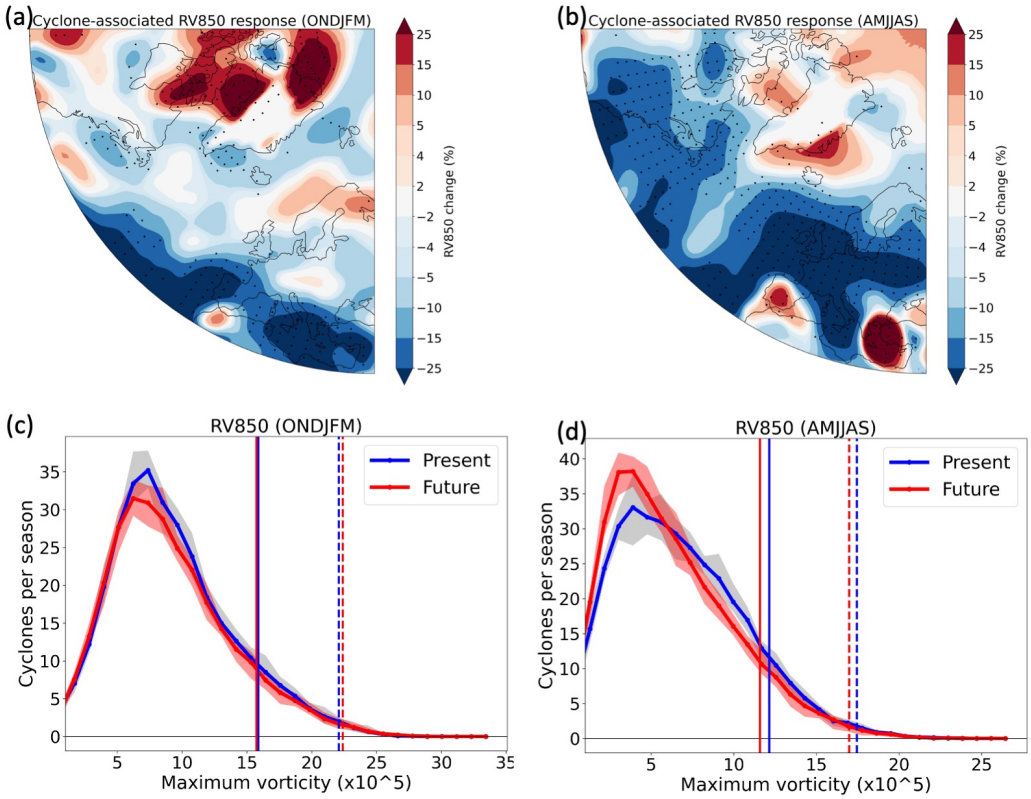

Figure 3.7: (a,b) Cyclones intensity (measured in terms of averaged RV850) response (Future (2091-2100) - Present (1990-2000)) in %. Black dots denote regions of ensemble agreement on the sign of change, i.e. more than 80% of the ensemble members indicate a change of the same sign. (c,d) Frequency distribution of cyclone intensity. Ensemble mean and spread of ensemble members 1-10 in (c) winter and (f) summer over the North Atlantic basin. The blue line represents present (1990-2000) and the red line represents future (2091-2100) climate. The vertical lines represent the 90^{th} (solid) and 99^{th} (dashed) percentiles.

In summer, the cyclone frequency change is more evident. The frequency of cyclones with low intensity increases while the frequency of strong cyclones decreases. Both 90^{th} and 99^{th} percentiles are lower in the simulated future compared to present-day climate, indicating a decrease of strong cyclones in summer, which is consistent with previous studies (e.g., Bengtsson et al., 2009, Zappa et al., 2013).

We also explore cyclone intensity changes in terms of wind speed. The maximum wind speed at 850 hPa is determined in a radius of 500 km around the location of the sea level pressure minimum for each time step during the cyclone lifetime. Fig. 3.8 shows future changes in the spatial pattern and frequency distribution of the cyclone-associated maximum wind speed in winter. The spatial patterns are similar to the changes in cyclone intensity measured in terms of relative vorticity (see again Fig. 3.7a) and generally

tend to follow the cyclone track response, with an increase in cyclone intensity and maximum winds in regions where the cyclone frequency is projected to increase. However, increases in maximum wind speed (e.g., over central Europe in winter) are typically more pronounced than the changes in cyclone intensity. Additionally, in winter, an increase in maximum wind speed of more than 10% is found north of the United Kingdom. In summer, the spatial pattern indicates less intense winds over the North Atlantic and Europe.

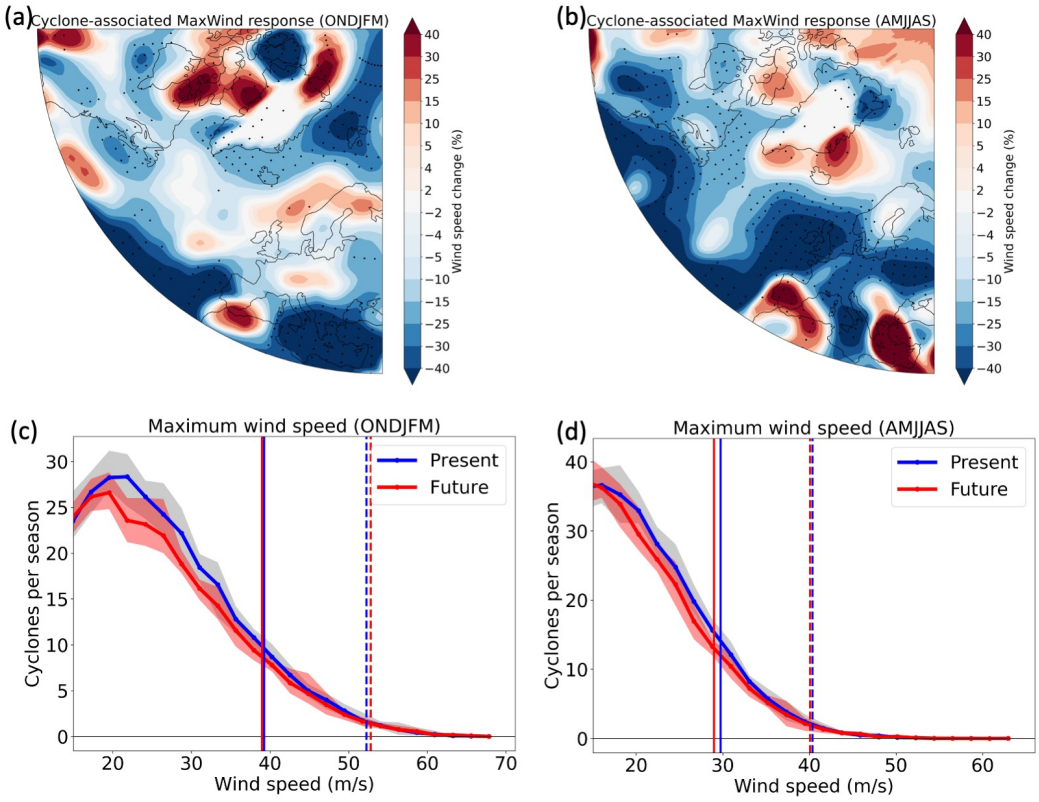

Figure 3.8: (a,b) Cyclones intensity (measured in terms of maximum wind speed at 850 hPa) response (Future (2091-2100) - Present (1990-2000)) in %. Black dots denote regions of ensemble agreement on the sign of change, i.e. more than 80% of the ensemble members indicate a change of the same sign. (c,d) Frequency distribution of cyclone intensity. Ensemble mean and spread of ensemble members 1-10 in (c) winter and (f) summer over the North Atlantic basin. The blue line represents present (1990-2000) and the red line represents future (2091-2100) climate. The vertical lines represent the 90^{th} (solid) and 99^{th} (dashed) percentiles.

Fig. 3.8c,d shows the frequency distribution of cyclone intensity in terms of the maximum wind speed at 850 hPa for the North Atlantic regions in present-day and future climate. Changes in frequency of strong cyclones are unclear. Nevertheless, there are some slight differences between the present and future climate in the percentiles. In winter, the 99^{th} percentile is projected to slightly increase in the future, whereas in summer, both the 90^{th} and 99^{th} percentiles are projected to decrease. Note, the 99^{th} percentile is higher in

winter (>50 m/s) than in summer (∼40m/s). This is consistent with previous studies, which have shown a higher incidence of strong windstorms in winter (e.g., Hewson and Neu, 2015).

3.5 Cyclone-associated precipitation response over the North Atlantic

To quantify the precipitation associated with cyclones, the simulated precipitation is averaged over a radial cap with a radius of 500 km around the cyclone center and traced along the cyclone track.

With 500 km, we selected a larger radius than for the relative vorticity field, because as Hawcroft et al. (2012) discussed, the precipitation farther way from the cyclone center (e.g., along the cold front) can be linked to the cyclone. Hawcroft et al. (2012) quantified that in winter (DJF) over the North Atlantic, the percentage contribution to the total precipitation climatology for $10/12/14^o$ radial caps is 54/71/81%. Note that the radius of 500 km compared to these values is still a relatively small and thus conservative estimate.

To quantify this fraction here, from the 6-hourly precipitation, the estimated cyclone-associated precipitation estimated is averaged over the entire analysis period to create cyclone-associated precipitation climatologies.

The relative cyclone-associated precipitation contribution to the total precipitation is shown in figure 3.9a,b. The figure shows that also in the CESM-LE simulations, a large part of the precipitation over the midlatitudes is associated with extratropical cyclones, with some seasonal variability. The maximum values are around 50%, as expected for using a radius smaller than Hawcroft et al. (2012). The most considerable contribution is located over the east coast of the USA and the Mediterranean region. The significance of cyclone-associated precipitation highlights the relevance of investigating future changes in the precipitation linked to extratropical cyclones.

Furthermore, the cyclone-associated precipitation response in a warming climate is examined in Fig. 3.9c,d. As expected, there are differences between the seasons. For instance, in winter, the cyclone-associated precipitation increases by up to 50 % over the North Atlantic; a clear increase is evident in central Europe. We can also see an increase over most of the territory of the USA. In contrast, the precipitation associated with extratropical cyclones tends to reduce over the Mediterranean region and parts of the Iberian Peninsula.

In summer, the precipitation increases only over the higher latitudes (mostly above 60^o) and for Europe and the U.S East coast, the cyclone-associated precipitation decreases.

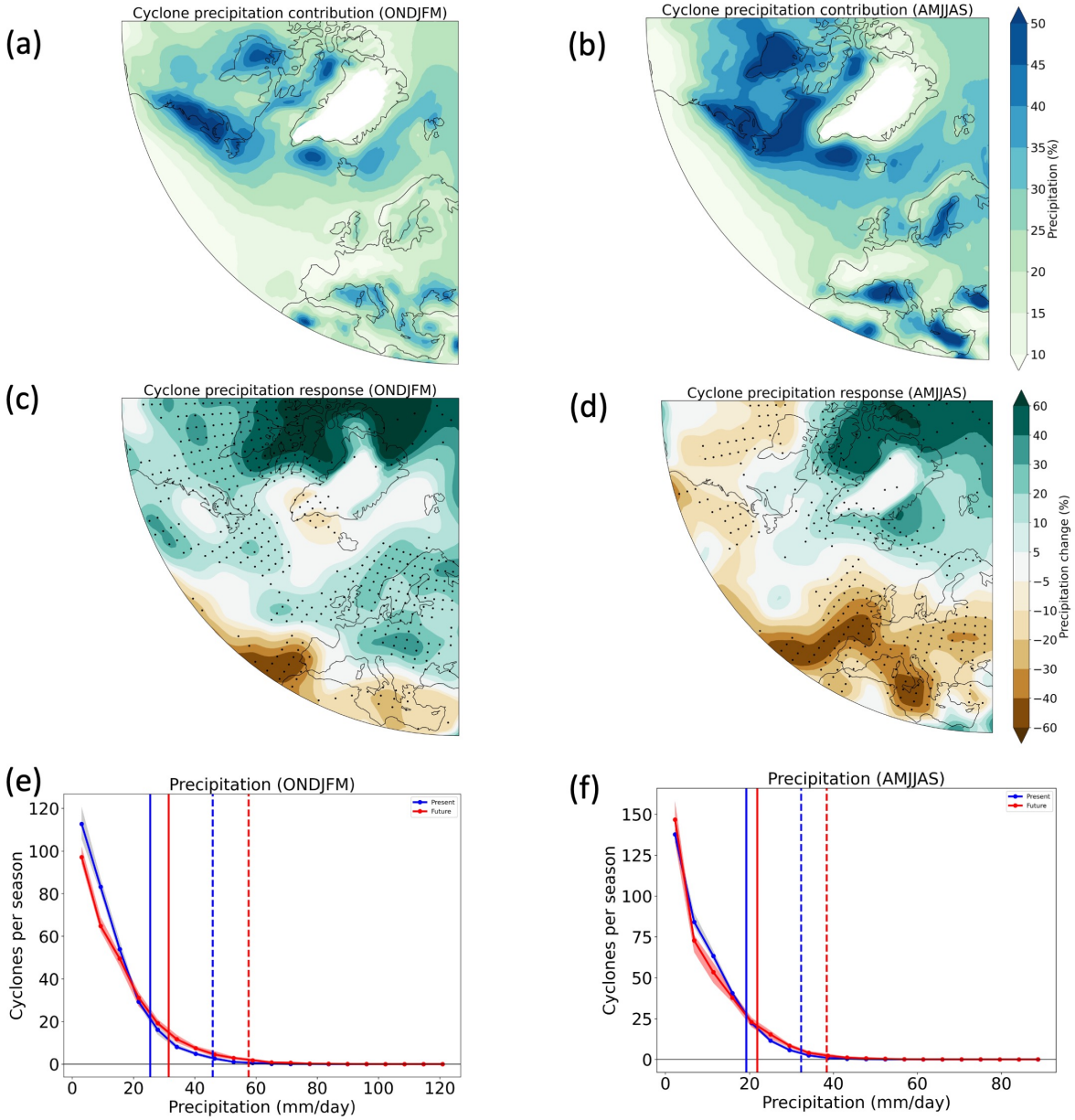

Figure 3.9: (a,b) Ensemble mean (members 1-10) of cyclones-associated precipitation contribution to the total precipitation in the North Atlantic region in present climate (1990-2000). (c,d) Cyclone-associated precipitation response (future (2091-2100) - present (1990-2000)). Black dots denote regions of ensemble disagreement on the sign of change, i.e. more than 80% of the ensemble members indicate a change of the same sign. (e,f) Frequency of occurrence of cyclones plotted for different bins of maximum cyclone precipitation intensity (the highest 6-hourly value along the cyclone track, mm/day). Ensemble mean and spread of ensemble members 1-10 in (a) winter and (b) summer over the North Atlantic basin. The blue line represents present-day (1990-2000) and the red line represents future (2091-2100) climate. The vertical lines represent the 90^{th} (solid) and 99^{th} (dashed) percentiles.

Note that, in general, the cyclone-associated precipitation response is similar to the total precipitation response (Fig. 2.3). A difference can be found in winter, where the cyclone-associated precipitation change is larger than the total precipitation change in central Europe. Also, the results are consistent with previous studies (e.g., Yettella and Kay, 2017).

In addition, we examine the maximum value of the area-averaged precipitation during the lifecycle of each cyclone over the North Atlantic to analyze the change of the more intense cyclone precipitation, which is related to precipitation extremes (Pfahl and Wernli, 2012). As for relative vorticity, we show the frequency distribution of maximum cyclone precipitation (Fig. 3.9f).

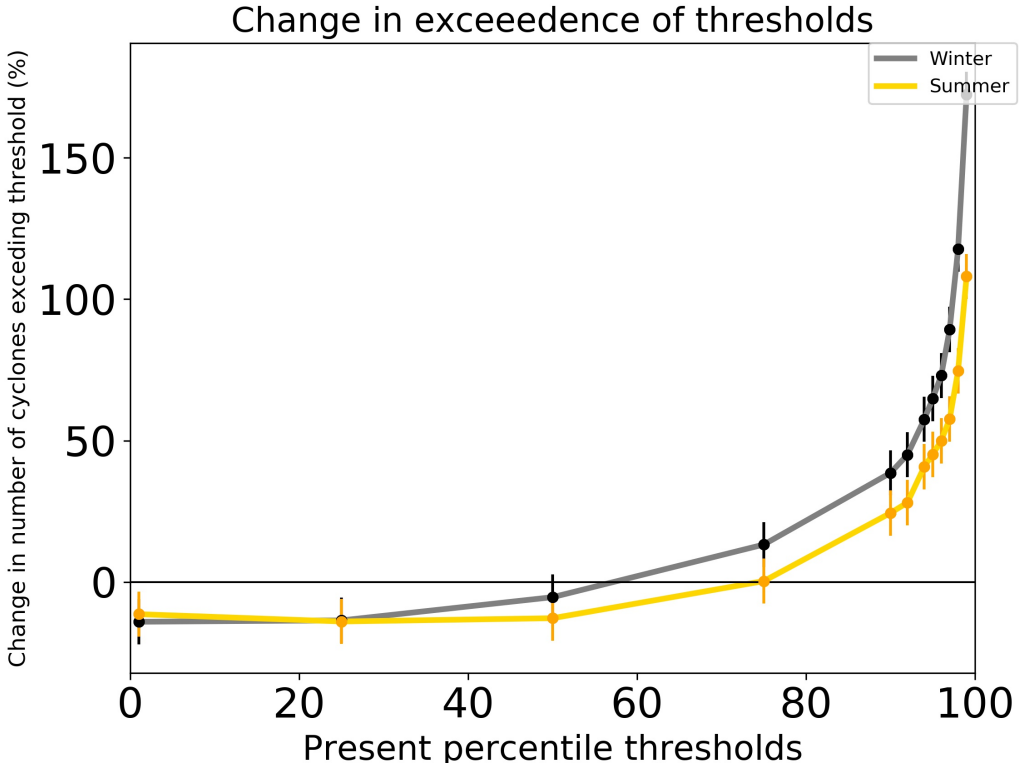

Figure 3.10: Change in the number of cyclones exceeding present precipitation thresholds (e.g., absolute precipitation intensity associated with the 90^{th} percentile defined for the period 1990-2000) in the North Atlantic for winter (grey) and summer (yellow). Vertical lines show the ensemble spread (maximum and minimum values of ensemble members 1-10).

In this case, we see a clear increase in the number of cyclones with intense precipitation in all seasons but with a stronger signal in winter. These increases are consistent with the 90^{th} and 99^{th} percentile values, which are larger in the future. The decrease in the number of cyclones with lower precipitation and the increasing number of cyclones with more intense precipitation is also shown in Fig. 3.10, where the most extreme (above the present 99^{th}) cyclones increase in number by around 150% in winter and 100% in summer.

3.6 Discussion

In summary, this section shows that the cyclone frequency biases in CESM-LE are relatively small in the main storm track region and are mainly due to short-lived cyclones. In comaparison with ERA-Interim, the model shows a higher bias during summer, specifically over the Iberian Peninsula and Mediterranean region. The lifecycle analysis shows that the model has less ability to reproduce cyclones with a short lifetime (> 2 days), which might be associated with an overestimation of warm conditions (positive temperature bias) in the model, particularly in the western Mediterranean (Fig. 3.11).

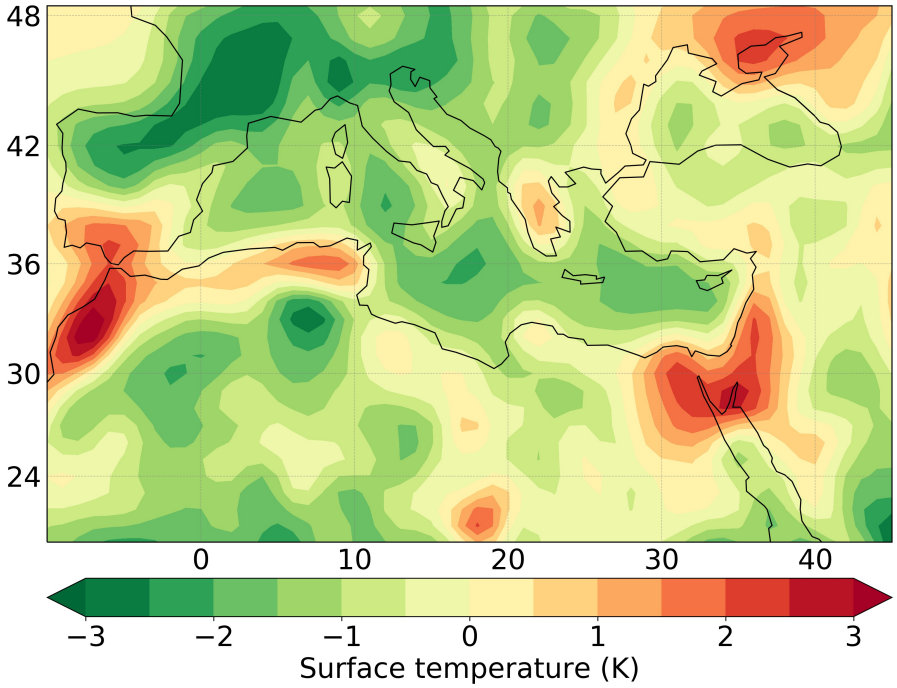

Figure 3.11: Surface temperature bias of CESM-LE (1990-2000) relative to ERA-Interim (1979-2010). During the the summer in the Mediterranean. CESM-LE ensemble members 1 to 10.

Future projections of cyclone frequencies mostly indicate a decrease over the ocean and the Mediterranean region, consistent with previous studies. However, during the summer over the Mediterranean region, an increase of cyclones with a short lifetime is projected.

Additionally, cyclone intensities are not projected to change substantially overall, and the spatial variations in intensity changes are similar to frequency changes. This lack of major cyclone intensity changes is consistent with previous studies (Ulbrich et al., 2009, Zappa et al., 2013, Pfahl et al., 2015, Day et al., 2018, Raible et al., 2018, Catto et al., 2019)

and most likely due to the competition between different thermodynamic and dynamic factors, as outlined in section 1.1. Nevertheless, as suggested by Catto et al. (2019), such projected changes in cyclone intensity may depend on the metric used for its definition. Here, we use the relative vorticity in a radius of 250 km, but other radii or even other measures, such as deepening rates (e.g., Binder et al., 2016), might lead to different results. With regard to precipitation, the frequency of cyclones with high precipitation rates is projected to increase. The same is true for precipitation extremes, which may increase by up to 150% in winter.

The analysis presented here has some limitations. It is based on a single climate model and thus does not take model uncertainty into account. On the other hand, by using several ensemble members, we have assessed the robustness of our findings with respect to natural climate variability (similar to, e.g., Yettella and Kay, 2017). Furthermore, our study uses a single cyclone tracking algorithm, which has been applied successfully before in many other studies on midlatitude cyclones (e.g., Pfahl et al., 2015, Sprenger et al., 2017) and gives results that are in the range of other tracking schemes (Neu et al., 2013). Arguments for the robustness of our findings concerning this choice of the tracking scheme are, again, that similar results have been obtained with other tracking algorithms, also using the same climate model (Day et al., 2018), and that the dependence on the tracking scheme is generally weaker for intense (compared to weak) cyclones (Neu et al., 2013, Ulbrich et al., 2013).

4 A composite perspective on changes of extratropical cyclones in a warming climate

In the previous section, we found a remarkable increase in precipitation rates and only minor projected changes in cyclone intensity in CESM-LE. However, even if overall intensity changes are small, there may be changes in cyclone dynamics and structure that can affect, e.g., spatial patterns of near-surface winds. Hence, we focus on cyclone structure and dynamic properties in more detail in the following. The leading hypothesis is that changes in cyclone impacts, such as wind gusts, do not occur only because of the shift in storm tracks but also because the properties of individual cyclones may change in a warming climate. Therefore, this section aims to investigate storm-scale dynamical changes with the help of composite analysis.

4.1 Data and methods

Obtaining composites

Cyclone-centered composites are created for the 10% strongest storms (denoted as intense cyclones in the following) occurring over the North Atlantic region (see Fig. 2.4), selected by their maximum relative vorticity at 850 hPa averaged over a radius of 250 km around the cyclone center (SLP minimum). Various fields are composited for the time of maximum intensity in accordance with the 850 hPa relative vorticity (t=0), as well as previous hours (t=-24, -18, -12, -6 h) and later hours (t=+6, +12, +18, +24 h) (see Fig. 4.1b). A radial grid with the pole centered on the cyclone center is generated, covering a spherical cap with a fixed radius of 10^o. Meteorological fields are then extracted to this new radial coordinate system and averaged over the chosen extratropical cyclones (Fig. 4.1a). The coordinate transformation reduces the distortion due to change in zonal grid spacing with latitude, as described in previous studies (Bengtsson et al., 2009, Catto et al., 2010). In some previous studies, this spherical cap has been rotated in the direction of cyclone propagation. We have tested such a rotation and decided not to use it because it introduced some noise in the composites (e.g., frontal structures appeared to be less apparent in the rotated compared to the unrotated composites, see Fig. A.1).

A complementary perspective on cyclone dynamics is obtained by constructing PV anomalies and PV anomaly profiles. To this end, a PV climatology is defined as follows: Firstly, the daily mean PV for each calendar day is calculated at each grid point and each vertical level of the model, separately for present-day (1990-2000) and future (2091-2100) climate. Then, a 30-day window is selected relative to each cyclone position, and composites (as

described previously) are obtained, averaged over these 30 days, on different interpolated pressure levels (1000, 925, 850, 750, 700, 600, 500, 400, 300, 250, 200, 150 hPa) from the calendar-day mean PV dataset. PV anomalies are then defined relative to these 30-day average. Finally, PV anomalies are spatially averaged in a radius of 2.5° around to the cyclone center to construct the PV anomaly profiles.

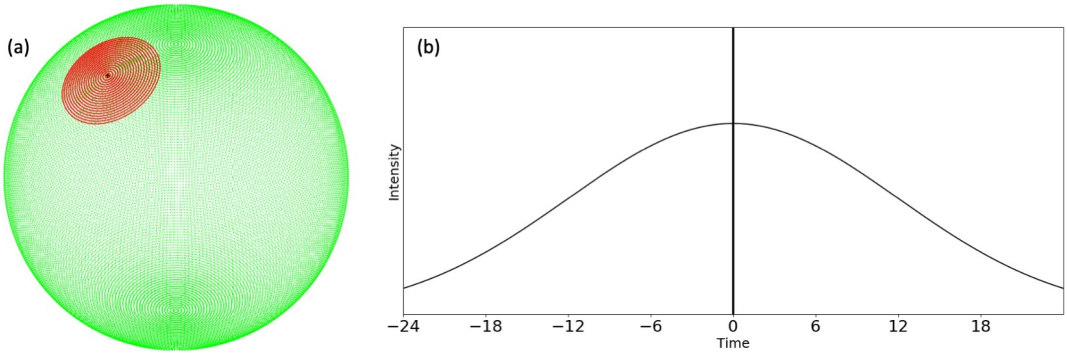

Figure 4.1: (a) Illustration of a cyclone-centric radial grid. The green points represent model grid points. The black dot is a sample cyclone center. The red points represent the radial grid (from Yettella and Kay, 2017). (b) Time steps extracted to build the composites.

4.2 Composites of intense cyclones

We use the 10% strongest storms over the North Atlantic in each ensemble member for the composite analysis. In this way, the focus is laid on the main storm track region over the ocean (as shown in Fig. 4.2), where the model also has the smallest biases compared to other regions such as the Mediterranean. In addition, the 10% strongest cyclones are typically associated with strong winds and high precipitation rates.

Figure 4.2 shows the future change in intense cyclone frequency. A bipolar pattern dominates the response in track density. In winter, an increase in intense cyclone frequency is projected over the northeast Atlantic region (Fig. 4.2c). The increase spreads over the northern United Kingdom and the western coast of Norway. In contrast, there is a reduction in track density to the south and east of Greenland. Contrary to winter, the largest increase in summer is located over the Greenland Sea (Fig. 4.2d). A reduction in cyclone frequency extends from the US east coast to the United Kingdom, with the most significant decrease to the west of the United Kingdom.

These results are again similar to the strong cyclone response found by Zappa et al. (2013), who defined strong cyclones as those exceeding a threshold in the maximum along-track wind speed at 850 hPa. However, Fig. 4.2b indicates a more evident increase in cyclone frequency than the results shown by Zappa et al. (2013) in the eastern North Atlantic in winter. Figure 4.2b also confirms that the notable changes in the frequency of all cyclones in figure 3.4a over west Greenland and high latitudes are due to relative weak storms.

Furthermore, the mean response found in the CESM model is also consistent with previous studies using other models (Leckebusch and Ulbrich, 2004, Pinto et al., 2009). For example, Pinto et al. (2009) analyzed the 10% strongest storms in the North Atlantic during the extended winter (October-March) with the ECHAM5 model and found an increase in cyclone frequency over the British Isles and the North Sea, but with the maximum increase slightly shifted southward in comparison to our results.

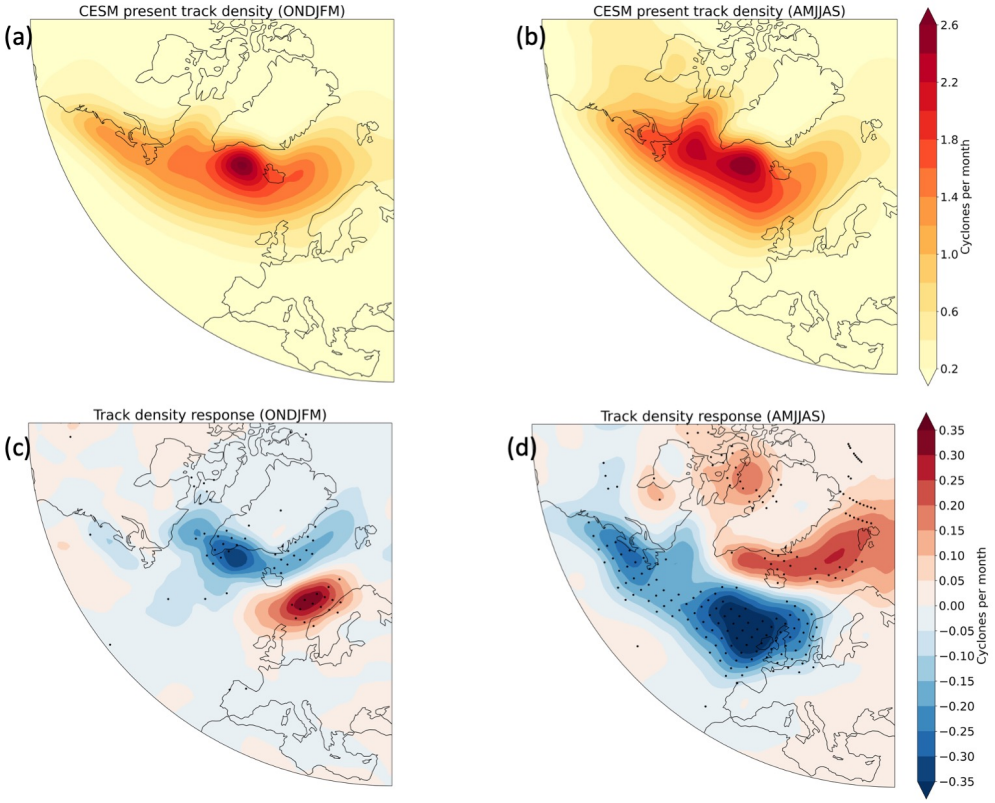

Figure 4.2: (a,b) Track density (1990-2000) and (c,d) mean track density response [future (2091-2100) - present (1990-2000)] for CESM-LE in (a,c) winter and (b,d) summer over the North Atlantic region, taking into account the 10% strongest extratropical cyclones.

The temporal evolution of the relative vorticity at 850 hPa (RV850) from the composites for the intense cyclones over the North Atlantic is shown in Fig. 4.3 (temporal evolution for all cyclones in ensemble number 1 are shown in Fig. B.1). Firstly, by construction, we find the maximum RV850 at time 0 (which is defined as the time of the maximum intensity). Also, the cyclones are more intense in winter than in summer. In the simulated warmer future climate, there is no clear increase in intensity at any time of the cyclone evolution. On the contrary, in summer, the cyclone intensity slightly decreases.

Regarding precipitation, we observe that the more intense rainfall occurs before the maximum intensity (time = -12 in winter and time = -6 in summer), and similar to RV850, the more intense precipitation occurs in the winter. Contrary to the cyclone intensity, there is a robust increase in future cyclone precipitation at the time steps considered. The maximum precipitation increase occurs before the time of maximum intensity.

These results are consistent with the previous section, where we showed that in the warmer future climate, the cyclones are associated with more precipitation, but the intensity trend is not clear. Temporal evolution for all cyclones in ensemble 1 is found in Fig. B.1.

The following composite analysis also includes other variables related to cyclone circulation, such as vertical velocity at 850 hPa (omega, Pa/s) and horizontal wind speed at 850 hPa (m/s). The latter is particularly relevant for the societal impacts of cyclones.

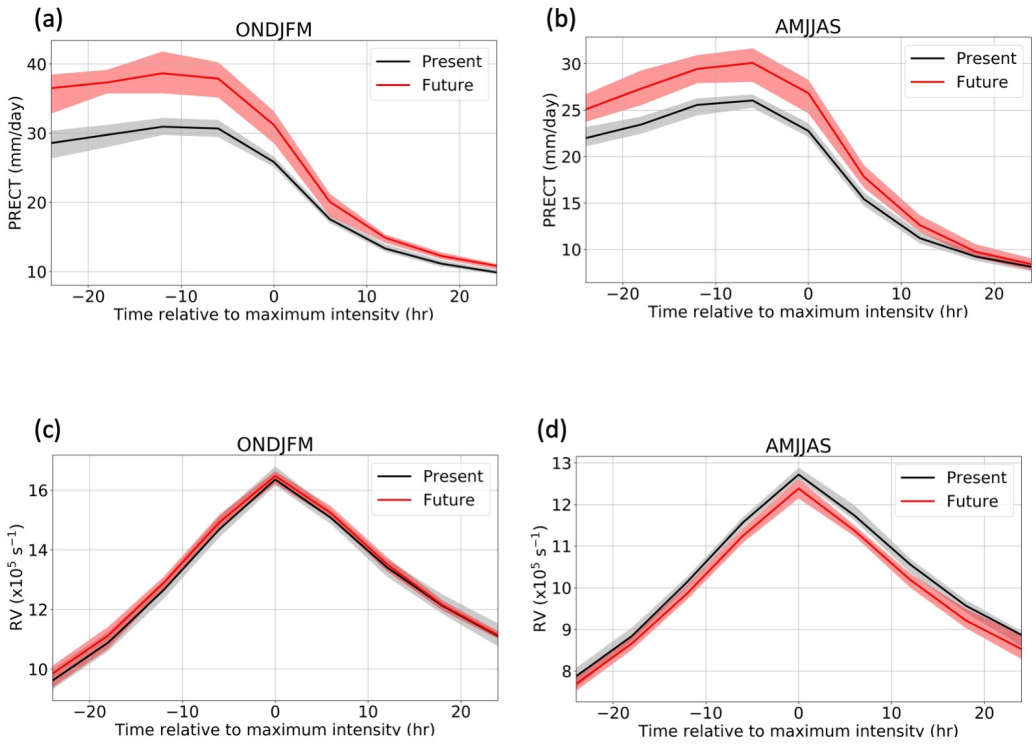

Figure 4.3: (a,b) Precipitation and (c, d) relative vorticity composite cyclone lifecycles for (a, c) winter and (b,d) summer in the North Atlantic. The black line represents present-day (1990-2000) and the red line represents future (2091-2100) climate. Precipitation is averaged within 5^o of the cyclone center and relative vorticity within 2.5^o of the cyclone center.

Present-day structure and properties of intense cyclones

The structure of the intense storms in present-day is examined in this section (difference between intense and all cyclones in ensemble number 1 are shown in Fig. B.2).

Figure 4.4 shows the composite precipitation, vertical velocity at 850 hPa and temperature at 850 hPa. We can identify the comma shape in the precipitation composite, which is typical for midlatitude cyclones and its (WCB) activity (e.g. Yettella and Kay, 2017,

Catto et al., 2010). The maximum precipitation is above 36 mm/day, and it is close to the cyclone center but with a slight northward displacement. This precipitation over the cyclone center is often called the occlusion band in a mature extratropical cyclone (Houze Jr, 2014).

Moreover, in Figs 4.4c and 4.4d the corresponding ascent is shown. The vertical motion is generally upward in the eastern half of the composite and downward in the western half. The ascent downstream over the warm sector indicates the WCB activity. The ascent also wraps cyclonically around the northward and upstream sides of the cyclone center.

Temperature composites at 850 hPa (Figs. 4.4e and 4.4f) show two zones of stronger gradient, the first is a bent-back gradient located to the south of the cyclone center, and the second is located to the east of the cyclone center.

Therefore, the precipitation and the temperature at 850 hPa composites show that the warm front is located east of the cyclone center (region of enhanced precipitation and strong temperature gradient) and the cold front is located to the south of the center (region of strong temperature gradient). Note that the fronts of individual cyclones will not be totally aligned, such that the temperature gradient is smoothed in the composite.

The average precipitation amount and cyclone intensity are more extensive in winter (Fig. 4.4a). Pressure and temperature gradients are also stronger in winter than in summer (Fig. 4.4e). Apart from the intensity, we can notice some seasonal differences in spatial patterns. For example, precipitation is more confined to the cyclone center during summer. Moreover, contrary to winter, the strongest temperature gradient during summer has a south-eastward displacement, suggesting a faster occlusion of the fronts.

Figure 4.5 shows the composites of relative vorticity at 850 hPa (RV850) and sea level pressure (SLP) (Fig. 4.5a,b), wind speed at lower levels (850 hPa, Fig. 4.5c,d) and wind speed at upper levels (250 hPa, 4.5e,f) for intense cyclones in present-day climate (1990-2000) at the time of their maximum intensity. The largest RV850 (Fig. 4.5a,b) is found in a region of approximately $\pm$ 2.5^o around the cyclone center. The horizontal gradient of RV850 is larger upstream than downstream of the cyclone center. Therefore, high values of RV850 (values above 4x10$^{-5}s^{-1}$) cover a more extensive area to the east of the SLP minimum, in the region of the warm front.

The wind speed at 850 hPa (Fig. 4.5c,d) shows a well-defined cyclonic circulation with equatorward flow upstream and poleward flow downstream of the cyclone center. The regional maximum wind speed at 850 hPa is located to the southeast of the cyclone center, over the warm sector, where the highest values are above 26 m/s. Similar low-level wind patterns with the strongest winds in a region from southwest to east of the cyclone center have been found in previous studies (Slater et al., 2015, 2017). The wind speed maximum in figure 4.5c,d may be related to the low-level jet (LLJ) that typically occurs ahead of the cold front. This low-level jet and the associated wind shear can result in strong wind gusts at the surface (Lackmann, 2002). Note, however, that the compositing method may

average out some of the air-stream related features. For instance, some storms may have the wind maximum behind the cold front associated with the CCB, others in the low-level jet region ahead of the front, and averaging then produces a broader maximum covering the entire area.

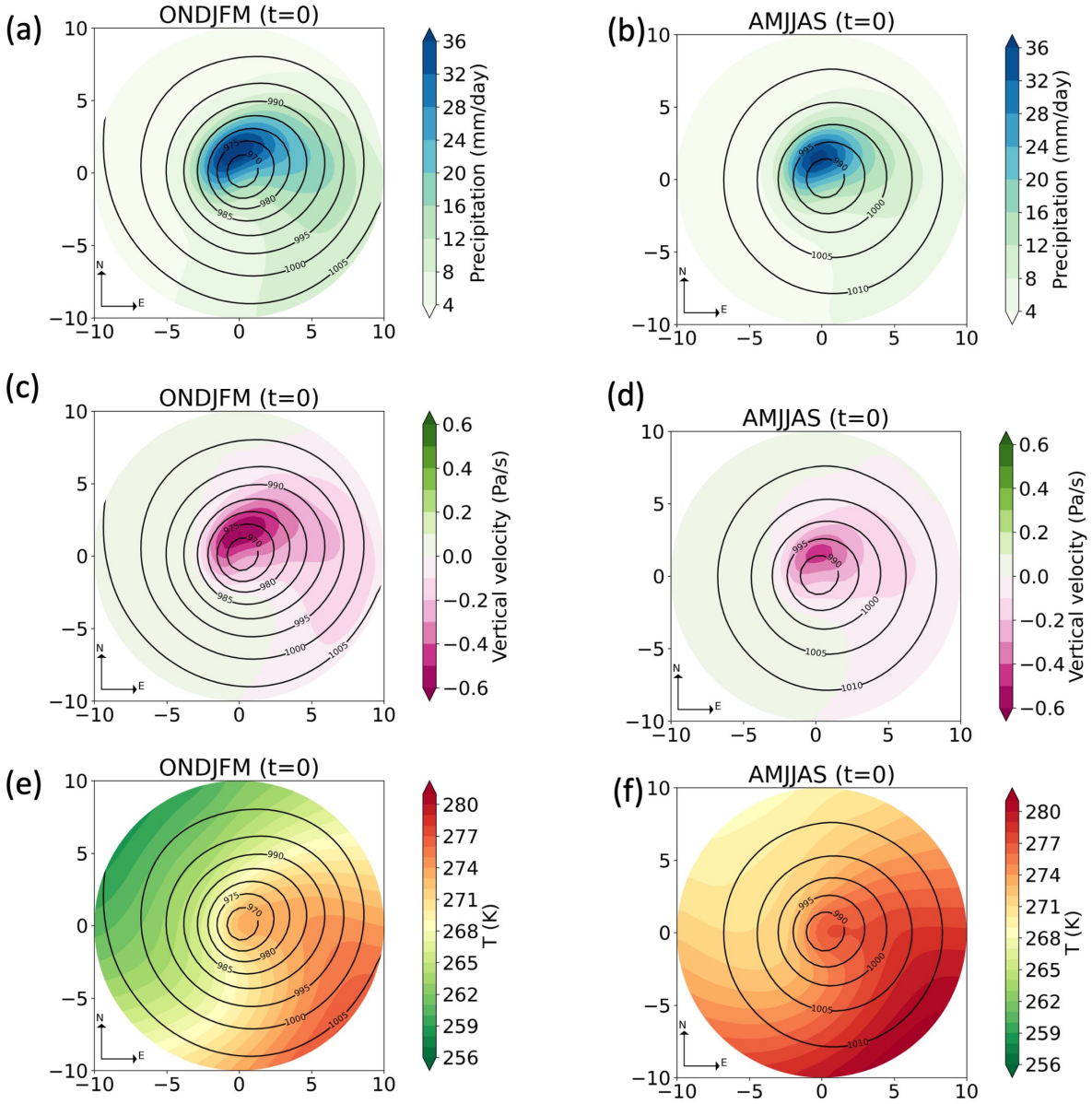

Figure 4.4: Present (1990-2000) cyclone (a,b) precipitation, (c,d) vertical velocity at 850 hPa and (e,f) temperature at 850 hPa composites for (a,c,e) winter and (b,d,f) summer in the North Atlantic. Mean SLP (hPa) is overlaid as black contour lines. The composites are shown at the time of maximum intensity (time=0).

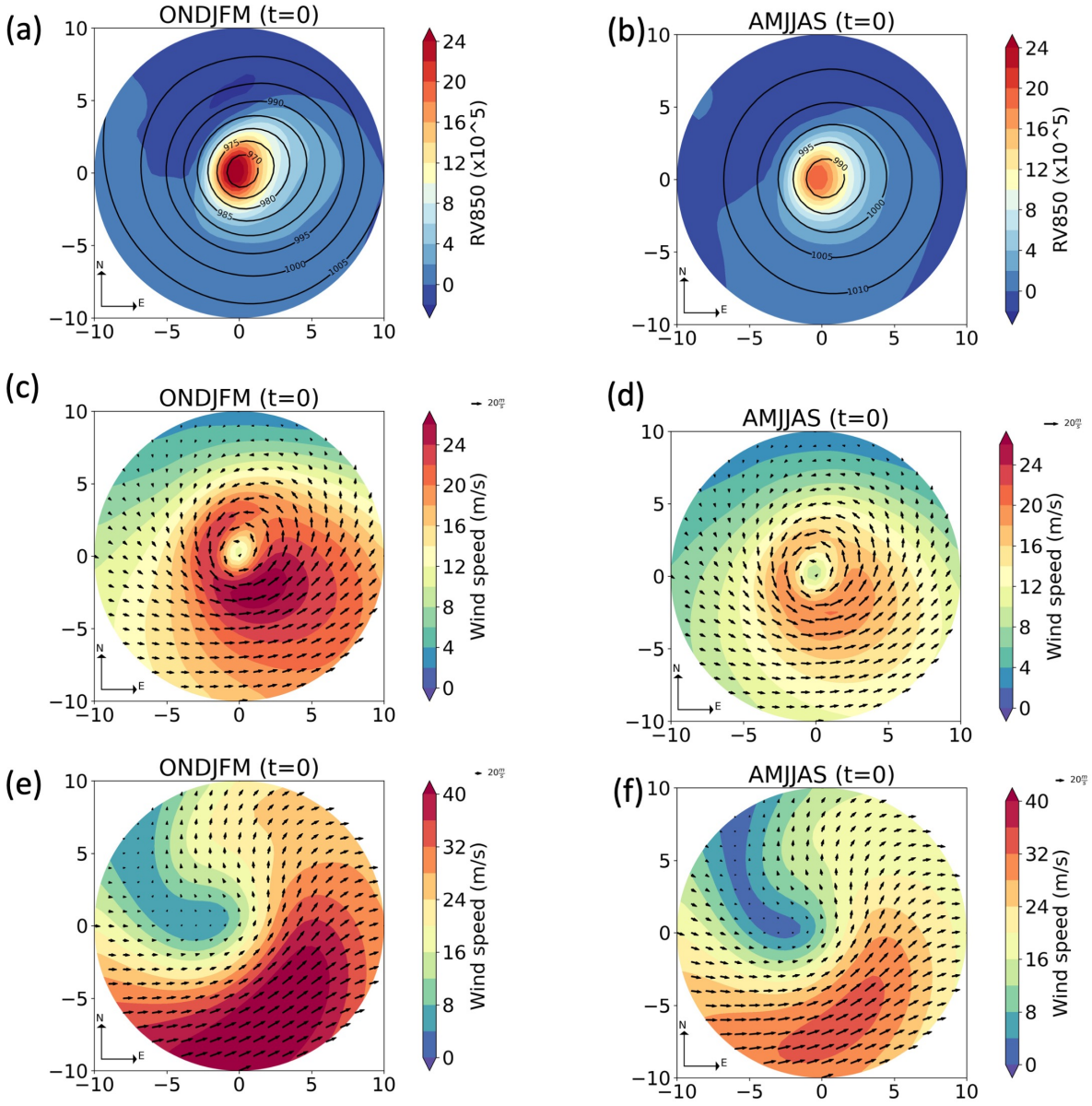

Figure 4.5: Present (1990-2000) cyclone (a,b) RV850, (c,d) wind at 850 hPa and (e,f) wind at 250 hPa composites for (a,c,e) winter and (b,d,f) summer in the North Atlantic region. Mean SLP (hPa) is overlaid as black contour lines in (a,b). The composites are shown at the time of maximum intensity (time=0).

The upper-level wind composite (Fig. 4.5e,f) shows the jet stream and its local maximum (jet streak) to the south of the cyclone center. The jet's wind direction is eastward to the south and poleward to the east of the cyclone center. The poleward flow to the east enhances the poleward motion of the low-level cyclone. Assuming that this poleward flow has also persisted in the period before maximum cyclone intensity, it may have contributed to cyclone intensification when the system crossed the upper-level jet axis (Rivière et al., 2013, Tamarin and Kaspi, 2017). At their time of maximum intensity, the most intense

cyclones are typically located near the left exit region of the upper-level jet streak, as also evident from figure 4.5e, in an area of strong quasi-geostrophic forcing (Barnes and Colman, 1993, Deveson et al., 2002).

The patterns in winter and summer are generally similar. We observe lower magnitudes and less well-defined cyclone structure during the summer season (Fig. 4.5b,d,f). The wind field gradients at lower levels appear to be more north-south oriented in summer; meanwhile, during winter, they tilt from northwest to southeast.

Future changes in structure and properties of intense cyclones

The response of intense extratropical cyclone composites is investigated in this section (future responses for all cyclones in ensemble number 1 are shown in Fig. B.3). The precipitation composites are shown in Figs. 4.6a and 4.6b. The precipitation increase is evident downstream of the cyclone center (region of the warm conveyor belt ascent), with strong changes located close to and north of the cyclone center. The results are similar to Yettella and Kay (2017).

We also show the precipitation change in percentage in Figs. 4.6c and 4.6d. From these figures, we find two bands of precipitation increase, the first reaching southward from the cyclone center and the second reaching eastwards, which are probably related to precipitation at the warm and cold front, respectively. The most significant increase is over the likely location of the warm front.

The maximum precipitation increase in percentage is between 30-35 %. Based on the global surface temperature increase in the CESM model (around 5 ^{o}K), this maximum rate of moisture increase is around 6-7% K^{-1} which is close to the Clausius-Clapeyron relation (6-7 % K^{-1}) (Schneider et al., 2010). There is an exception for winter; in the far-eastern part of the warm front, the increase appears to be larger than the Clausius-Clapeyron rate. This precipitation zone above the Clausius-Clapeyron rate is even more pronounced in terms of spatial extent and intensity during the hours before the maximum intensity (not shown). It covers the whole warm front region and increases above 40%. The latter results suggest that, in addition to a thermodynamic precipitation increase, amplified dynamical processes might contribute to the precipitation intensification in a warming climate (see, e.g., Pfahl et al., 2017). This will be further investigated in chapter 7.

Contrary to the results of Yettella and Kay (2017), the increase in winter is more extensive than in summer. In summer, the pattern is comparable with winter, with three zones of precipitation increase: the center, warm and cold front. The precipitation associated with the fronts spreads out, the cold front is displaced westward, and the warm front is displaced poleward.

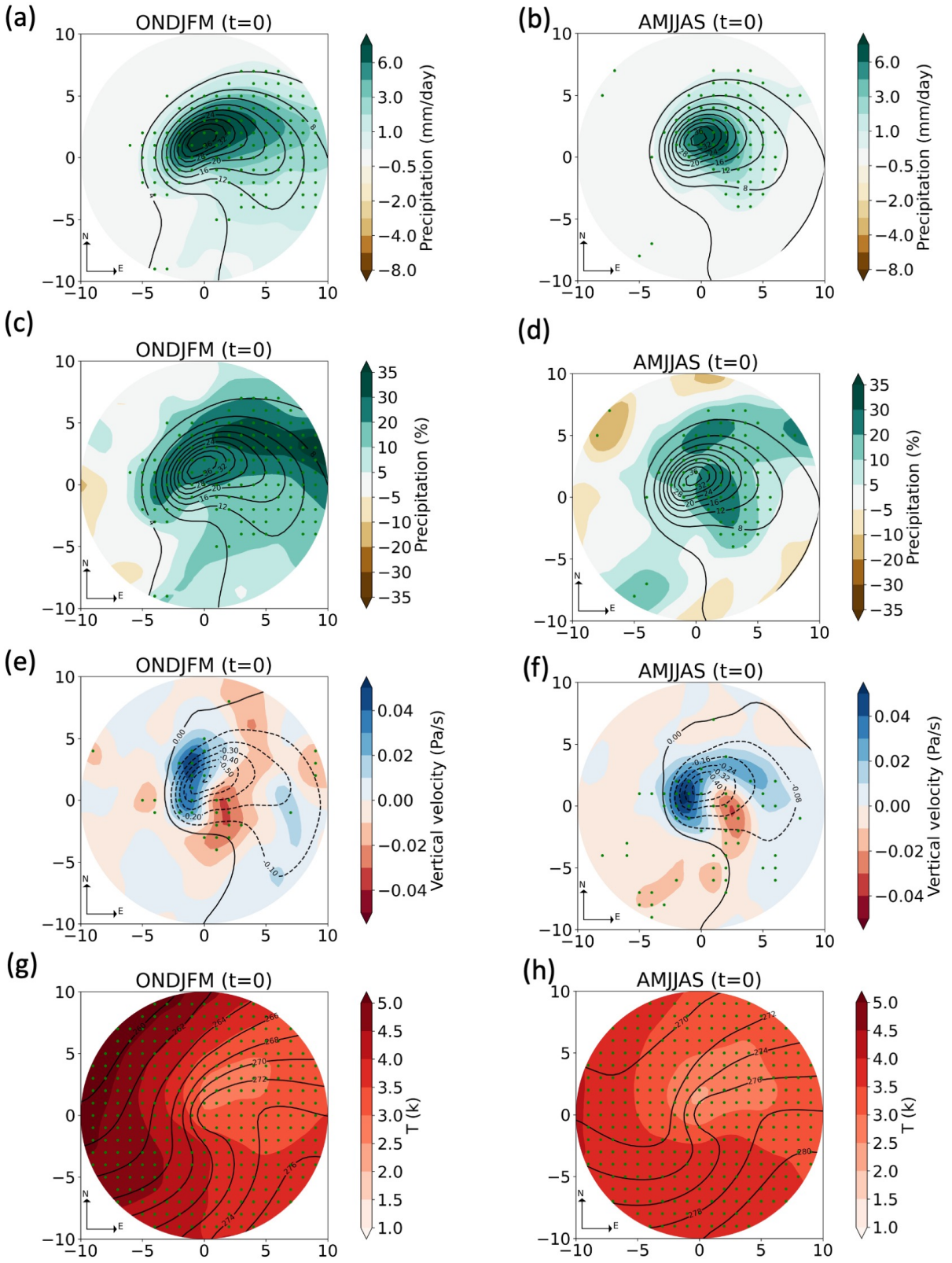

Figure 4.6: Cyclone (a,b,c,d) precipitation, (e,f) vertical velocity at 850 hPa and (g,h) temperature at 850 hPa composites response for (a,c,e,g) winter and (b,d,f,h) summer in the North Atlantic. Present-day mean for each field is overlaid as black contour lines. The composites are at the time of maximum intensity (time=0).

Furthermore, the vertical velocity is shown in Figs. 4.6e and 4.6f. In general, the ascent increases to the east of the cyclone center and decreases to the west of the cyclone center. Thus, the ascent will be enhanced farther away from the cyclone center, over the warm region, probably associated with the WCB activity. However, there are some regions with more complex patterns. For example, during winter (Fig.4.6e), the ascent increases to the northeast of the cyclone center, which corresponds to the warm front region. As discussed before, the warm front is a region of substantial precipitation increase. We expect that the increase of the ascent will produce an amplification of the precipitation in that region.

In summer, the anomalies of vertical motion have a different spatial distribution (Fig. 4.6f). For instance, a region of enhanced ascent is located in the cold front sector. A region of reduced ascent wraps around the cyclone center from the north to the west.

A stronger forcing for precipitation formation by vertical motion in some cyclone regions (adding up to the moisture increase), resulting in amplified precipitation, was also mentioned in the previous study by Michaelis et al. (2017). This amplified ascent can be related to temperature advection aided by enhanced wind speed (Michaelis et al., 2017). Sinclair et al. (2020) used an idealized global model to simulate the response of cyclones to the warming climate and found that the ascent increases by diabatic heating and modified thermal advection produce a displacement of the warm front ascent region. In contrast, increases in ascent due to vorticity advection produce the downstream spread. The dynamic and thermodynamic contributions to the future amplification of cyclone precipitation will be analyzed in chapter 7.

The temperature response at 850 hPa in winter is shown in Fig. 4.6g. The most significant increase is found upstream (west of the cyclone center), over the cold area, which means a reduction in the temperature gradient and therefore reduced baroclinicity. In isolation, this would lead to a reduction of the cyclone intensity. Note that the smallest increase is projected over the warm front. We can also observe that the maximum temperature increase at 850 hPa is around 5 ^{o} K, similar to the global mean surface temperature change in the model. However, the temperature increase over the warm region is around 3 ^{o} K. A smaller temperature increase compared to the global mean is associated with the fact that intense cyclones are located over the ocean, where the warming is smaller compared to the continents.

On the contrary, the temperature increase in summer is smaller than in winter (Fig. 4.6h). However, the largest increase is also to the west of the cyclone center. A comparable increase is located to the south of the cyclone center. This might suggest that the fronts will turn slightly cyclonically or will have a faster occlusion.

Changes in the composite patterns of the wind field and RV850 shown in figure 4.7 are indicative of projected future changes in cyclone structure and intensity. In winter, the relative vorticity changes (Fig. 4.7a) have an intricate spatial pattern, with a RV850 reduction near the cyclone center and RV850 increases to the northeast and southwest of the SLP minimum. This may indicate enhanced relative vorticity values near the cold

and warm fronts of intense cyclones in a warmer climate. Sinclair et al. (2020) found a similar spatial pattern in aquaplanet simulations.

Contrary to winter, we identify a clear intensity decrease over the cyclone center and warm region in summer (Fig. 4.7b). We also observe a smaller positive anomaly farther to the north and south of the cyclone center.

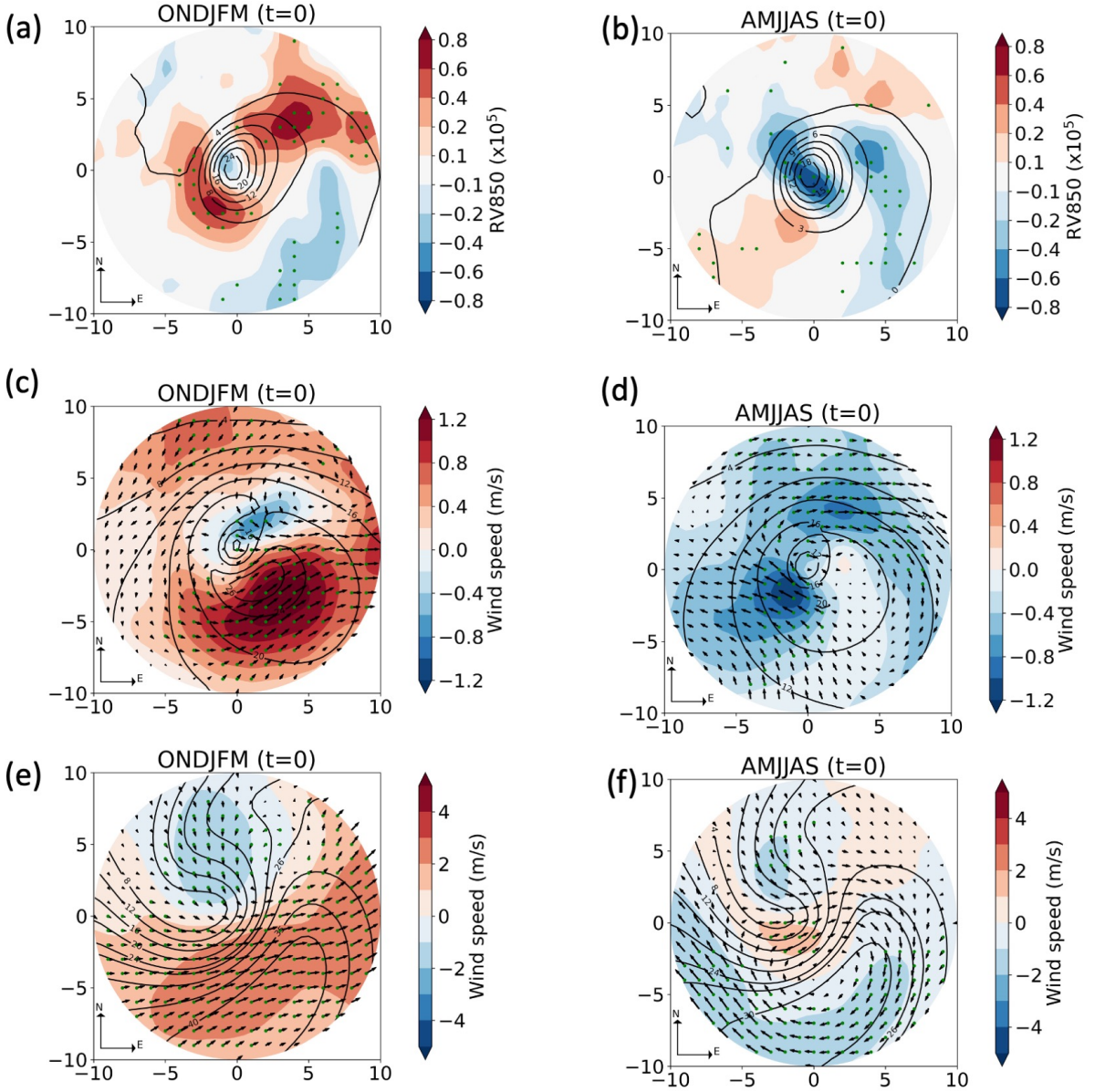

Figure 4.7: Cyclone (a,b) RV850, (c,d) wind speed at 850 hPa and (e,f) wind speed at 250 hPa composite response for (a,c,e) winter and (b,d,f) summer in the North Atlantic region. Present-day means for each field are overlaid as black contour lines. The composites are shown at the time of maximum intensity (time=0).

Figures 4.7c,d shows the wind speed changes at 850 hPa. A clear seasonal difference is observed. In winter, a slight decrease in wind speed is simulated north and northeast of the cyclone center, but in most other regions, wind velocities increase. The most significant increase emerges to the southeast of the center. This is related to a broadening of the footprint of strong winds (see again Fig. 4.7c) in a southeastward direction, further into the cyclones' warm sector. Similar enhanced winds have been found in the new CMIP6 climate projections (Priestley and Catto, 2022).

In summer, the wind speed decreases in most regions (Fig. 4.7d). The most significant decrease is located over the cold region, suggesting a weaker CCB. In the warm region, the changes are smaller. Accordingly, the LLJ maximum speed will not change significantly. This wind reduction at the lower level is consistent with the results found in the CMIP6 models (Priestley and Catto, 2022).

The wind speed changes at 250 hPa are shown in Fig. 4.7e. An increase in the wind velocity can be identified to the south and downstream of the cyclone center, linked to a more robust eastward flow and an enhanced jet stream. This increase is consistent with the mean response of the jet stream to enhanced upper-tropospheric meridional temperature gradients (Grise and Polvani, 2014, Shaw et al., 2016, Priestley and Catto, 2022).

On the contrary, in summer, the upper-level winds are projected to weaken (Fig. 4.7f). The main area of decreased wind speed is projected to the south of the cyclone center, over the jet streak.

Note that, at low levels, the wind increases are more robust than the decreases across the ensemble members (see the green dots in Fig. 4.7c), which might be due to small shifts in the location of the negative anomaly between ensemble members. In the following, in order to better understand the changes in cyclone dynamics that are related to these altered wind patterns, we investigate composite potential vorticity anomalies and their projected future changes.

4.3 PV analysis of intense cyclones

A qualitative framework to understand the relation between PV and extratropical cyclone dynamics and the role of LH is through three anomalous components in the PV-associated cyclone circulation: a positive upper-tropospheric PV anomaly, a positive potential temperature anomaly at the surface, and a positive lower-tropospheric PV anomaly (Davis and Emanuel, 1991, Davis, 1992). A more extended discussion of this PV framework is provided in chapter 1.

Here, we use the PV framework to analyze the future changes in cyclone dynamics. PV anomaly profiles are examined before and during the time of maximum intensity. In

addition, composites are investigated at low levels (700 hPa) and upper levels (250 hPa) at the time of maximum intensity. As in Pfahl et al. (2015) the hydrostatic approximation of Ertel PV is used:

$$q \approx -g[(-\frac{\partial u}{\partial y} + \frac{\partial v}{\partial x} + f)\frac{\partial \theta}{\partial p} + \frac{\partial u}{\partial p}\frac{\partial \theta}{\partial y} - \frac{\partial v}{\partial p}\frac{\partial \theta}{\partial x}], \tag{7}$$

where θ denotes potential temperature, u and v are the horizontal wind components, f is the Coriolis parameter, p is the pressure, and g is the acceleration due to gravity. The horizontal derivatives in the Equation are at constant pressure.

To first quantify simulated PV changes averaged over the cyclone area, figure 4.8 shows the PV anomaly profiles for intense cyclones in the North Atlantic region. At the time of maximum intensity (t=0, figure 4.8b,d), there are prominent positive PV anomalies in the lower and upper troposphere, as typically associated with intense extratropical cyclones (Grams et al., 2011, Čampa and Wernli, 2012, Pfahl et al., 2015, Büeler and Pfahl, 2017). The lower-tropospheric PV anomaly is primarily created by diabatic processes, such as latent heat released during cloud formation (Wernli and Davies, 1997, Ahmadi-Givi et al., 2004, Büeler and Pfahl, 2017, Müller et al., 2020). The upper-tropospheric PV anomaly is associated with adiabatic PV advection from the stratosphere and partly influenced by the cyclonic wind field linked to the lower-tropospheric PV anomaly (Hoskins et al., 1985, Wernli et al., 2002).

Figure 4.8a shows the PV anomaly profile 12 hours before the time of maximum intensity when both PV anomalies are still weaker and the low-level maximum is located at a higher pressure. Nevertheless, the low-level anomaly has a notable magnitude even 12 hours before the maximum intensity. High PV anomalies are also found at the upper levels. In the hours after the maximum intensity, the positive anomaly is more evident at the upper levels, above 400 hPa (not shown). As indicated by the blue lines in figure 4.8, the growth of the upper-tropospheric PV anomaly between t=-12 and t=0 goes along with a lowering of the dynamical tropopause.

As a response to climate warming, at the time of maximum intensity (t=0, Fig. 4.8b), there is a general increase in the lower and mid-tropospheric PV anomaly and a slight decrease in the upper-tropospheric PV anomaly. Note that the slight change in the upper-level anomaly is probably related to the relatively small averaging radius of 2.5°. Changes in the upper-level PV structure will become more evident in the composites discussed below. The amplification of the lower tropospheric PV anomaly is more robust in the layer between 850 and 600 hPa. These structural changes are similar to the previous finding of Büeler and Pfahl (2019) for intense cyclones based on idealized model simulations. For instance, also in these idealized simulations, the lower tropospheric PV maximum extends more into the middle troposphere in warmer climates. However, the magnitude of PV changes in the Büeler and Pfahl (2019) experiments are more prominent than in the CESM-LE simulations presented here. This is mainly because the range of climate

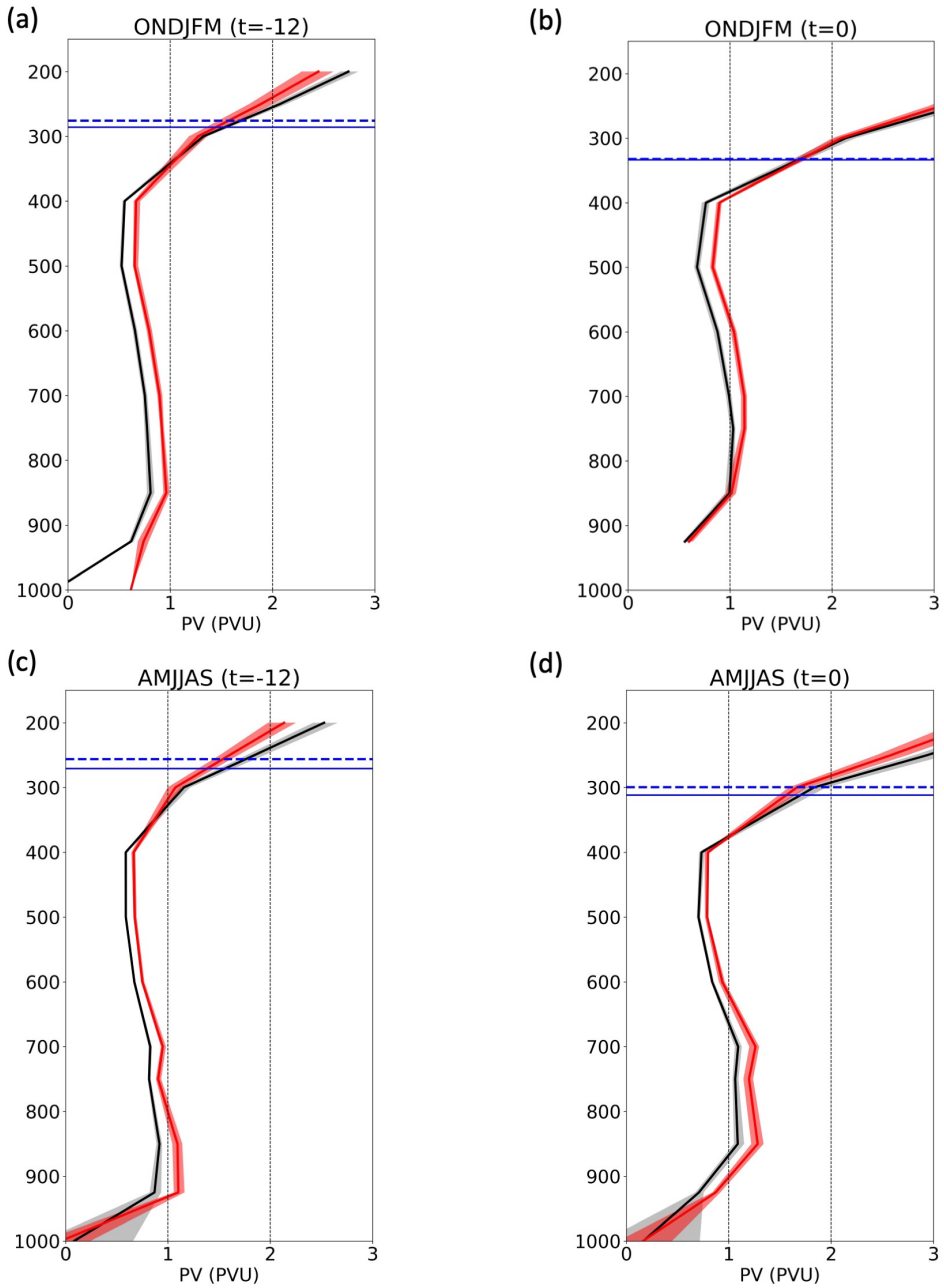

Figure 4.8: Vertical profiles of PV anomalies associated with intense extratropical cyclones in the North Atlantic region during (a,b) winter and (c,d) summer for present-day climate (1990-2000), shown as black lines, and future climate (2091-2100), shown as red lines. Anomalies are calculated with respect to a local PV climatology and averaged in a radius of 2.5° around the cyclone center. The solid blue lines indicate the 2-PVU tropopause in the presence of cyclones for present-day (solid line) and future (dashed line) climate. Composite profiles are shown (a,b) 12 hours before and (c,d) at the time of maximum intensity.

warming is much more extensive in the idealized simulations.

The positive PV anomaly in the lowest part of the troposphere (below 850 hPa) increases more in the hours before maximum intensity (Fig. 4.8a). This increase is likely related to a more considerable influence of cloud formation and precipitation processes prior to the maximum intensity (Pfahl and Sprenger, 2016), which agrees with an analysis of the precipitation life cycle that was presented in section 4.2.

After the maximum intensity, the PV changes are smaller, mainly restricted to the upper levels (above $\sim$ 600 hPa and 700 hPa for winter and summer, respectively).

Finally, figure 4.8 indicates that the height of the tropopause during the presence of intense cyclones is projected to increase slightly, which reflects the general increase in tropospheric depth in a warming climate (O'Gorman and Schneider, 2008, Pfahl et al., 2015). This increase is more evident 12 hours before the maximum intensity (Fig. 4.8a,c).

Figure 4.8c,d also indicates some seasonal differences at the time of the maximum intensity in the lower-tropospheric PV anomaly. For example, in winter, the maximum PV anomaly is located around 850 hPa in the present-day climate. It moves near 750 hPa in the future, which corresponds to an upward displacement (in addition to the amplification). Meanwhile, in summer, we identify only a general amplification. Another difference is found before the maximum intensity at the lower levels (925 hPa); in the summer season, the PV increase is larger than in the winter season.

In the following, the horizontal structure of cyclone-related PV anomalies is also analyzed with the help of composites. Note again that a PV climatology specific to the respective climate (present-day vs future) has been subtracted from the full PV fields to obtain these anomalies. As shown in figure 4.9c,d, there is a clear, diabatically created maximum in the PV anomaly at 700 hPa near the cyclone center, which extends downstream in the region of the warm front. A secondary maximum can be observed along the north-western flank of the composite region. The second maximum is likely related to frictional PV generation over the land masses such as Greenland and North America that are located to the north-west of the North Atlantic storm track (see again Fig. 4.2).

The upper-tropospheric PV anomaly shown in figure 4.9a,b follows a dipole pattern, with high PV values associated with an upstream trough in the western part of the composite and a maximum south-west of the cyclone center. A clear signature of cyclonic wave breaking can be observed, which is also linked to the formation of the jet streak (see again Fig. 4.5e,f). This PV anomaly pattern is typical for extratropical cyclones during their mature stage of development (Pinto et al., 2014, Houze Jr, 2014, Michaelis et al., 2017). Moreover, it is a signature of the deepening processes of the upper level PV, which leads eventually to the "treble clef" upper level PV distribution characteristic of a warm-occluded structure in the lower troposphere (Martin, 1998, Tamarin and Kaspi, 2016)

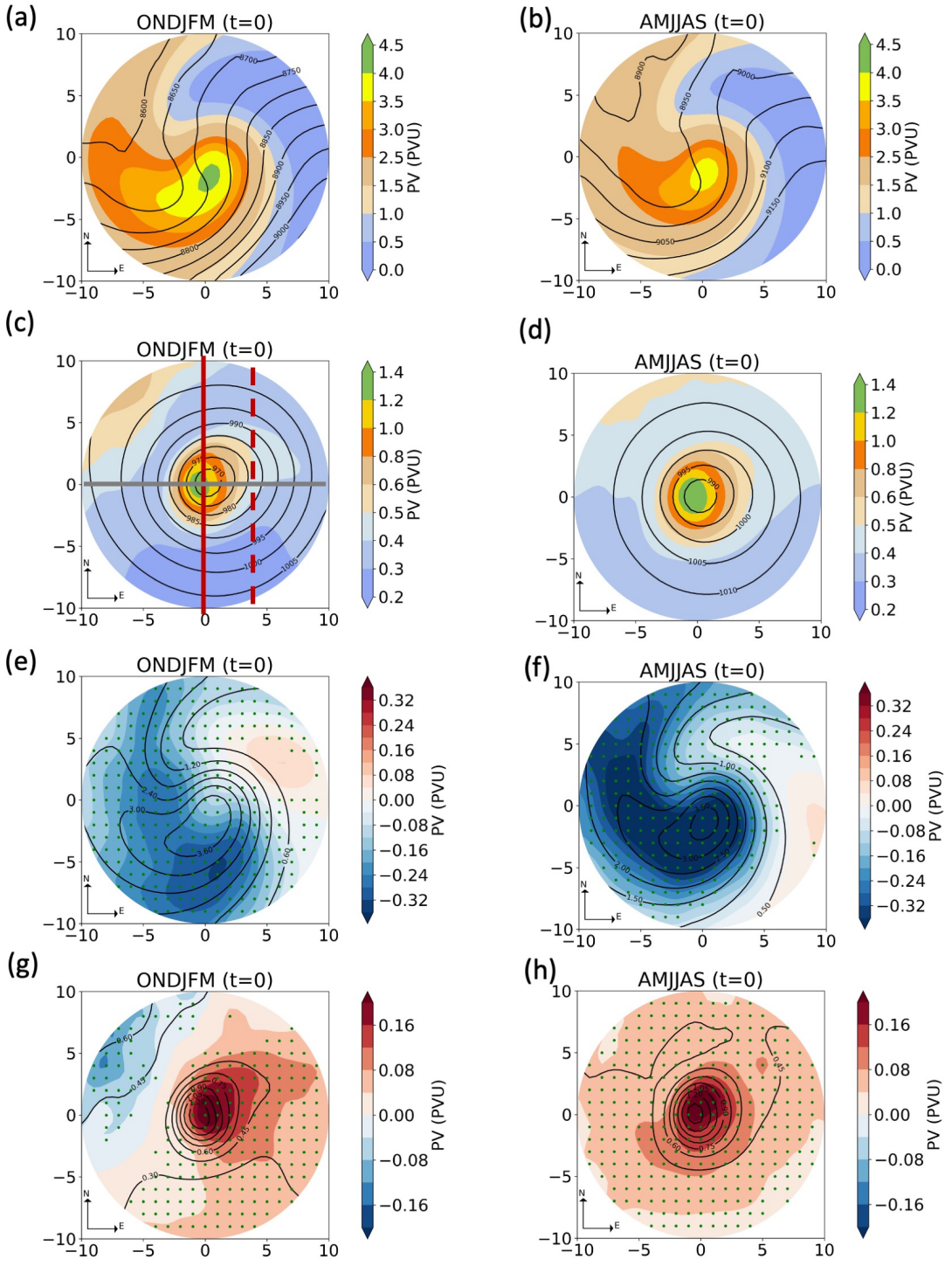

Figure 4.9: Present-day composites for intense cyclones of (a,b) PV at 250 hPa and (c,d) PV at 700 hPa and (e,f,g,h) their future change for (a,b) winter and (c,d) summer in the North Atlantic region. Mean SLP (hPa) is overlaid as black contour lines in (c,d) and geopotential height (m) is overlaid as black contour lines in (a,b). The present-day mean of each field is overlaid as black contour lines in (e,f,g, h). Green dots in (e,f,g,h) denote regions of ensemble agreement on the sign of change, i.e., more than 80% of the ensemble members indicate a future change of the same sign. The composites are shown at the time of maximum intensity (time=0).

In summer, higher PV anomalies are found at lower levels, while smaller PV anomalies dominate the upper levels. Additionally, seasonal differences in the spatial distribution are found at the lower levels. For instance, PV gradients are stronger in winter than in summer to the south of the cyclone center.

The vertical velocity is related to diabatic heating through the omega equation of an environment in quasi-geostrophic balance (Räisänen, 1995, Holton and Hakim, 2012, Rantanen et al., 2017). The relationship between the omega equation and potential vorticity has been explored in previous studies (Hoskins et al., 2003, Dixon et al., 2003, Funatsu and Waugh, 2008, Liu et al., 2020). The vertical velocity can physically be decomposed into the sum of the isentropic displacement and isentropic upglide. The first is associated with diabatically forced vertical motion, and the second is associated with a quasi-horizontal motion of a particle moving along a sloping isentropic surface (Funatsu and Waugh, 2008, Liu et al., 2020). The maximum ascent in the cyclone composites (see again Fig. 4.4c,d) is located along the maximum lower-tropospheric PV (slightly to the north of this maximum). This relation will be explored in the next section with cross-sections in different cyclone regions.

Future changes of lower-tropospheric composite PV anomalies are shown in figure 4.9g,h. Positive PV anomalies are projected to increase in the region of the present-day maximum, near the cyclone center, but also downstream in the region of the warm front and generally in the area of the cyclone's warm sector (note that PV anomalies also increase in the cold sector in summer). This increase, in both seasons, is consistent with an increase in precipitation over the warm sector and with the overall rise of atmospheric moisture content, cyclone-precipitation and thus latent heat release in a warmer climate (Schneider et al., 2010, Yettella and Kay, 2017). Similar increases in lower-tropospheric PV have been found in other studies (e.g. Marciano et al., 2015, Michaelis et al., 2017, Zhang and Colle, 2018, Sinclair et al., 2020) and have been directly attributed to enhanced latent heat release in idealized simulations (Büeler and Pfahl, 2019). In winter, increases in lower-tropospheric PV over the warm sector correspond with an increase in relative vorticity (cf. Fig. 4.7a) in some areas, such as near the warm front, but not everywhere, pointing towards a complex relationship between PV and wind changes that will be further discussed below. Moreover, PV at 700 hPa is projected to decrease in the region of the secondary maximum at the northwestern edge of the composite in winter. This might be related to the eastward shift of the intense cyclone tracks in the northeastern Atlantic (see again Fig. 4.2c), which brings them further away from Greenland's topography.

Based on the quasi-geostrophic balance assumption, a positive PV anomaly is associated with ascent on its eastern and descent on its western flank (Hoskins, 1997). A similar response can be found in the vertical wind composite 4.6e,f. Thus, it is possible to associate the enhanced LH release with enhanced ascent downstream.

The upper-level PV anomaly is projected to decrease in most regions but in particular upstream and south of the cyclone center (Fig. 4.9e,f). During summer, the largest reduction is aligned with the maximum upper-tropospheric PV of the present-day climate.

In winter, the most substantial reduction occurs along the southern flank of the PV maximum, pointing to a decreased cyclonic wave breaking. A small PV increase is found downstream of the cyclone center, which is, however, hardly consistent across the ensemble member.

A similar reduction of upper-tropospheric PV has been found by Michaelis et al. (2017). In winter, parts of the PV decrease may be explained by changes in meridional PV advection. For instance, the slight increase in southerly upper-level wind velocities over the warm sector (see again Fig.4.7e) may go along with enhanced advection of low-PV air masses from lower latitudes. In addition, an upward shift of the dynamical tropopause might contribute to such a PV decrease, although this tropopause shift is very small in the cyclones investigated here (see again Fig. 4.8) and thus not sufficient to explain the entire PV decrease. Finally, also enhanced LH at lower levels may impact the upper-level PV distribution through amplified upward motion and negative diabatic PV tendencies above the level of maximum heating. Michaelis et al. (2017) showed that this might lead to negative PV changes northeast of the cyclone center prior to (but not at) the time of maximum cyclone intensity. We will investigate the complex interplay between diabatic PV changes and PV advection (see also Brennan et al., 2008, Madonna et al., 2014) in chapter 6 using a Lagrangian approach.

The enhanced diabatic heating in a warmer and therefore more humid climate may thus influence PV anomalies and cyclone dynamics at both lower and upper levels. At low levels, it generates sizeable positive PV anomalies that directly contribute to cyclone intensification. This qualitative discussion will be completed by quantitative PPVI results in chapter 5.

Cyclone cross-sections during winter

We study vertical cross-sections in different cyclone regions to analyze the vertical circulation associated with the PV anomalies and their future changes during winter. Winter is chosen to be able to compare the circulation response to the PV anomalies with previous studies (Marciano et al., 2015, Michaelis et al., 2017, Zhang and Colle, 2018, Catto et al., 2019, Sinclair et al., 2020), which, for instance, found an enhanced LLJ and ascent downstream of the cyclone center.

Vertical cross-sections of PV, vertical and horizontal wind speed are shown in Fig. 4.10. Cross-section west to east (WeEa) are shown in panels 4.10a and 4.10b. In the present-day climate, a PV tower (Grams et al., 2011) is evident over the cyclone center. Two maxima of horizontal wind speed are found at the low levels, the first to the west and the second to the east of the PV tower. The maximum ascent is located near the cyclone core and slopes slightly westward with height (maybe associated with the occlusion and CCB). A secondary maximum of ascent is located to the east, which could be associated with the WCB. This configuration fits with the theory of extratropical cyclones from a PV perspective (Lackmann, 2011). The upper-level jet streak can be identified at the

eastern flank of the cyclone with horizontal wind velocities around 35 m/s.

A clear PV tower is also found in the cross-section south to north (SoNo) (Fig. 4.10c). Nevertheless, the maximum ascent is slightly displaced poleward. The two maxima of horizontal wind speed in the low levels around the PV tower are also evident. The maximum horizontal wind speed is more extensive to the south of the cyclone center, likely related to the LLJ. In the upper levels, the jet streak is located to the south of the cyclone center.

The future response to the cross-section WeEa is shown in Fig. 4.10b. The PV increase covers the PV tower from the surface to the mid-levels. The PV has the largest increase over the cyclone center. The increase extends eastward towards the warm region. The strongest PV decreases are found at upper levels. Nevertheless, there is a decrease on the western side of the PV tower near surface.

The vertical motion seems to respond to the PV anomaly response following the quasi-geostrophic balance (Fig. 4.10b). In particular, the ascent is amplified to the east and reduced to the west of the cyclone center, as also discussed in the previous section. Note that the ascent reduction upstream has a larger magnitude.

The horizontal wind speed has a more complex pattern, but we can identify a wind speed increase at the mid-levels to the west of the cyclone center. At the upper levels, the wind speed also seems to increase with the largest increase over the jet streak.

Fig. 4.10d shows the future response in the SoNo cross-section. A dipole pattern is found on the northward flank of the main region of ascent. The ascent is reduced at lower levels, while ascent is enhanced just below and at the tropopause.

The horizontal wind speed is projected to increase to the south of the cyclone center (Fig. 4.10d). The increase means a stronger jet streak at upper levels and a stronger LLJ at low levels.

Finally, the strong PV anomaly increase in the northern part of the cross-section at low-mid levels and the reduction below the tropopause is in accordance with the PV erosion hypothesis. In particular, the strongest PV reduction at the tropopause levels is found above the region of amplified ascent, where most likely also the latent heat release increases due to this stronger upward motion. However, there are regions (south of the cyclone center, and also to its west in the WeEa cross-section, Fig. 4.10b) where the reduction does not appear to be produced by PV erosion, either the entire PV column tends to reduce or the PV decrease is located above a region of descent.

We also investigate the PV anomalies associated with the circulation over the WCB sector. Catto et al. (2010) suggested that this WCB region is located at 4^o to the east of the cyclone center. We compared the horizontal wind fields in our composites to the results of Catto et al. (2010) and found a similar pattern (not shown). For example, the WCB is

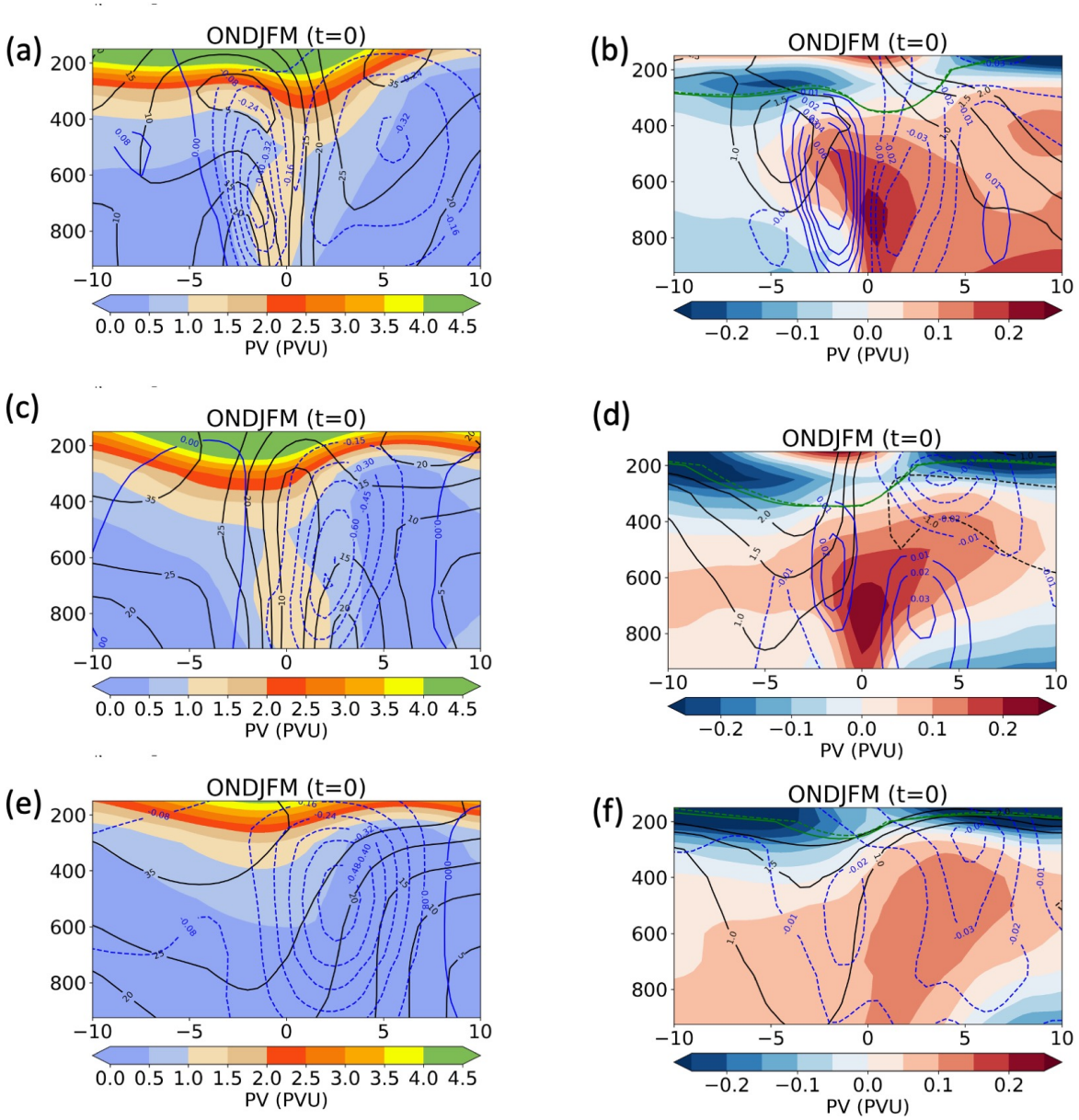

Figure 4.10: (a,c,e) Vertical cross-sections in present-day climate and (b,d,f) their future response composites. (a,b) cross-section from west to east (grey line in Fig. 4.9c). (c,d) cross-section from south to north (red line in Fig. 4.9c). (e,f) cross-section in the WCB region (dashed red line in Fig. 4.9c). PV (shaded colors), wind speed (m/s, black contour lines) and omega (Pa/s, dashed blue lines) The tropopause is shown in present-day (green solid line) and in future (green dashed line) climate . The composites are shown at the time of maximum intensity (time=0).

located ahead of the LLJ maximum speed. Thus, we created cross-sections at the same location to analyze if the circulation corresponds to the WCB regime and then analyze its response to the warming climate.

The cross-sections in the WCB region are shown in Figs 4.10e,f In the present-day climate, the vertical motion is upward over the entire area. We can identify the zone of maximum ascent at mid-levels to the north of the cyclone center. Below this maximum ascent, a region of high moisture content can be identified (not shown), which is related to the WCB. Moreover, the higher temperatures at low levels to the south of the cyclone center (not shown) complete the features discussed by Catto et al. (2010). We also observe a strong jet streak to the south of the cyclone center as well as a strong LLJ. Therefore, the characteristics correspond to WCB activity.

We continue with an analysis of the WCB circulation changes in a warming climate (Fig. 4.10f). The maximum PV increase is found at mid-levels, northward of the cyclone center. A northward and upward extension of the region of strongest ascent is evident. According to Sinclair et al. (2020) this extension and enhanced ascent can be associated with diabatic heating. It is linked to enhanced precipitation over the warm front in the winter season as the climate warms. A stronger LLJ over the southern part WCB region can also be expected. A detailed Lagrangian analysis of the air streams will be performed in chapter 6.

4.4 Discussion

In this chapter, we have analyzed the general structure of intense extratropical cyclones in present-day climate and its future change in the North Atlantic region. Different fields have been explored at the time of maximum intensity, and the main findings are discussed below.

Precipitation intensity will increase at the cyclone center and over the downstream region. A remarkable precipitation increase is located over the warm front during the winter, indicating that changes in dynamic process might play a role in modifying precipitation distribution and amplification in a warming climate. A poleward and downstream expansion of the rain band associated with the warm front is also found, similar to previous studies (Sinclair et al., 2020).

In addition, the vertical velocity is projected to change following a dipole pattern, that is, a stronger ascent to the east of the cyclone center and a weaker ascent to the west of the cyclone center. Other regions of enhanced upward motions are to the northeast of the cyclone center in winter while stronger ascent will dominate to the south of the cyclone center in summer. Those changes can probably be related to the enhanced precipitation over the frontal regions. The role of the dynamics in the enhanced precipitation will be further investigated in chapter 7.

A weaker temperature gradient will be expected in the future, thus explaining the lack of stronger cyclones. The temperature at 850 hPa also reveals a possible faster front occlusion in summer.

Cyclone intensity changes have been analyzed in terms of RV850 and wind speed. In winter, we have identified an increase in near-surface wind speed to the south of the cyclone center. Besides, wind speed composite also shows a larger footprint of enhanced winds downstream of these strong winds. Therefore, an enhanced low-level jet will be expected. On the contrary, the intensity of wind speed at low levels will decrease in summer.

Winter wind increases as a response to the warming climate are more evident in Fig. 4.11. The maximum wind speed increase is clear during and after the maximum intensity (Fig. 4.11a). Note that such an increase in wind speed is not evident in Fig. 3.8c, which is mainly related to the fact that we have considered intense cyclones and that a bigger radius has been chosen. As discussed above, the stronger low-level jet may be associated with the CCB and WCB because these air streams have a large influence on the LLJ during the mature stage of the cyclones (Hewson and Neu, 2015). The larger LLJ footprint and slight displacement downstream are shown in Fig. 4.11b.

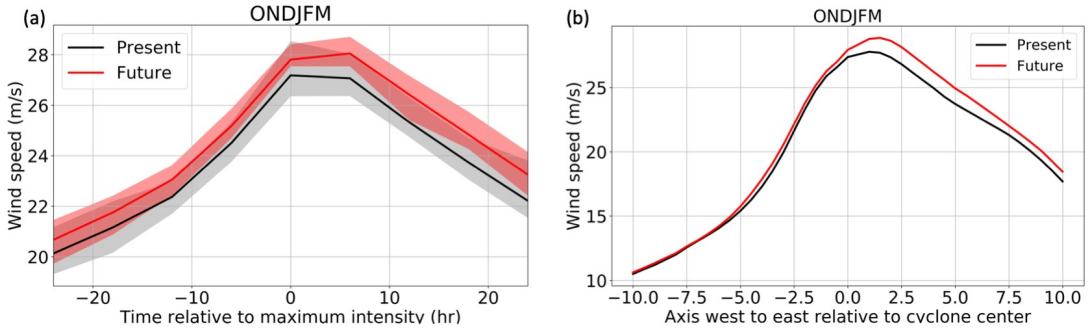

Figure 4.11: (a) Maximum wind speed composite cyclone lifecycle for the winter in the North Atlantic. The black line represents present-day (1990-2000) and the red line represents future (2091-2100) climate. The maximum wind speed is calculated within 8^o of the cyclone center. (b) Wind speed at 3^o to the south of the cyclone center.

From the PV analysis, we obtain some insights into the role of diabatic processes for extratropical cyclones over the North Atlantic in a warming climate with the help of the composites and profiles of the potential vorticity.

Lower and upper tropospheric PV changes were examined. The fact that the maximum intensity occurs after enhanced rain rates imply that the diabatic heating is an important mechanism contributing to cyclone intensification in a warming climate(Marciano et al., 2015). A larger positive PV anomaly driven by LH is observed in the PV profiles between lower and middle levels. The composites at 700 hPa reveal an increase in PV over the cyclone center and downstream area. The upper tropospheric PV also seems to be affected

by the enhanced latent heat. The latent heat increase might erode the UPV in some regions, resulting in a reduction of PV anomaly. However, over other regions, an altered advection probably plays a more important role. In the next chapter, we use piecewise PV inversion to analyze the cyclone circulation associated with the PV anomalies.

The relation between the PV and the vertical motion response seems more evident in the cross-sections. Increased PV at middle levels produces a stronger ascent to the east of the cyclone center while weaker ascent is located to the west of the cyclone center. In addition to the northward and eastward extension during winter, the maximum ascent over the WCB region will also move upward. An explicit analysis of the airstreams will be discussed in chapter 7.

5 PPVI analysis of extreme extratropical cyclones

As discussed in chapter 4, also CESM-LE simulations predict an increase in diabatic PV anomalies in a warmer future climate. As the PV anomaly in the lower troposphere is primarily related to diabatic processes, increased LH is expected to result in an intensification of this anomaly. Accordingly, an increase in lower-tropospheric PV in midlatitude cyclones has been detected in idealized model simulations (Pfahl et al., 2015, Büeler and Pfahl, 2019, Sinclair et al., 2020) and climate change studies with regional models (Marciano et al., 2015, Michaelis et al., 2017, Zhang and Colle, 2018). One way to identify the influence of altered LH on cyclone dynamics is via the PV framework. Tamarin and Kaspi (2017) and Tamarin-Brodsky and Kaspi (2017), using PV inversion, showed that such diabatically induced low-level PV increases contribute to an enhanced poleward motion of cyclones as the climate warms. Nevertheless, it is not clear how (diabatic) PV changes link to structural changes in other impact-relevant cyclone properties such as low-level wind velocity. This is one of the central questions of the present chapter.

5.1 Data and methods

Piecewise PV inversion

Piecewise potential vorticity inversion (PPVI) can be used to examine the contributions of PV anomalies (q') to the wind field of an extratropical cyclone (Davis and Emanuel, 1991, Tochimoto and Niino, 2016). For a suitable set of balance and boundary conditions, the invertibility of PV allows the derivation of wind and geopotential height fields from the PV distribution (Hoskins et al., 1985, Seiler, 2019)

With PPVI, q' in extratropical cyclones is commonly partitioned into three layers: the surface layer, the lower atmospheric layer, and the upper atmospheric layer (Seiler, 2019). The inversion may then be utilized to investigate the relative contributions of the PV anomalies in these layers to the flow field at specific levels (Tamarin and Kaspi, 2016, Teubler and Riemer, 2016, Tamarin-Brodsky and Kaspi, 2017) or to extratropical cyclone intensity (Seiler, 2019). Ertel (1942) defines PV as

$$q = \frac{1}{\rho}\vec{\eta} \cdot \nabla\theta \tag{8}$$

where q is PV, ρ is the air density, $\vec{\eta}$ is the absolute vorticity, θ is potential temperature, and ∇ is the three-dimensional Nabla operator.

The PV inversion code used here is based on Davis and Emanuel (1991) and Davis (1992), but was strongly modified by Teubler and Riemer (2016). Nonlinear balance (Charney, 1955) assumes that the wind's irrotational component is substantially smaller than the magnitude of the nondivergent wind (e.g. Davis, 1992, Seiler, 2019). Therefore, geopotential (Φ) as a function of the non-divergent streamfunction (Ψ) and Ertel's PV can be expressed in spherical coordinates (Davis and Emanuel, 1991, Davis, 1992):

$$\nabla^2\Phi = \nabla \cdot f\nabla\Psi + \frac{2}{a^4 cos^2\phi}\left[\frac{\partial^2\Psi}{\partial\lambda^2}\frac{\partial^2\Psi}{\partial\phi^2} - \left(\frac{\partial^2\Psi}{\partial\lambda\partial\phi}\right)^2\right] \tag{9}$$

and

$$q = \frac{g\kappa\pi}{p}\left[(f+\nabla^2\Psi)\frac{\partial^2\Phi}{\partial\pi^2} - \frac{1}{a^2\cos^2\phi}\frac{\partial^2\Psi}{\partial\lambda\partial\pi}\frac{\partial^2\Phi}{\partial\lambda\partial\pi} - \frac{1}{a^2}\frac{\partial^2\Psi}{\partial\phi\partial\pi}\frac{\partial^2\Phi}{\partial\phi\partial\pi}\right] \tag{10}$$

respectively, where Φ is the geopotential, Ψ is the non-divergent streamfunction, λ is longitude, ϕ is latitude, a is the radius of the earth, $\kappa = R/C_p$ is the Poisson constant, f is the Coriolis Parameter, p is pressure, and $\pi = (p/p_0)^\kappa$ is the Exner function.

Solving 9 and 10 for the unknowns Φ and Ψ, given q on a limited domain conduces to the full PV inversion (Davis and Emanuel, 1991). Regarding boundary conditions, Φ and Ψ are prescribed on the lateral domain boundaries (Dirichlet boundary conditions) and their vertical derivatives on the horizontal boundaries (Neumann boundary conditions). On the lateral boundaries, the observed geopotential is employed as the boundary condition for Φ and $\frac{\partial\Phi}{\partial\pi} = -\theta$ is used at the top and bottom of the domain (for more details see Davis, 1992).

At each grid point, PV anomalies are calculated as deviations from the PV background, defined here as a running mean over a 30 day time slice. A full PV inversion is computed for instantaneous values (q) and for 30-day mean values ($\bar{q}$), conducting to instantaneous balanced Φ and Ψ, and mean balanced $\bar{\Phi}$ and $\bar{\Psi}$.

The PV inversion is performed for the time of maximum intensity for each cyclone track and in a three-dimensional box bounded by the 900 and 100 hPa pressure surfaces, with a horizontal dimension of 30^o longitude, 15^o latitude around the cyclone center of interest. Furthermore, PV anomalies q' in upper- and lower-tropospheric layers are considered separately from each other (right column in Fig. 5.1): the upper layer between 550 and 150 hPa, the lower layer between 850 and 600 hPa and the lower boundary contribution at 875 hPa. Note that in the lower layer contribution, the PV anomalies and potential temperature at the boundary are separated, but the upper layer contribution contains both, PV anomalies and temperature at the upper boundary. The separation level between these anomalies (600 hPa) is consistent with the transition of the shape of the PV features

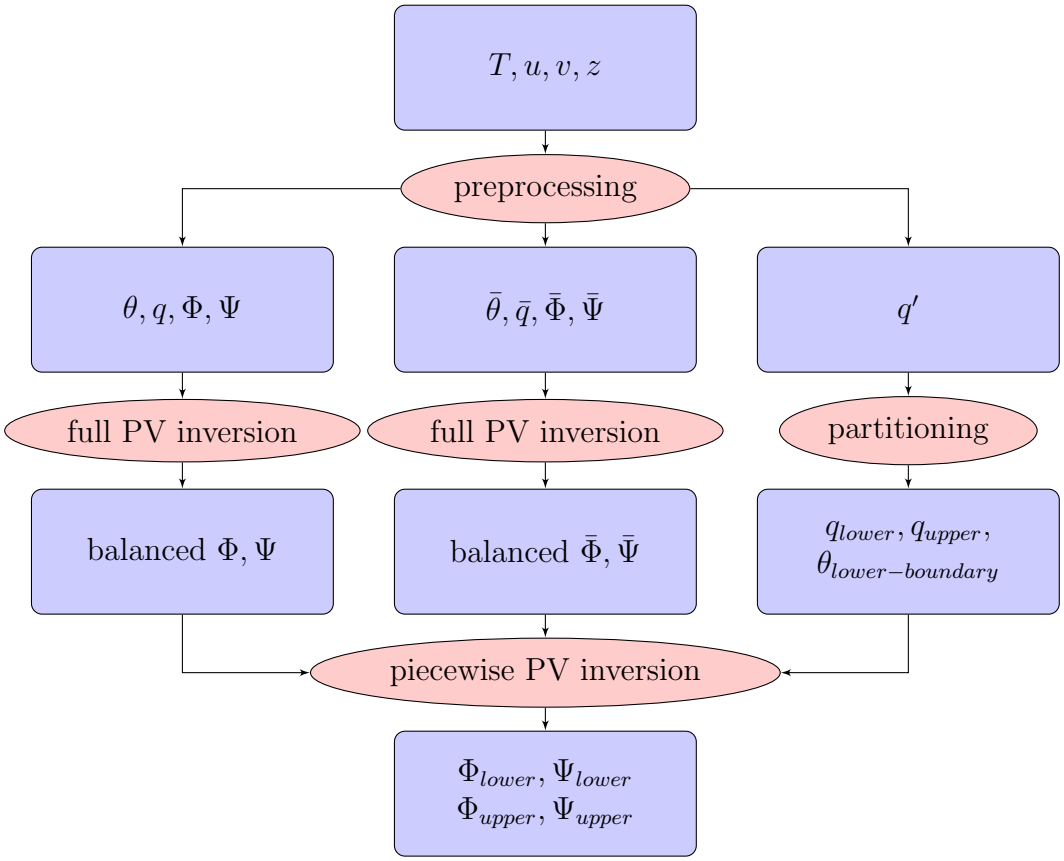

Figure 5.1: Algorithm for computing the piecewise potential vorticity inversion. Rectangles indicate variables, including temperature T, zonal wind speed u, meridional wind speed v, geopotential height z, potential vorticity q, geopotential Φ, and streamfunction Ψ, and ovals show steps of the calculation. Adapted from Seiler (2019).

from lower to higher levels (see Supplementary Fig. C.1). See figure 5.1 for a general overview of the PPVI algorithm.

The CESM-LE output is provided on hybrid sigma-pressure coordinates and, for the PPVI, is interpolated to equidistant isobaric levels ($\Delta P = 50hPa$) between 1000 and 50 hPa. Furthermore, in regions of high topography, the data are extrapolated below the ground. Following Davis and Emanuel (1991), temperature is extrapolated using a constant lapse rate (moist), then the geopotential is obtained by using the hydrostatic equation and state equation. Finally, the missing wind components (u,v) below the ground are filled by propagating the last value available downward.

Because of the computational effort, the piecewise PV inversion is not performed for all cyclones mentioned above (the 10% strongest), but only for the 1% strongest cyclones, which are denoted as extreme cyclones in the following.

5.2 PV analysis of extreme cyclones

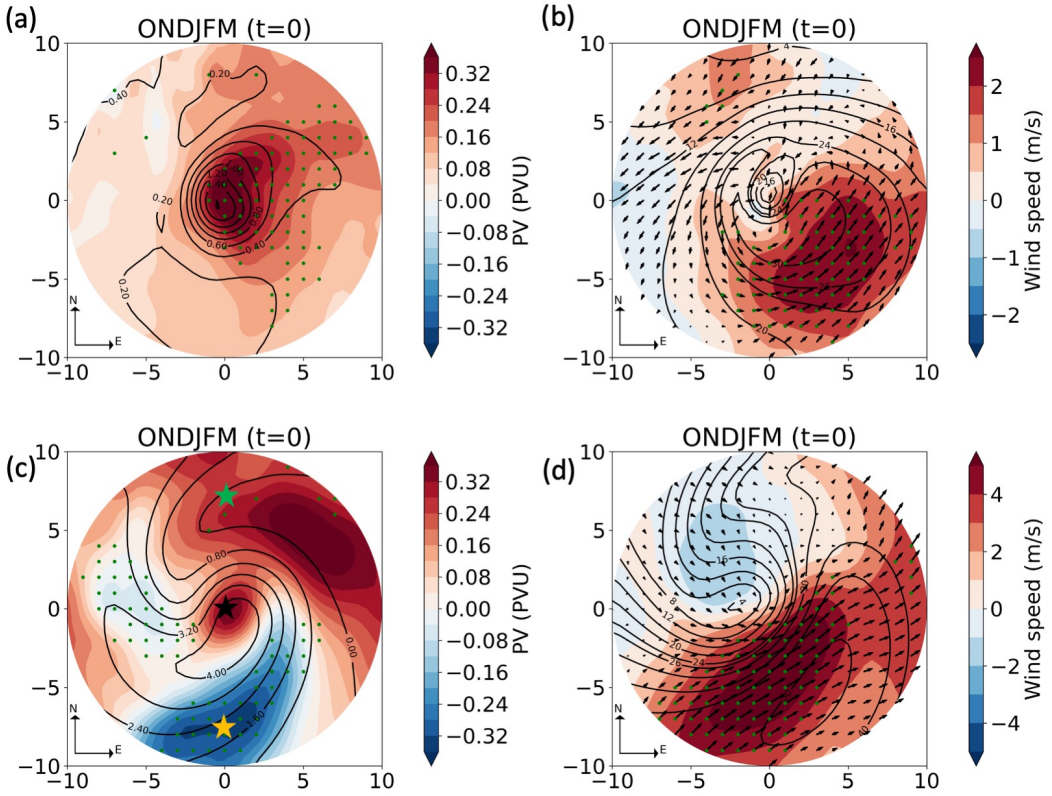

Figure 5.2: Future change in composites for extreme cyclones of a) PV at 700 hPa, b) wind speed at 850 hPa, c) PV at 250 hPa and d) wind speed at 250 hPa for winter in the North Atlantic region. The present-day mean of each field is overlaid as black contour lines. Green dots denote regions of ensemble agreement on the sign of change, i.e., more than 80% of the ensemble members indicate a future change of the same sign. The composites are shown at the time of maximum intensity (time=0). Extreme cyclones are defined as the 1% strongest systems in terms of maximum RV850.

Due to the relatively high computational effort, PPVI is not performed for all intense cyclones, but only for the 1% strongest cyclones in the 10 ensemble members are analyzed, which are referred to as extreme cyclones here. In this way, the focus is laid even more on the strongest storms with potentially largest impacts in terms of near-surface wind velocities. Before we show the PPVI results, we thus briefly discuss composite PV and wind changes associated with these extreme cyclones.

In the lower troposphere, the future changes in PV and wind composites of extreme cyclones (Fig. 5.2a,b) reproduce the main features of the corresponding composite changes of intense cyclones (cf. Figs. 4.9g and 4.7c), in particular regarding the regions of PV and wind speed increases that are consistent across ensemble members. Nevertheless, differences between extreme and intense cyclones are found in the magnitude of changes. For example, the wind magnitude increases by up to 1.2 m/s for intense cyclones, but

by up to 2.5 m/s for extreme cyclones. In addition, the region of strong wind increase reaches further to the southeast for extreme cyclones, i.e., the wind footprint is even further enlarged, and there is a stronger poleward component in the wind change for extreme cyclones. Also, the maximum magnitude of (diabatic) PV changes is about twice as large for the extreme as for the intense cyclones. These results further support the hypothesis that the strengthening of the low-level winds can be associated with diabatic potential vorticity increase: a larger amplification of diabatic PV generation in extreme cyclones goes along with a larger increase also in wind speed.

In contrast to the lower troposphere, upper-level PV changes for extreme cyclones differ more substantially from the intense cyclone changes. For instance, figure 5.2c indicates an upper-level PV increase near the cyclone center, where a decrease is projected for intense cyclones (Fig. 4.9d). However, this increase is not robust across ensemble members. A PV reduction to the south and west of the cyclone center, on the other hand, is common in both extreme and intense cyclones. Upper-level wind speed changes for extreme cyclones (Fig. 5.2d) again follow a similar spatial pattern as for intense cyclones (Fig. 4.7e) with amplified magnitude. Similar to the lower levels, the wind change in the region of the main jet has a more pronounced poleward component in extreme cyclones.

All together, this comparison indicates that, at lower levels and with regard to upper-level winds, changes in extreme cyclones are qualitatively similar to changes in intense cyclones. There are some differences in the behavior of the two cyclone classes in terms of projected upper-level PV changes, which can, however, be partially attributed to natural climate variability (as they are not robust across the ensemble of model simulations).

5.3 PPVI of extreme extratropical cyclones

A piecewise inversion is performed to quantify the relative contributions of upper and lower level PV anomalies to projected future wind speed changes in extreme cyclones and thus complement the previous qualitative discussion. The usefulness of such an inversion method to explain wind changes has been demonstrated in previous studies (e.g. Tochimoto and Niino, 2016, Tamarin-Brodsky and Kaspi, 2017).

As described in section 5.1, the PPVI separates the troposphere into an upper and a lower layer, and the effect of PV anomalies in each layer is separately evaluated. Figure 5.3 shows PV composites averaged over these layers. The spatial distribution shows a clear difference between the upper and lower layers. The lower layer is characterized by a localized PV anomaly in the region of the cyclone center, similar to the PV anomaly composite at 700 hPa for extreme cyclones (see again Fig. 5.2a). In contrast, the average upper-layer anomaly has a broader maximum southwest of the center and a cyclonic wave-breaking structure, reminiscent of the extreme cyclone anomaly at 250 hPa (Fig. 5.2c). Thus, the chosen separation level at 600 hPa appears to work well in separating these different structures (for more details, see Supplementary Fig. C.1). Figure 5.3b,d also

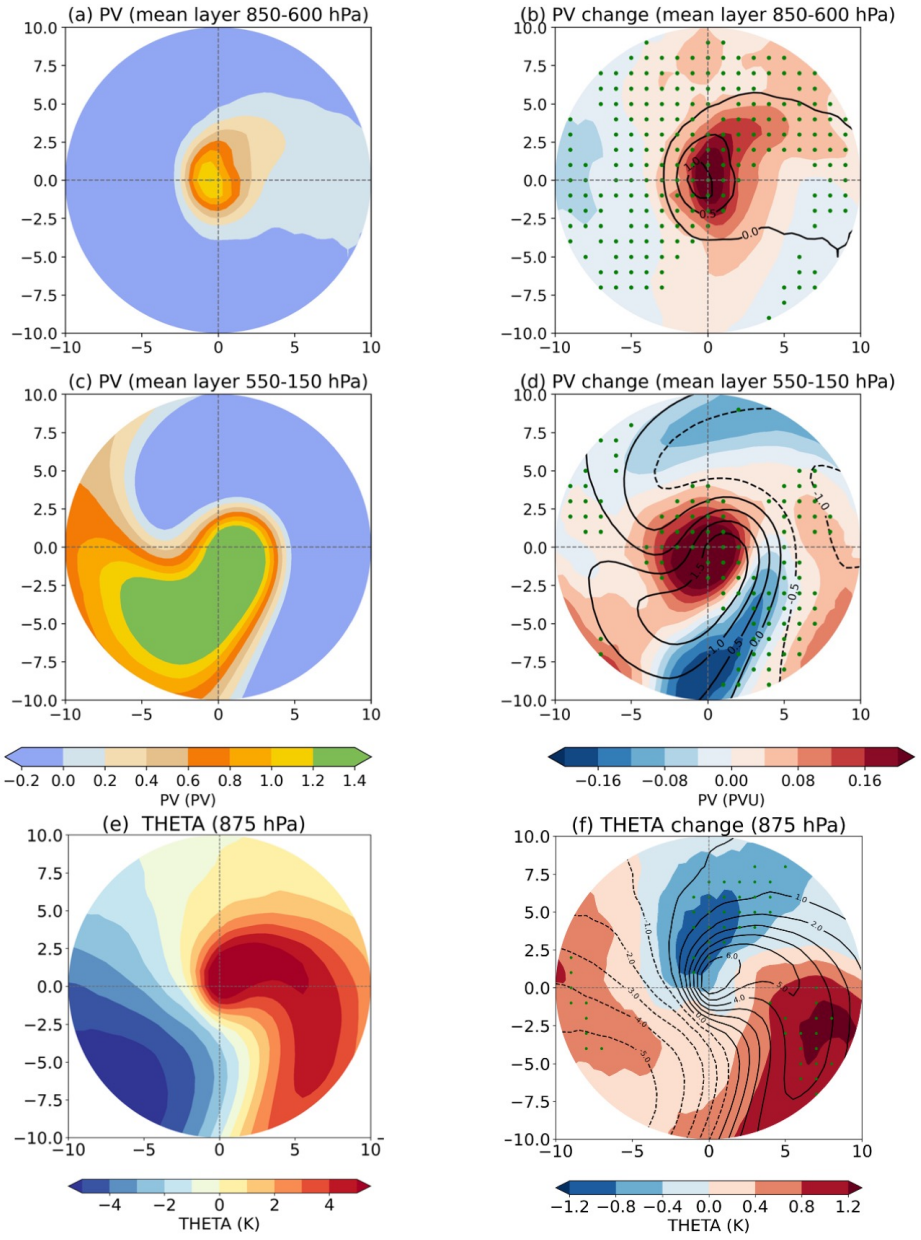

Figure 5.3: Present-day composites for extreme cyclones of PV averaged over (a) the lower troposphere (850-600 hPa), (c) the upper troposphere (550-150 hPa) and (e) potential temperature at 875 hPa (lower boundary) for winter in the North Atlantic region. Future changes of the lower tropospheric PV, upper tropospheric PV and potential temperature are shown in b, d, and f respectively. The present-day mean of each field is overlaid as black contour lines in b, d and f. The composites are shown at the time of maximum intensity (time=0).

shows the future changes of the layer-mean PV anomaly composites. These projected changes are again consistent with our previous findings for specific levels (see Fig. 5.2). The lower-tropospheric anomaly increases mostly near the cyclone center and in the region of the fronts.

In the upper layer, there is a reduction of PV to the south of the cyclone center and a PV increase near the center. Figure 5.3e shows the temperature anomalies at the lower boundary in present-day climate. A predominant positive anomaly is found downstream and a negative anomaly upstream of the cyclone center. Future changes (Fig. 5.3f) are characterized by a temperature anomaly reduction to the north of the cyclone center and two regions of increased temperature, to the west and southeast of the cyclone center. The latter (the most significant increase) covers most of the warm sector. Figure 5.2b shows a southward wind response to the north of the cyclone center as the climate warms and stronger south-westerlies in the warm sector. The temperature anomalies in Fig. 5.3f can thus be related to amplified cold air advection north and amplified warm air advection southeast of the cyclone center.

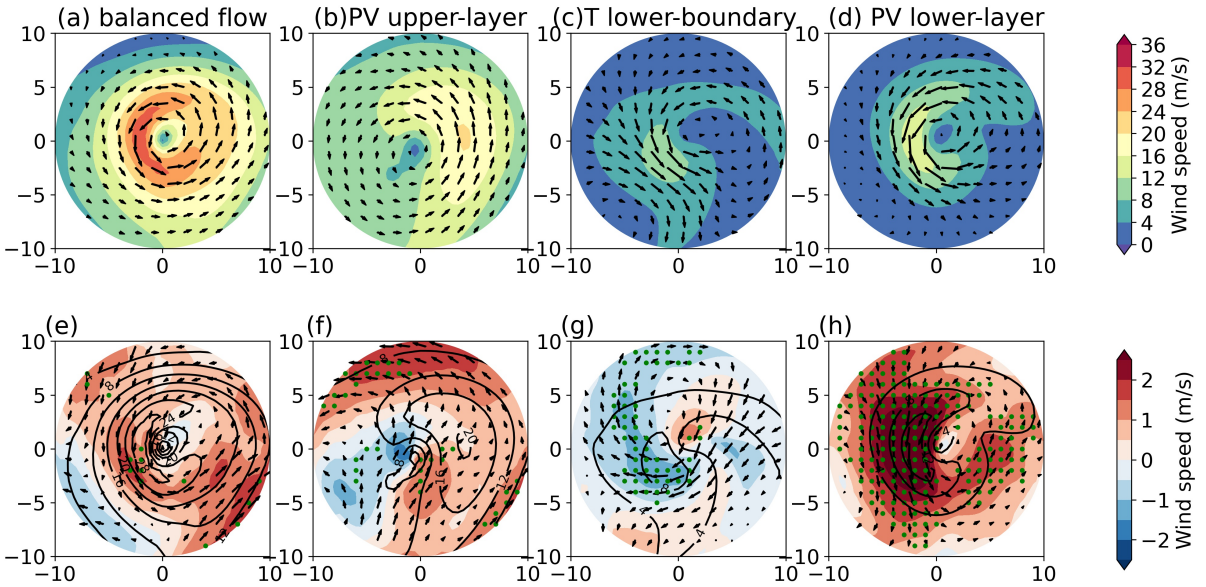

Figure 5.4: PPVI decomposition of the wind composites at 850 hPa in present-day climate (upper row) and their future change (lower row). The total balanced wind composite obtained from the full PV inversion is shown in figures a) and e). The other figures show the wind composites obtained from inverting (b, f) the upper-layer PV anomalies, (c, g) temperature anomalies at the lower boundary, and (d, h) the lower-layer PV anomalies.

Figure 5.4 shows the results of the PPVI for wind speed composites at 850 hPa in present-day climate (upper row) and their projected future change (lower row). The balanced wind composite (Fig. 5.4a) is obtained from inverting the complete PV distribution in the specified domain (see again section 5.1 for more details). It is broadly similar to the full wind composite (present-day composites for extremes, Supplementary Fig. C.2a), the wind speed increases southward and there is a band of strong winds upstream. Nevertheless, the balanced wind speed has a smaller magnitude over the cyclones' warm sector. This indicates that the high winds in this region, which are partly associated with the low-level jet ahead of the cold front, have an essential non-balanced component (divergent component).

Also, projected future changes in the balanced wind (Fig. 5.4e) reproduce changes in the

full wind (Fig. 5.2b) fairly well. In particular, they also show increased wind velocities and an extended wind footprint in the warm sector. PPVI allows for a decomposition of the balanced flow and its changes into contributions from different anomalies, here the upper- and lower-layer PV anomalies, temperature anomalies at the lower boundary as well as the background PV field. For the 850 hPa winds, the background only has a small contribution (see Supplementary Fig. C.3).

Supplementary Fig. C.5, a comparison between the balanced flow and the sum of the total contributions, demonstrates the consistency of this decomposition and shows that both the present-day balanced flow and its projected change are similar to the sum of the individual contributions. Differences between the balanced flow and the sum of all wind components arise due to (i) the imperfect knowledge of boundary conditions, (ii) non-linearities associated with the separation, especially the separation of low-level temperature anomalies and low-level PV anomalies, and (iii) numerical inaccuracies, mostly in calculating the Neumann boundary condition at 125 hPa, where the vertical θ gradient is very large.

The decomposition of the present-day wind composite (Fig. 5.4a-d) indicates that all three anomalies contribute to the cyclonic circulation. The weakest contribution comes from the temperature anomaly, whose center of circulation is also shifted northwestward compared to the cyclone center. The upper-layer PV anomaly has overall the largest contribution, in particular for the poleward flow downstream of the cyclone center, where the horizontal PV gradients in the upper layer are also the largest (cf. Fig. 5.3c). Low-layer PV contributes most substantially to the equatorward flow upstream of the center, again in the region of largest low-layer PV gradients. The critical role of upper-layer PV for the flow at 850 hPa seen in figure 5.4 is generally consistent with our conceptual understanding of cyclone intensification (Hoskins et al., 1985) and with previous PPVI results (Seiler, 2019).

The future change of PPVI decomposition of the wind flow at 850 hPa is discussed now. The largest contribution to the future changes in balanced flow at 850 hPa (Fig. 5.4e) is associated with low-layer PV changes (Fig. 5.4h). The increase in low-layer PV at the cyclone center (cf. Fig. 5.3b), which is mainly due to enhanced latent heating (see again section 4.3), is linked to amplified cyclonic circulation all around the cyclone center, but in particular to its west, where the already strong PV gradients are further enhanced. However, this amplification of the equatorward flow upstream is partly compensated by a reduced equatorward component (Fig. 5.4f) associated with a reduction in the upper-layer PV gradient due to a PV increase to the northwest of the present-day maximum (Fig. 5.3d). In contrast, in the warm sector southeast of the cyclone center, both changes in lower- and upper-layer PV are associated with an enhanced south-westerly flow and thus add up to produce higher wind velocities and an enlarged wind footprint (see again Fig. 5.4e). This wind speed increase in the warm sector is slightly reduced by changes in the temperature anomaly at the lower boundary that are linked to an anomalous anti-cyclonic circulation centered northwest to the cyclone center (Fig. 5.4g). The anti-cyclonic circulation is located over a cold anomaly (Fig. 5.3f). All together, these results show that the

projected enhancement of the wind footprint in the warm sector cannot be attributed to a single mechanism alone, but results from a constructive superposition of wind changes linked to upper- and lower-tropospheric PV anomalies.

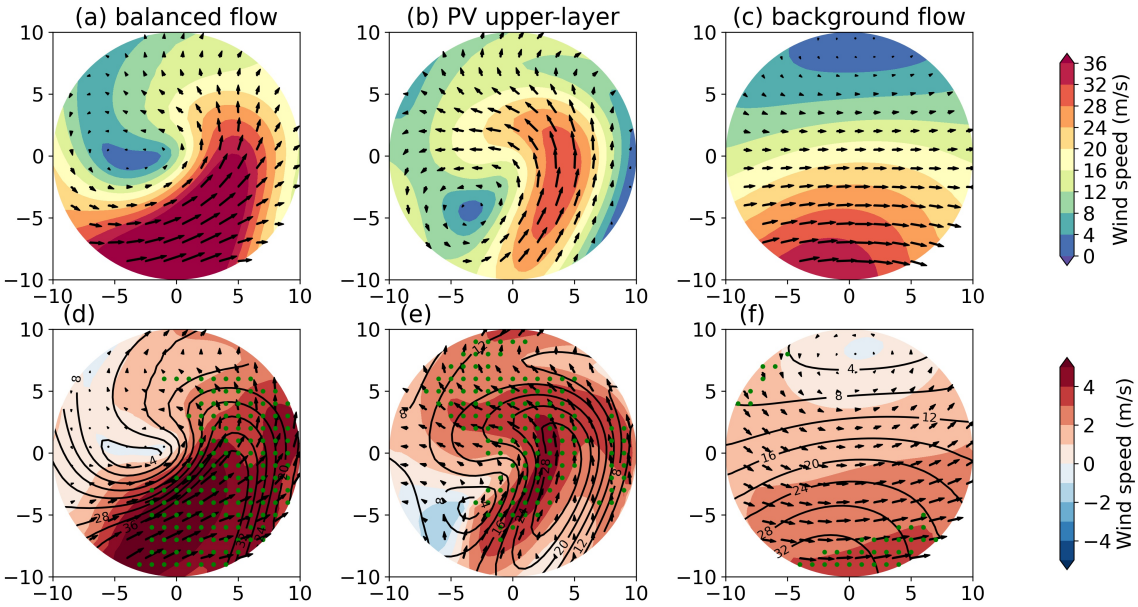

Figure 5.5: PPVI decomposition of the wind composites at 250 hPa in present-day climate (upper row) and their future change (lower row). The total balanced wind composite obtained from the full PV inversion is shown in figures a and d. The other figures show the wind composites obtained from inverting (b, e) the upper-layer PV anomalies and (c, f) the background PV.

Also, for wind speed in the upper troposphere, at 250 hPa (Fig. 5.5), the balanced flow from the PV inversion reproduces the present-day wind composite (cf. Supplementary Fig. 3b) and its projected future change (cf. Fig. 5.2d) qualitatively. However, the present-day wind velocities are underestimated (Fig. 5.5a), and the small projected wind speed reduction northwest of the cyclone center (which is not consistent across ensemble members) is not captured (Fig. 5.5d). As for the low-level wind, the PPVI yields a consistent decomposition of this balanced flow and its future change (Supplementary Fig. C.6). Nevertheless, the contributions of low-layer PV and temperature anomalies at the lower boundary are small (see Supplementary Fig. C.4), such that only the contribution of upper-layer PV and the background flow are shown in figure 5.5.

The present-day wind composite at 250 hPa (Fig. 5.5a) is a superposition of westerly background flow with a wind speed maximum at the southern edge of the domain (Fig. 5.5c) and a component linked to the upper-layer PV anomaly (Fig. 5.5b), which is mostly poleward to the east and westward to the west of the cyclone center.

The future wind speed increase at upper levels, which is mostly found to the south and east of the cyclone center (Fig. 5.5d), results from a combination of the two mentioned

components. First, an amplified westerly background flow (Fig. 5.5f), consistent with previous studies of future changes in the upper-level jet (Grise and Polvani, 2014, Shaw et al., 2016). Second, the larger wind velocities linked to upper-layer PV changes (Fig. 5.5e). The latter is most prominent in a region of enhanced PV gradients associated with the dipole pattern of projected PV changes (see again Fig. 5.3d) southeast as well as north of the cyclone center. Similar patterns of upper-level wind speed changes in midlatitude cyclones have been found by Tamarin-Brodsky and Kaspi (2017). The enhanced poleward flow is thought to contribute to the increased poleward propagation of cyclones in a warmer climate (Tamarin-Brodsky and Kaspi, 2017) and, as discussed in section 4.3, can feedback on the PV anomaly pattern by transporting low-PV airmasses from lower latitudes towards the cyclone center.

5.4 Discussion

In order to better understand the dynamical mechanisms behind these wind speed changes, a PV anomaly and inversion analysis have been conducted. PV inversion has been used previously to study future changes in cyclone propagation (Tamarin-Brodsky and Kaspi, 2017, Tamarin and Kaspi, 2017), but here, it has been used for the first time for the investigation of future changes in the near-surface wind patterns associated with midlatitude cyclones. In agreement with many previous studies (Pfahl et al., 2015, Marciano et al., 2015, Michaelis et al., 2017, Zhang and Colle, 2018, Sinclair et al., 2020) we find an increase in lower-tropospheric PV near the cyclone center and fronts that is most likely due to increased latent heating in a warmer and thus more humid climate (Büeler and Pfahl, 2019).

According to our PPVI analysis, this amplified low-level PV is associated with enhanced cyclonic wind velocities around the cyclone center, indicating that the increased latent heating contributes to the broadening of the wind footprint in the warm sector. However, it is not the sole cause of this broadening, as also PV changes in the upper troposphere go along with an increase of south-westerly winds in this region. More specifically, a dipole change in upper-tropospheric PV with a projected PV increase near the cyclone center and a decrease to the south and southwest are associated with enhanced upper-level PV gradients in the region ahead of the cold front and thus increased poleward flow throughout the troposphere. In contrast to the warm region southeast of the cyclone center, where wind changes associated with upper- and lower-layer PV changes superimpose in a constructive way, these wind changes partly compensate each other upstream of the cyclone center, where net wind speed changes are thus smaller. Note that the projected wind increase in the warm sector is robust across the different cyclone intensity classes and ensemble members analyzed here and is also seen in the balanced wind response of the PV inversion. However, the PPVI does not exactly reproduce the full wind changes in a quantitative way, and the corresponding results should thus be interpreted with care.

Our results have been presented on specific vertical levels, but are generally robust with

respect to small shifts of these levels (see, for instance, Figs. 5.2 and 5.3). Finally, as discussed in section 5.3, the PV inversion results can be affected by errors due to imperfect knowledge of boundary conditions, non-linearities and numerical inaccuracies. Especially the separation between low-level PV anomalies and lower boundary θ-anomalies is affected by such errors, since the far-field impact of the low-level PV anomalies onto potential temperature below is not known. Nevertheless, we have shown that the associated residuum of the decomposition is relatively small and that the inversion method is able to reproduce the main features of the projected wind changes. In the next chapter, a Lagrangian airstream analysis will be used to complement and expand these dynamical insights.

6 A Lagrangian analysis of extratropical cyclones changes in a warming climate

In chapter 5, we found significant changes in PV anomalies in a future climate that have been related to changes in strong near-surface winds. However, the source of these PV anomalies is still unclear, especially at upper levels. Thus, a Lagrangian perspective is adopted in this chapter with backward trajectories to link PV anomaly changes to advective and diabatic processes. Moreover, the role of specific airstreams such as the WCB in the PV generation/destruction are examined.

6.1 Data and methods

Trajectory calculation

The calculation of the trajectories is based on the 1% strongest cyclones in 10 ensemble members of CESM-LE during the extended winter season and the Lagrangian Analysis Tool (LAGRANTO; Wernli and Davies, 1997, Sprenger and Wernli, 2015). LAGRANTO applies a kinematic technique to compute air parcel trajectories using the three-dimensional wind field. 7-day backward trajectories are started from a horizontal equidistant grid ($\Delta x = 200$ km) centered on the cyclone center (SLP minimum) covering the storm area with a fixed radius of 1500 km at the time of maximum intensity of each selected extreme cyclone (Fig. 6.1a).

The trajectories are initialized at 8 different vertical levels: 850., 800., 700., 600., 500., 400., 300., 250. hPa (Fig. 6.1b). Along with these trajectories, different variables are traced, together with the trajectory position (longitude, latitude) and pressure. These physical parameters include specific humidity q, potential temperature θ, and potential vorticity PV.

Composites of Lagrangian air mass properties are computed as outlined in the following. At a given pressure level, the change in magnitude of any variable at two different time steps is calculated for each grid point and each selected cyclone (Fig. 6.2). Then, a radial grid centered on the cyclone center is created to interpolate the change in magnitude using the method described in chapter 4. Finally, these Lagrangian changes are averaged over all extreme cyclones to construct the Lagrangian composites at specific pressure levels.

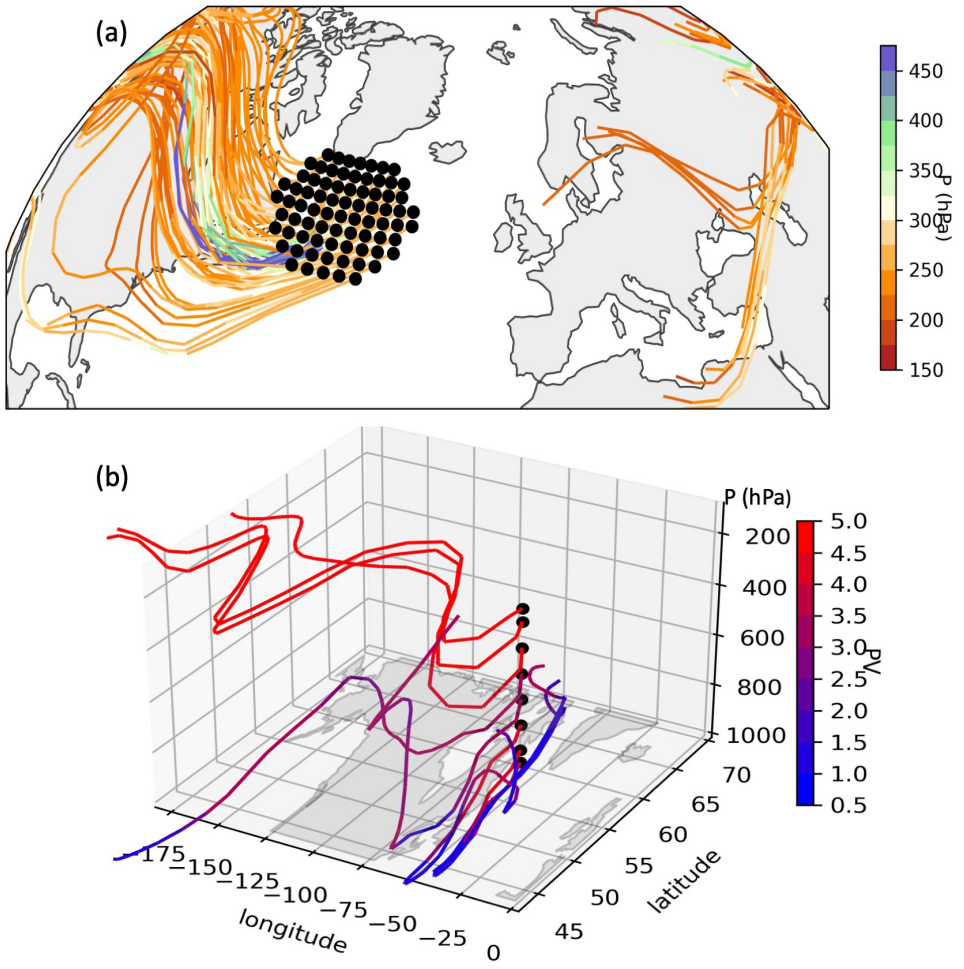

Figure 6.1: (a) Pressure changes (color) along trajectories ending at 250 hPa and (b) PV along trajectories initialized at all levels at the cyclone center of one storm during the 7 days before the time of maximum intensity.

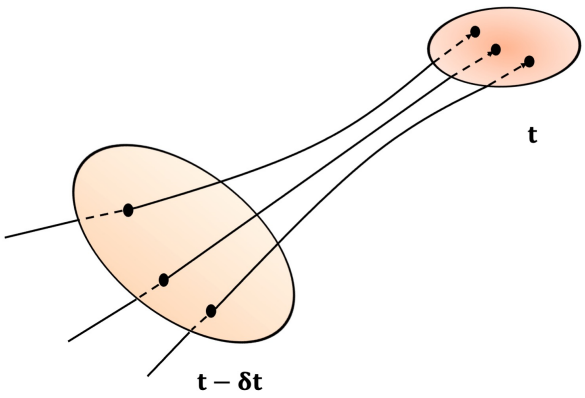

Figure 6.2: Computation of changes in air mass properties for the Lagrangian composites.

6.2 Time series of parameters along trajectories

In this section, we analyze the temporal evolution of different key parameters along the backward trajectories, which provides insights into the time at which the parameters experience a significant change, which eventually determines the cyclone intensity and structure. The change of PV and θ between two timesteps along the trajectories can be associated with diabatic processes due to their conservative properties for adiabatic and frictionless motion (Steinfeld and Pfahl, 2019, Steinfeld et al., 2020). A comparison between the temporal evolution of the present-day and future trajectories may provide insights into the influence of diabatic and advective processes that shape the structure and intensity of PV anomalies in the future climate.

As the first step, we evaluate various parameters averaged over all trajectories ending in the cyclone area (in a radius of 10^o around the SLP minimum). The evolution of these parameters along backward trajectories initialized at the time of maximum intensity is examined for two specific pressure levels: 700 hPa and 250 hPa. In the following, the temporal evolution of a) pressure, latitude, longitude, b) specific humidity, c) θ and d) PV along these trajectories is analyzed.

a) Pressure, latitude, longitude

Figs. 6.3a,b show the temporal evolution of pressure along backward trajectories. Both trajectories ending at 700 and 250 hPa experience an ascent in the previous 24-h to the maximum intensity. At low levels, the ascent is about 30 hPa, while at upper levels, it is larger, around 50 hPa. This ascent could be associated with airstreams activity, for example, the WCB (Binder et al., 2016, Madonna et al., 2014). Note that we have averaged the trajectories in the cyclone region without distinguishing between the different airstream types. Thus, a strong ascend similar to the WCB (600 hPa in two days) can not be found here. However, the lagrangian composites presented in the following sections will allow us to better distinguish the different airstreams.

In general, the trajectories experience an equatorward displacement before the ascent and a poleward movement during the ascent phase (Figs. 6.3c,d). The temporal evolution of longitude (Figs. 6.3e,f) shows that the trajectories move eastward. Moreover, trajectories ending at upper levels travel larger distances, which is due to the typically larger wind velocities at upper levels.

In the future climate, we observe that the trajectories ending at 700 hPa behave similarly as for the present-day. For instance, the main ascent starts in the 24 hours prior to maximum intensity. A qualitative change during this period of ascent (t=-24) is not evident. However, the trajectories before this final 24 h period are originated from higher levels compared to present-day. Before 7 days, most of them are located close to the 650 hPa level. The spread is similar in both periods, decreasing 2 days before the cyclones' maximum intensity.

At the end of the century, trajectories are projected to follow a similar zonal and meridional displacement as in present-day.

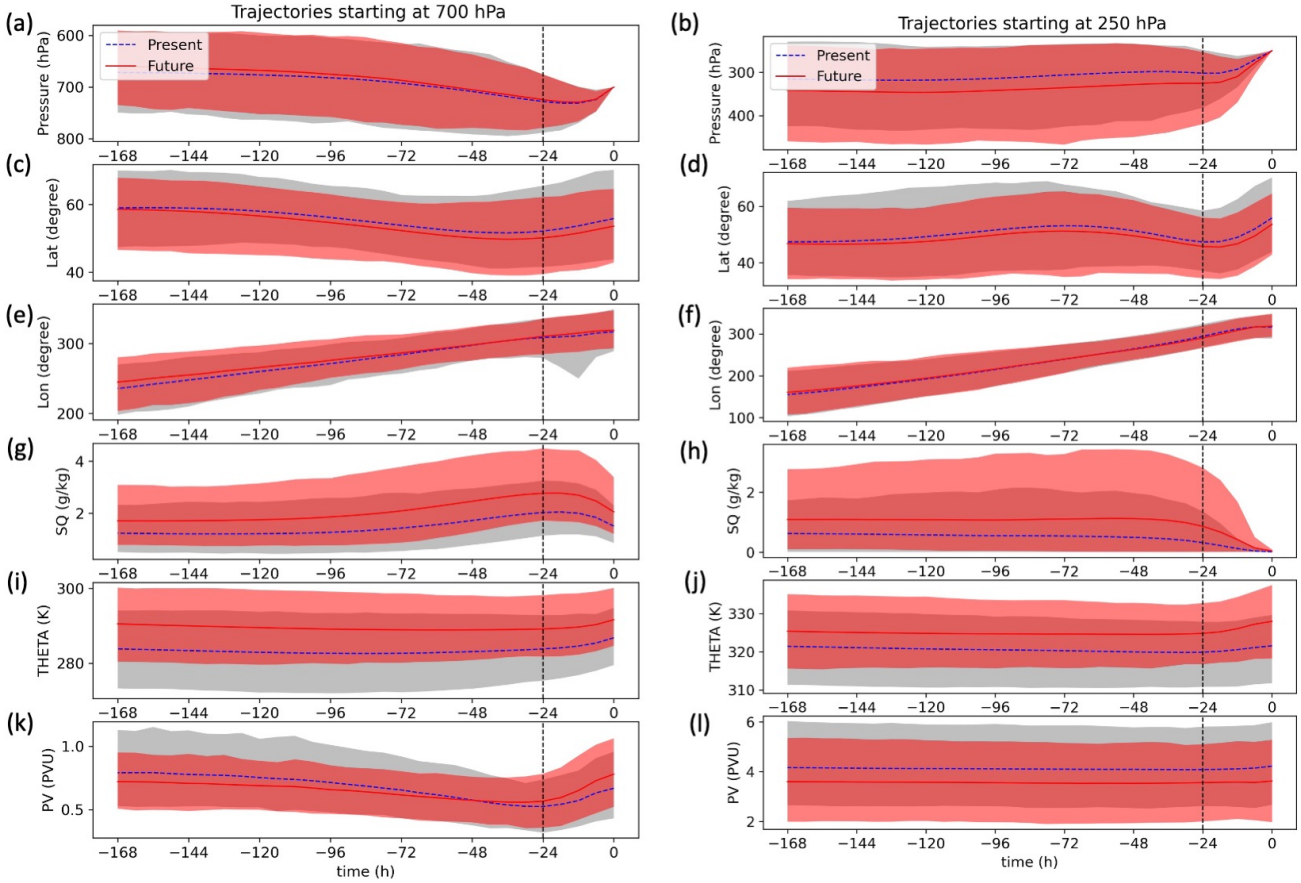

Figure 6.3: Temporal evolution of pressure, latitude, longitude, specific humidity, potential temperature and PV averaged over all trajectories initialized within a 10° radius around the cyclone center and all selected cyclones. The average for present-day climate is shown as blue, dashed line, the average over the future time slice as red line. Shading shows the 5 and 95 percentile.

b) Specific humidity

Fig. 6.3g,h shows the temporal evolution of specific humidity along the backward trajectories. Trajectories reaching the lower levels experience different moisture changes compared to the trajectories reaching the upper levels. During the 6-day pre-ascent phase, trajectories reaching the 700 hPa level typically gain moisture, on average, from 1.5 to more than 2 g Kg^{-1}. During the ascent phase, water vapor condenses, and the specific humidity decreases to 1.5 g Kg^{-1}. In contrast, trajectories reaching upper levels experience a constant decrease of moisture with values close to 0 g Kg^{-1} at 250 hPa.

In the future climate, the moisture content increases for both trajectories ending at upper and lower levels. The moisture increase for trajectories ending at 700 hPa is constant over time (0.5 gKg^{-1}). However, trajectories ending at 250 hPa converge towards 0 gKg^{-1} at the time of maximum intensity, similar to the present-day.

c) Potential temperature

Fig. 6.3i shows an increase of the airstream's potential temperature during the ascent period (t=-24 to t=0) for trajectories reaching the 700 hPa level. The increase can be linked to the latent heat release associated with the phase changes of moisture during the ascent (condensation, vapor deposition, freezing). This effect is responsible for the increase of θ along the trajectories reaching 250 hPa (Fig. 6.3f). The trajectories reach the level of 700 hPa with a potential temperature of 285 K in the mean, while the trajectories reach the level of 250 hPa with a potential temperature of 321 K. However, there is a large spread of around 20 K, which makes it difficult to detect changes.

In the future, the potential temperature along backward trajectories generally increases in the 7 days before the maximum cyclone intensity. An increase of 5 K is projected for both trajectories ending at 700 hPa and at 250 hPa. Note that this increase corresponds with the global mean warming of 5 K. The future evolution of the potential temperature during ascent will be examined in detail with the composites in the next section.

d) Potential vorticity

PV is a conservative quantity along adiabatic flows, and its value in an air parcel can only be modified by diabatic or frictional processes (Hoskins et al., 1985). Figs. 6.3k,l show the temporal evolution of PV along the backward trajectories. We observe a different behavior between trajectories ending at 700 hPa and 250 hPa. For instance, trajectories ending at 700 hPa experience a clear increase 24 h before the cyclones' maximum intensity. A steep PV increase at low levels before the maximum cyclone intensity can be produced by intense WCB cloud-diabatic processes (Binder et al., 2016, Madonna et al., 2014). At 250 hPa, the trajectories barely experience changes. Most likely, these small changes in the mean PV are related to opposing PV changes along individual trajectories, with some of them experiencing PV destruction due to their location above the region of maximum diabatic heating.

The future temporal evolution of PV (red color in Fig. 6.3k,l) along trajectories ending at 700 hPa is projected to be characterized by a more pronounced increase than for present-day. This PV increase is consistent with an increase in precipitation found in section 4.2. Note that such increases in θ evolution are not evident. A more constant spread is observed in the future climate. On the contrary, the trajectories ending at 250 hPa are projected to have an almost constant PV value, similar to the present-day trajectories. Nevertheless, the PV of the future trajectories will remain lower than for

present-day during the whole period of 7-days. This can be explained by a decrease in the climatological PV at upper levels (Fig. 6.4). The impact of this effect on the upper PV anomalies differs depending on the cyclone region. A more detailed description of the PV evolution at specific locations will be analyzed in the following.

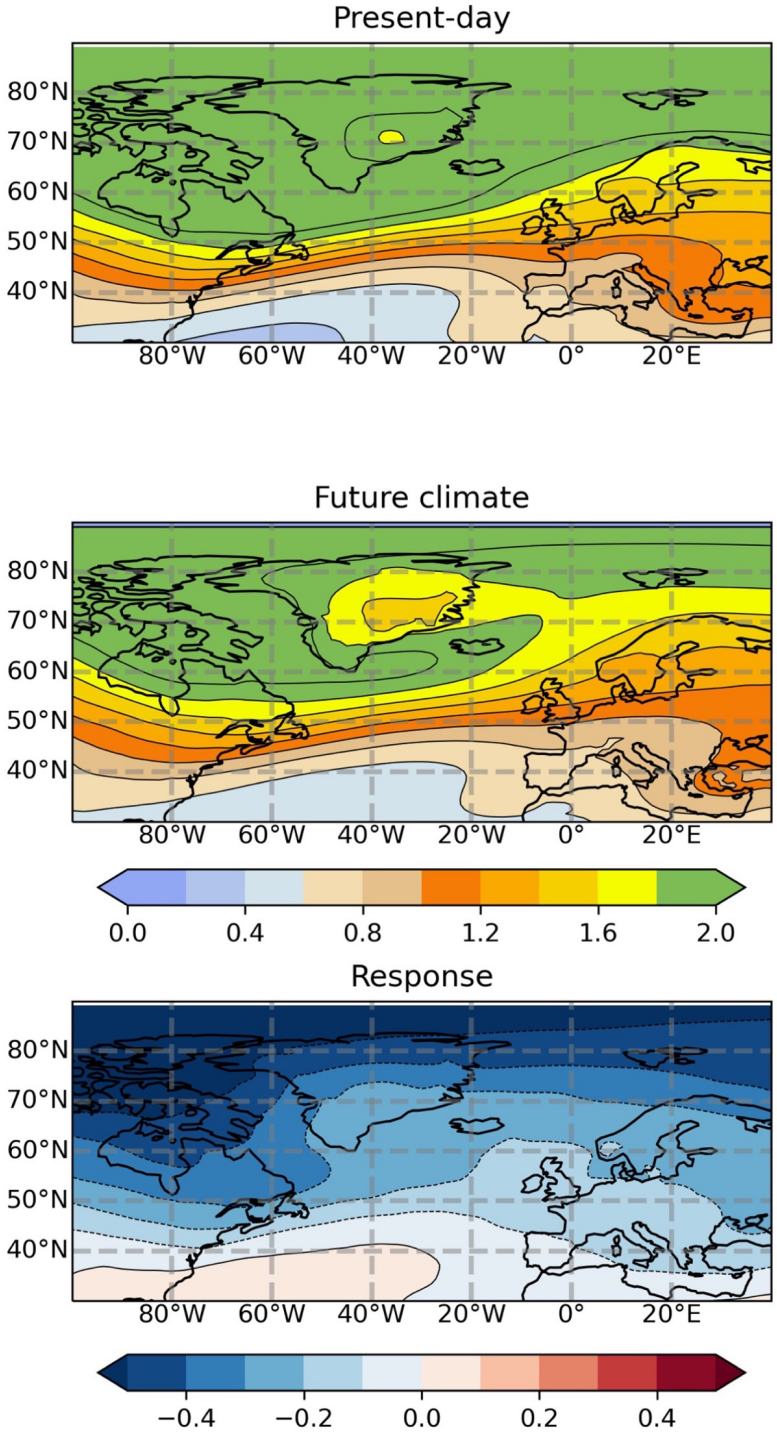

Figure 6.4: PV climatology for the extended winter in the North Atlantic region in the present-day, future climate and their difference (response to climate warming).

Time series of parameters along backward trajectories initialized at specific locations

To get an impression of the evolution of trajectories ending over the PV anomalies associated with the strong winds discussed in chapter 5, we average the trajectories ending at the cyclone center (positive PV anomaly response at upper levels, marked as a black star in Fig. 5.2c). The second specific location analyzed in the following is to the north of the cyclone center (positive PV anomaly response at upper levels, marked as a green star in Fig. 5.2c). Finally, we analyze the trajectories ending to the south of the cyclone center (negative PV anomaly changes at upper levels, marked as a yellow star in Fig. 5.2c).

Fig. 6.5l shows the temporal evolution of PV along backward trajectories ending at the cyclone center at 250 hPa. We identify an increase in PV 24 h before the maximum intensity. Future PV values are lower than for present-day 7 days before the maximum intensity and for almost the entire trajectory period, but converge towards the present-day at the end of the ascent phase, going along with a stronger PV increase in the last 24 hours. A reduction in PV of the trajectories for the whole period is expected in the future climate. Note that there is no difference in PV at the final time step between present-day and future climate, but the composite at upper levels (Fig. 5.2c) shows an increase in the PV anomaly. This difference can be explained by the reduction of the climatological PV (Fig. 6.4) that is used for the calculation of anomalies.

Fig. 6.5k shows the temporal evolution of PV along the backward trajectories ending at the cyclone center at 700 hPa, for which an increased PV in the future climate is evident. Accordingly, Fig. 6.5a shows a strong ascent ($\sim$ 300 hPa in 24 h) for both present-day and future periods, with a slight increase in the mean ascent projected in future climate. Thus, we can assume that the PV is diabatically produced.

The stronger diabatic PV production in the warmer future climate is consistent with higher moisture content and a more pronounced decrease in specific humidity during the final 24 h (6.5g). However, stronger diabatic heating is not directly evident from the evolution of potential temperature, for which the absolute change in the last 24 hours is comparable for present-day and future climate.

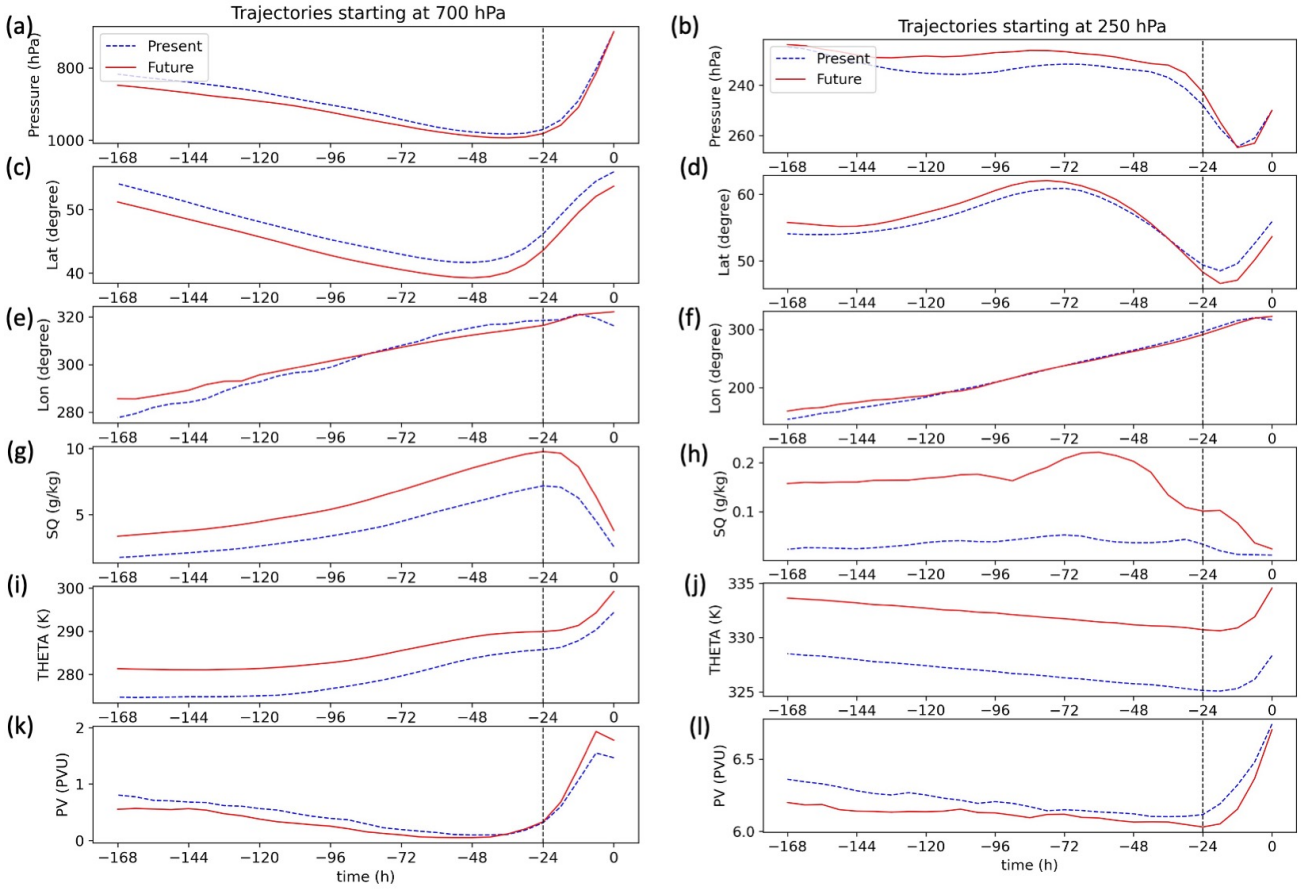

Figure 6.5: Temporal evolution of pressure, latitude, longitude, specific humidity, potential temperature and PV along trajectories ending at the cyclone center.

Air parcels ending at 250 hPa to the north of the cyclone center (positive PV anomaly response at upper levels) have a different path (Fig. 6.6) in comparison with the trajectories ending at the cyclone center. Here, trajectories ascend 24 hours before the maximum intensity from middle tropospheric levels. Since the middle levels will be a region of strong heat release in a warming climate, θ along the trajectories increases faster in the future than in the present-day climate. The PV along these trajectories experience an increase and decrease pattern prior reaching the level of 250 hPa. This increase and decrease pattern and the relatively small overall changes could be related to both diabatic PV generation, but also destruction above the level of maximum heating, which partially compensate each other when averaging over many trajectories.

In addition, the trajectories experiences a strong northward movement (Fig. 6.6d), but not a big change in longitude in the last 24 hours, which means a westward displacement relative to the eastward-moving cyclone center and thus likely corresponds to a cyclonic wrap-up around the cyclone center.

Fig. 6.6 shows that the trajectories ending at 700 hPa move downward and are dominated by diabatic cooling. However, in the future, PV along these trajectories will experience a smaller decrease, probably associated with changes in microphysical processes, for example, an increase in snow melting (Crezee et al., 2017, Attinger et al., 2021).

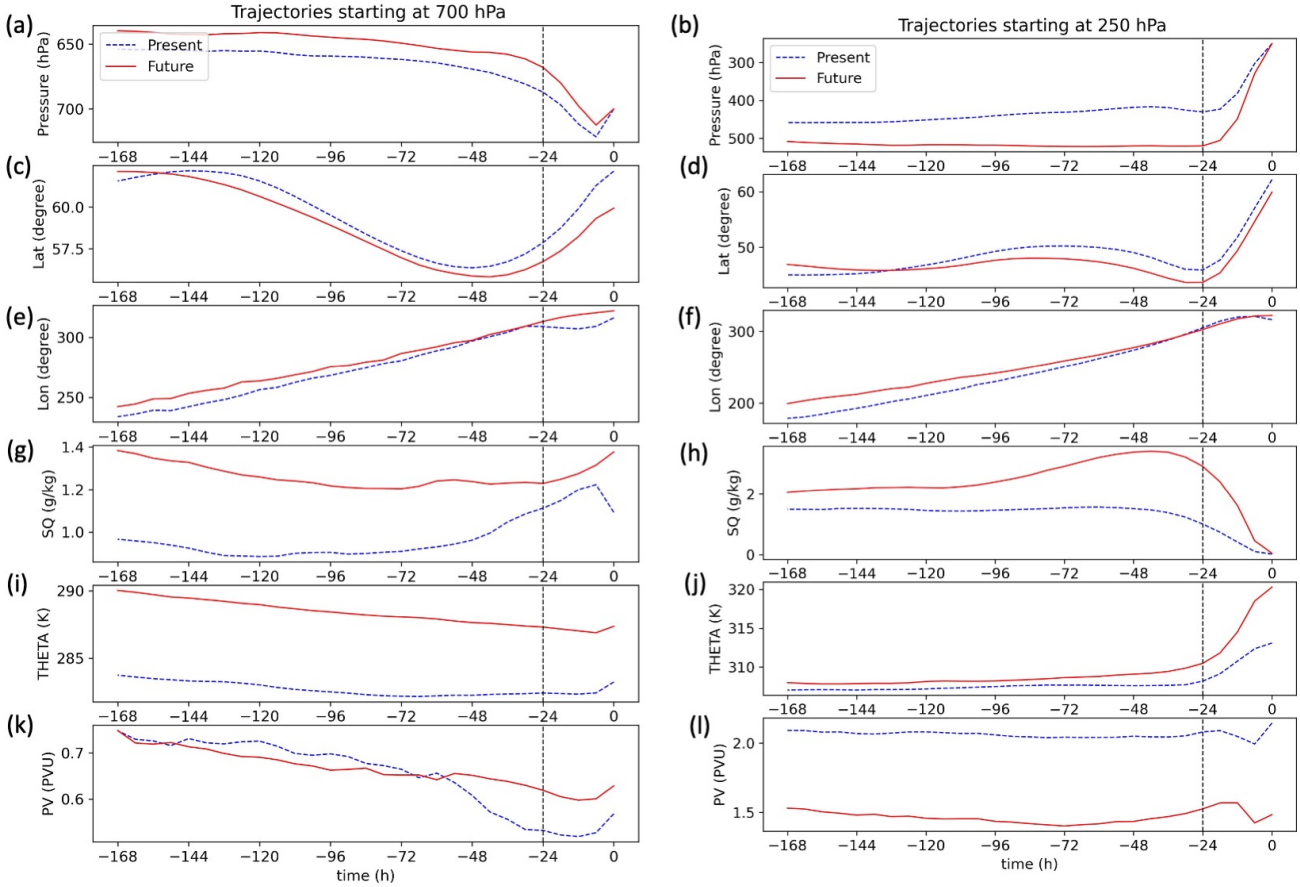

Figure 6.6: Temporal evolution of pressure, latitude, longitude, specific humidity, potential temperature and PV along trajectories ending to the north of the cyclone center.

The temporal evolution of PV along trajectories ending at 250 hPa south of the cyclone center (negative PV anomaly response at upper levels) is shown in Fig. 6.7l. Here, the PV evolution of trajectories remains nearly constant during the 7 days before the cyclones' maximum intensity in present-day, with a slight increase in the 6 h before arrival. Note that the trajectories move downward 6 h prior to the storm's maximum intensity. In the future climate, PV along trajectories ending at 250 hPa is projected to decrease. The PV reduction is probably associated with the reduced PV climatology in the future (see again Fig. 6.4) and the origin of the trajectories. Air parcels originate at lower latitudes and lower levels in the simulated future climate (Fig. 6.7b,d), i.e., in a region with typically smaller PV values. This change, thus, is the main reason for the negative PV anomaly

response to the south of the cyclone at upper levels (Fig. 5.2c).

We can also observe that the trajectories ending at 700 hPa south of the cyclone center tend to descend 48 h prior to the maximum intensity, which is associated with a PV reduction. Changes in potential temperature are relatively small, but dominated by diabatic cooling at least in the period prior to -24 h (Fig. 6.7i). This evolution resembles the dry intrusion air stream (Raveh-Rubin, 2017). However, the PV reduction along trajectories in the future climate will be smaller, resulting in a positive PV anomaly response, in agreement with the PV composite (Fig. 5.2a). Changes in turbulent mixing processes might contribute to a larger PV at lower levels to the south of the storm center (Attinger et al., 2021). A more detailed description of the structure of the PV reduction will be performed in the next sections.

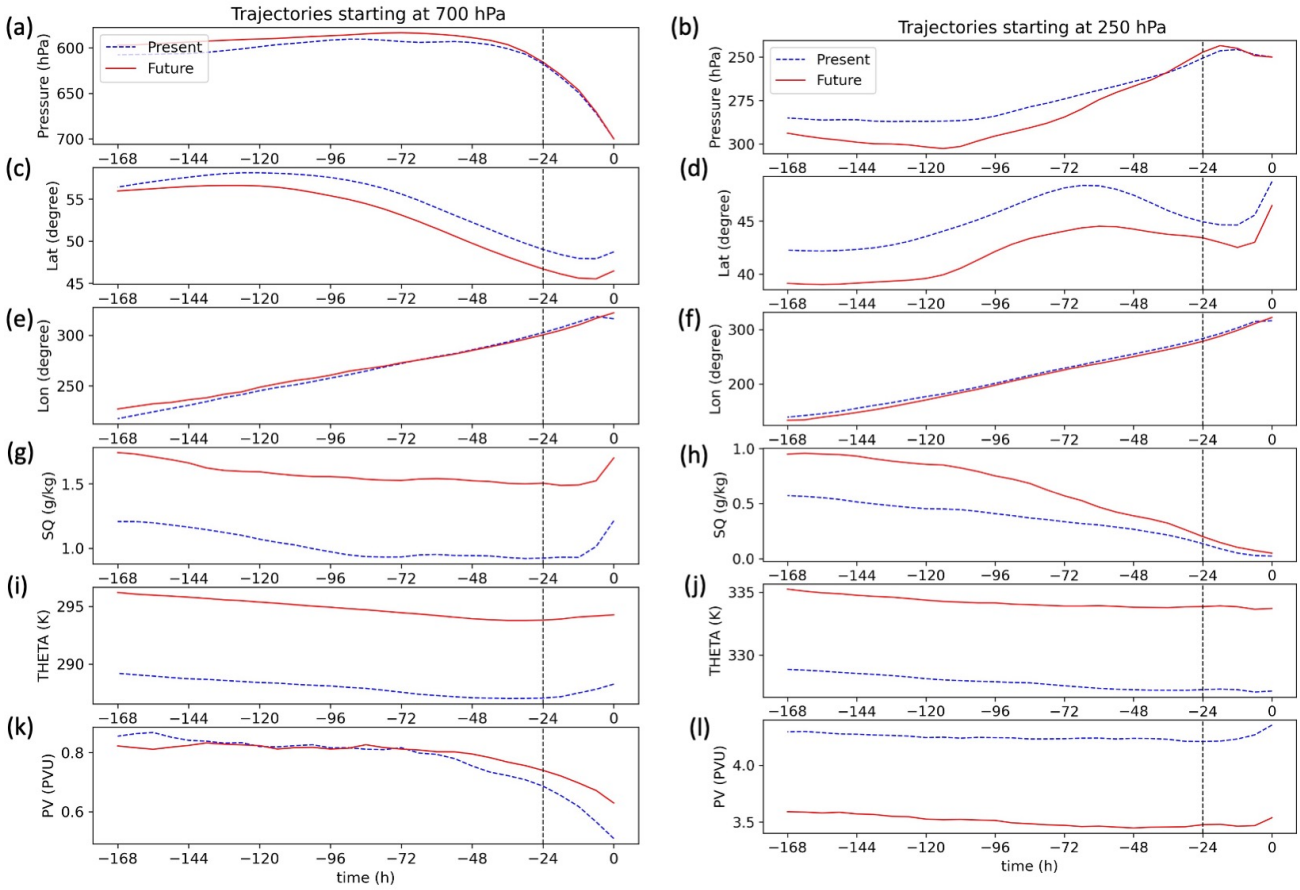

Figure 6.7: Temporal evolution of pressure, latitude, longitude, specific humidity, potential temperature and PV along trajectories ending to the south of the cyclone center.

6.3 Lagrangian composites of extreme cyclones

In the previous section, we have identified that the period of significant changes in the physical parameters is 24 hours before the maximum intensity; during this period, a clear ascent phase and a PV increase are observed at the cyclone center. However, the distribution of the PV may vary in the cyclone area. Therefore, we have constructed Lagrangian composites by subtracting the value of a specific parameter in the air parcel at time t= - 24 h from the value at time cyclone maximum intensity (t=0). In this way, we can investigate the change of the physical parameters during the period of maximum change (see Figs. 6.3, 6.5, 6.6, 6.7) and identify the spatial distribution of the different airstreams. We examine such Lagrangian composites of changes in latitude, longitude, pressure, θ and PV.

Low levels (700 hPa)

a) Latitude, longitude and pressure

Fig. 6.8a shows the composite of latitude change along trajectories ending at 700 hPa during the 24 h before the cyclone maximum intensity. The contours depict the present-day change, and the colors show the future response. Here, positive (negative) values indicate trajectories originating from the south (north). Trajectories from the south dominate the downstream region of the cyclone, with the maximum northward transport over the warm region. Thus, the trajectories ending in the warm region travel long distances from the south. Trajectories from the north are found southwest of the cyclone center with smaller absolute meridional displacements.

Now, we examine the composite of longitude change along trajectories ending at 700 hPa (Fig. 6.8b). Note that positive (negative) values indicate trajectories originating from the west (east). The air parcels have a dominant trajectory from west to east. The trajectories traveling farther from the west are located to the south of the cyclone center. A small region of westward displacement is located northwest of the cyclone center (expected occlusion region), indicative of cyclonic wrap-up of the air around the cyclone center, as also mentioned above. Note that the cyclones generally move eastward; thus, a clear westward displacement is not expected.

In Fig. 6.8c a clear zone of ascent is identified in the warm region and particularly around the cyclone center. A maximum rate of ascent of 250 hPa in 24 h is located at the cyclone center, whereas a wedge-shaped zone of descent is located to the southwest of the cyclone center.

Strong ascent from the south in the warm region can be linked to the WCB activity. As discussed previously, the descent branch from farther west to the south of the cyclone center can be related to the dry intrusion activity.

As the climate warms, the warm region and cyclone center will be dominated by an enhanced ascent and more pronounced northward transport. On the southern flank, the region of descent will slightly increase. On the northwestern flank, a new region of descent emerges. This could be related to the cold conveyor belt or the warm conveyor belt wrapping around the cyclone. Thus, a generally stronger cyclone airstream activity is expected in the future climate.

b) θ

Fig. 6.8d shows the Lagrangian composite of potential temperature at 700 hPa (trajectory changes in 24 h prior to maximum cyclone intensity). In the present-day climate, we observe an increase in potential temperature along trajectories all over the cyclone region. The largest increase in potential temperature is located at the cyclone center. This potential temperature increase matches up with the region of the strongest ascent. Thus, the trajectories heat up as they rise, most likely due to latent heat release during cloud formation.

The future response of the potential temperature change along backward trajectories is shown by the color shading in Fig. in 6.8d. More vigorous heating will cover the cyclone center, while weaker heating will dominate the region to the south and northwest of the cyclone center. This response of diabatic heating coincides again with the change in vertical motion. The regions of enhanced descent will be regions of weaker heating. In contrast, regions of enhanced ascent will be regions of more substantial heating.

c) PV

The Lagrangian change of PV in the 24 h prior to maximum intensity is shown in Fig. 6.8e. PV production is observed in trajectories ending in the warm region with its maximum at the cyclone center. The PV production region coincides with the region of strong ascent (in a come-shape). Therefore, similar to θ, PV along trajectories is increased as the air parcels rise. This process in the warm region, in particular near the cyclones' warm fronts, is likely related to WCB activity.

A small region of PV destruction is found to the south of the cyclone center, which can be linked to the region of descending trajectories associated with the dry intrusion.

In the future climate (Fig. 6.8e), PV along trajectories will increase more substantially in most of the cyclone region (except for the northwest region). The stronger PV production follows a coma-shape over the warm region, with the strongest changes at the cyclone center. An enhanced increase of PV matches up with a more vigorous ascent in the WCB region near the cyclones' warm fronts. We suggest that an enhanced WCB will contribute to PV production by diabatic processes.

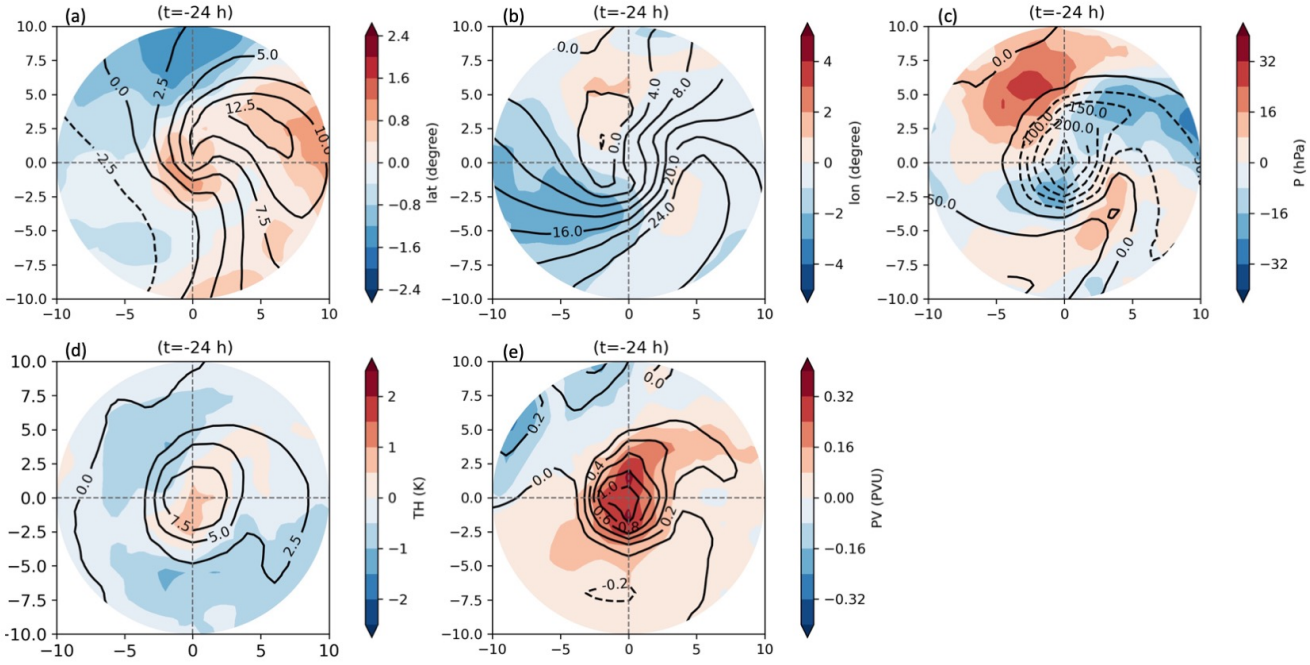

Figure 6.8: Present-day Lagrangian changes in the last 24 hours before arrival in backward trajectories initialized at 700 hPa (contours) and their future response (shaded color) of (a) Latitude, (b) longitude, (c) pressure, (d) potential temperature and (e) PV.

Upper levels (250 hPa)

a) Latitude, longitude and pressure

Fig. 6.9a shows the composite of latitude change along trajectories initialized at 250 hPa during the 24 h before the cyclone maximum intensity. The contours depict the present-day change, and the colors show the future response. Most of the cyclone region is dominated by trajectories coming from the south, with the faster trajectories to the northeast of the cyclone center. A smaller region to the west of the cyclone center has some trajectories coming from the north. Note that at low levels, there is a larger region of trajectories from the north along the same flank of the cyclone.

The composite of longitude change along trajectories ending at 250 hPa is shown in Fig. 6.9b. Trajectories generally move eastwards during the 24-hour period. The most substantial change in longitude is found to the southeast of the cyclone center ($\Delta x \approx 45^o$), near the left exit region of the upper-level jet streak.

Regions of ascent and descent are shown in Fig. 6.9c. Ascending trajectories are located northeast of the cyclone center. Contrary to the low levels, the strongest ascent is located to the north of the cyclone center. The ascending air parcels to the northeast, which also moved poleward in the last 24 h before the time of maximum intensity (see again

Fig. 6.8a), can be related to the WCB outflow. The descent of trajectories located to the southwest of the cyclone center is weaker than the ascent in the eastern part.

In the future climate, the region north of the cyclone center will be affected by enhanced ascent. Also, over this region, the trajectories will experience a stronger poleward displacement while the eastward displacement will become weaker. This is indicative of a more intense WCB outflow, which wraps around the cyclone center.

b) θ

Fig. 6.9d shows the Lagrangian composite of potential temperature at 250 hPa. In the present-day climate (contours), the potential temperature increases along trajectories to the north of the cyclone center and over the low-level warm region. Similar to the Lagrangian composite at 700 hPa, at upper levels, the region of maximum increase of potential temperature matches up with the region of most vigorous ascent. The trajectories experience a slight decrease in potential temperature upstream of the cyclone center. Again, this decrease coincides with descending trajectories. Thus, ascending trajectories experience diabatic heating, most likely due to cloud formation, and descending trajectories experience slight diabatic cooling, probably due to longwave radiation.

The future response of the potential temperature change along trajectories is indicated by the shaded colors Fig. in 6.9d. Here, we identify an intensification of the temperature changes. A more substantial increase in temperature will dominate the trajectories reaching the north of the cyclone center. The stronger warming along these trajectories still matches up with the enhanced ascent. Therefore, the link between heating and ascent will prevail and dominate the cyclone's upper-level dynamics, particularly to the north of the cyclone center. Again, the heated airstreams can be related to a WCB branch wrapping up around the cyclone center.

c) PV

The change in 24 h prior to the maximum intensity of potential vorticity along the trajectories is shown in Fig. 6.9e. In the present-day climate, the most evident PV production along trajectories is located in the cyclone center. This region does not show a strong ascent and the trajectories originate from the west. Note that the cyclone center is where we have identified the maximum positive PV anomaly in the composite analysis in the present-day climate. PV destruction is observed to the northeast of the cyclone center.

In the future climate (Fig. 6.9e), less PV production along trajectories will cover most of the cyclone region (except for the northwest region). The PV reduction will also include the south region of the cyclone, where we have found the most evident negative PV anomaly response in the future climate. However, this Lagrangian PV analysis shows that the region with the largest negative change in PV production along trajectories is located to the northeast of the cyclone center. Note that from the temporal evolution of PV in the south region of the cyclone (see again Fig. 6.7), PV along trajectories is lower

in the future climate than in the present-day during the entire 7 days, which is attributed to a reduced climatological PV. A small region of enhanced PV production is located to the west of the cyclone center.

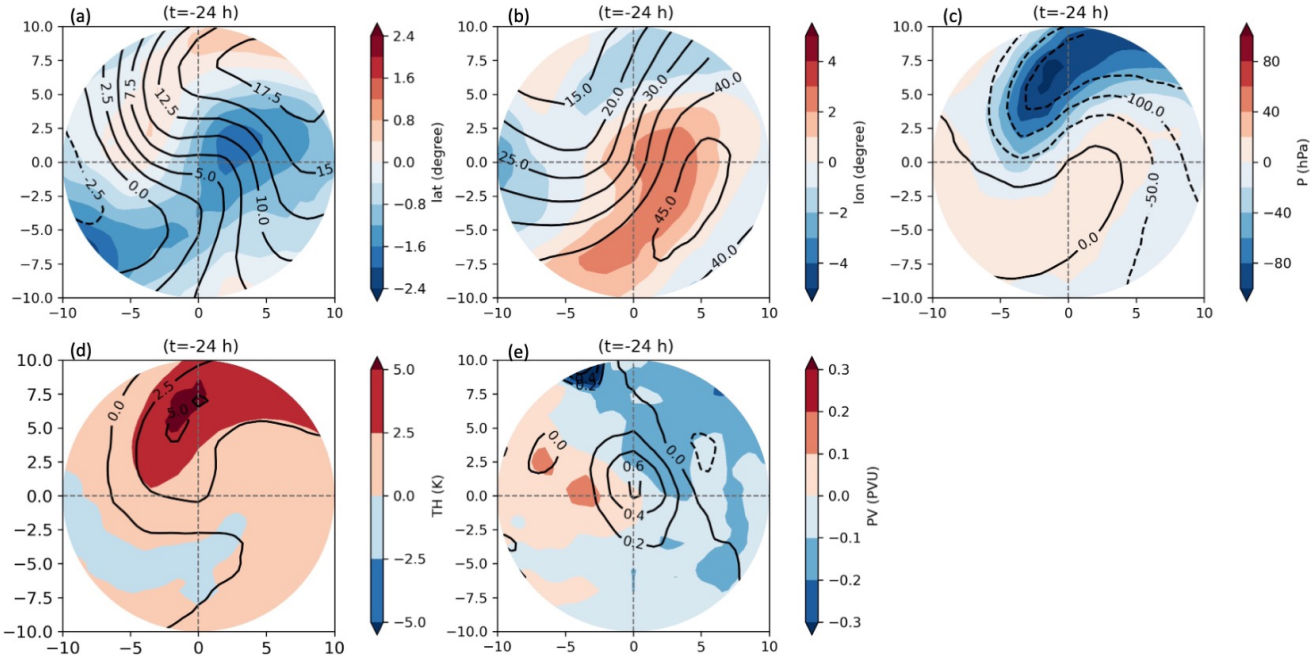

Figure 6.9: Present-day Lagrangian changes in the last 24 hours before arrival in backward trajectories initialized at 250 hPa (contours) and their future response (shaded color) of (a) Latitude, (b) longitude, (c) pressure, (d) potential temperature and (e) PV.

6.4 Lagrangian composite cross sections

The Lagrangian composite analyses point out that specific airstreams shape the cyclone structure in the future climate. A different perspective to analyze the airstream contributions to the PV changes in extratropical cyclones can be obtained from vertical cross sections in different regions. Therefore, we have constructed Lagrangian composites along vertical cross-sections to investigate the role of the dry intrusion and WCB in four different regions: (1) west to east at cyclone center, (2) south to north at cyclone center, (3) south to north at 8 ^{o} longitude (WCB regime), and (4) west to east at -4^o latitude (dry intrusion regime).

We first describe two cross-sections 1 and 2, which are located at the cyclone center. The parameters to examine are pressure and PV.

a) Pressure

The west-east vertical section across the center of the composite cyclone shows the pres-

ence of two zones of strong ascend (Fig. 6.10a).

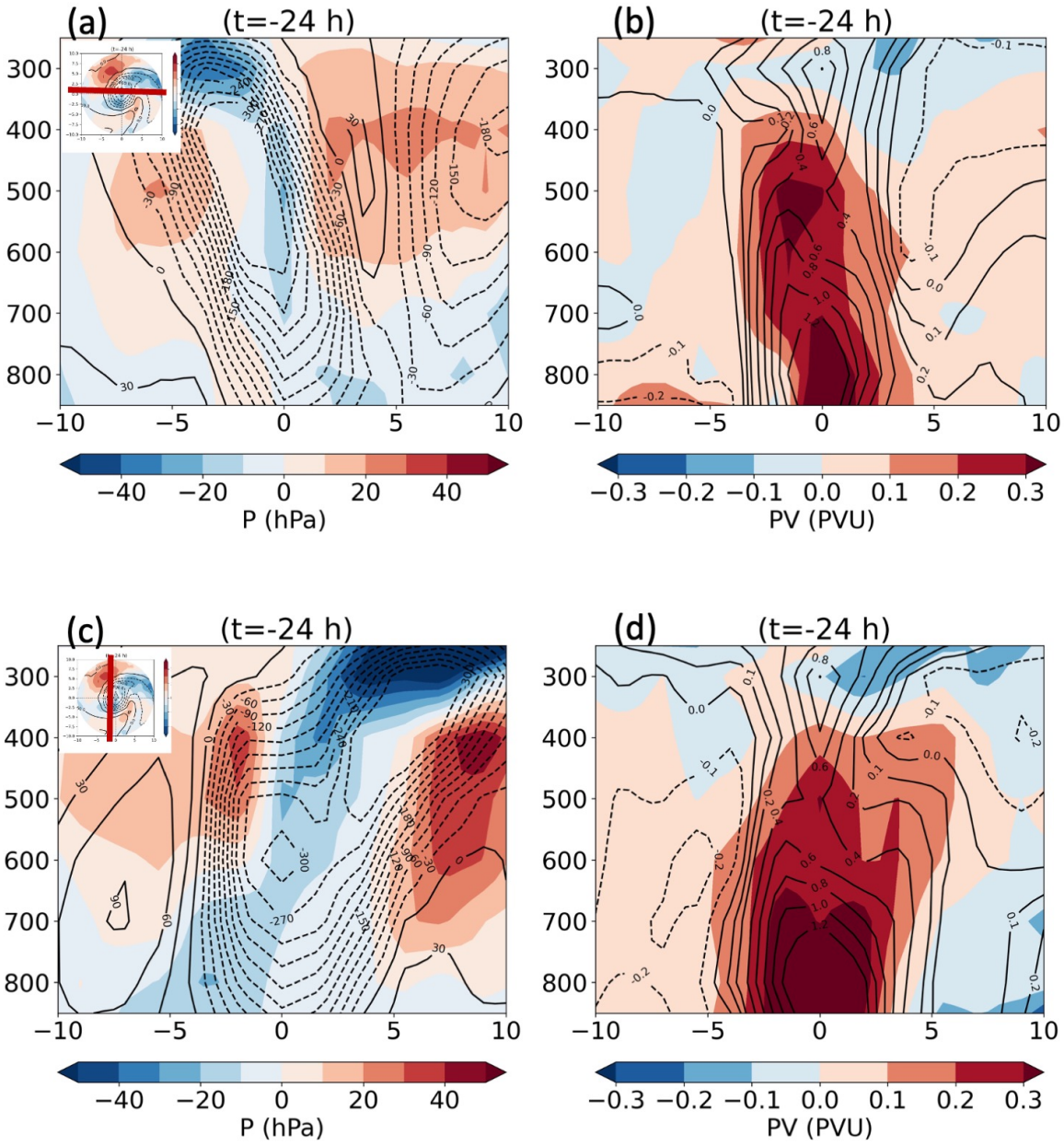

Figure 6.10: (a,b)West-east and (c,d)south-north vertical cross sections through the cyclone center. Shown are changes in time of (c,d) pressure and (b,d) PV along trajectories:[t=0]-[t=-24]. Present-day airstream changes (contours) and their future response (color shading).

The first is located over the cyclone center, with the most vigorous ascent at mid-levels. From the south-north vertical section across the composite cyclone, we identify that the

ascent dominates to the north of the cyclone center (Fig. 6.10c). A second ascending region is observed to the east of the cyclone center, and the strongest ascend occurs at higher levels. As we discussed previously, these ascent regions could be linked to the WCB circulation.

A smaller area of descent is located to the south of the cyclone center (Fig. 6.10c). The dry intrusion could be responsible for this descent.

In the future climate, the first branch of ascent is projected to intensify (blue shading in Figs. 6.10a,c). The most considerable acceleration will be found in the WCB outflow to the west and the north of the cyclone center (Fig. 6.10a). The second branch of ascent will be weaker, at least at middle levels (Fig. 6.10a). The region of descent (dry intrusion) will be stronger at the middle and upper levels (Fig. 6.10c).

b) PV

Figs. 6.10b and 6.10d show stronger PV production along trajectories at the cyclone center. At low levels, the PV increases by around 1.2 PVU in 24 h. The strong low-level PV production is connected to an upper-level PV production that generates an intense PV tower. The diabatically produced PV extends from the surface up to the middle levels, in the area of strong WCB ascent, illustrating the critical role of the WCB for cyclone intensification.

The structure of the WCB outflow (Fig. 6.10a) suggests that the WCB is associated with a cyclonic (PV increasing) and anticyclonic (PV reduction) branch (it might be the same branch wrapping around the cyclone center). In the west-east vertical section, the cyclonically turning branch of the WCB outflow is found above 400 hPa, slightly to the west of the cyclone center. In this region, the upper-level trough is less pronounced and may be eroded by diabatic processes (Binder et al., 2016). However, this signal is not clear, since there are no negative PV changes.

Note that the concentration of strong WCB-related PV production is located in the cyclone center in our analysis. This implies that cyclones are primarily associated with WCBs of type 2, which ascend near to the cyclone center (Martínez-Alvarado et al., 2014).

Besides the PV reduction associated with the WCB outflow, a second region with PV reduction can be found to the south of the cyclone center (Fig. 6.10d). This PV reduction region is located at low levels over the region of the dry intrusion.

Based on the Eulerian analysis (chapter 5) and the current Lagrangian analysis, we note that the cyclone structure and evolution correspond to explosively intensifying cyclones with strong WCBs (Binder et al., 2016). They are linked to pronounced WCB-related diabatic PV production in the cyclone center, a cyclonically breaking upper-level wave, and the formation of a PV tower towards the end of intensification.

The future response of the evolution of PV along the trajectories is shown in Figs. 6.10b and 6.10d as color shading. An enhanced PV production at the cyclone center is projected to extend from the surface to about 400 hPa. The more substantial diabatic processes in the WCB will contribute to the enhanced PV. Note that the PV reduction to the south of the cyclone center (DI-related) will be weaker. Probably it is influenced by turbulent mixing processes. We will investigate this further in the next section.

Enhanced PV production in the cyclonic branch of the WCB outflow will move upward and to the west of the cyclone center. Regarding the second WCB outflow, the anticyclonic branch experience a not straightforward evolution. An additional cross-section across this region will be shown in the next section.

WCB vertical cross section

As we described before, we have identified two WCB branches. The evolution of the first cyclonic branch has been described in detail with the vertical cross-section across the cyclone center. To analyze the second branch, we have constructed a south-north vertical cross-section 8^o eastward of the cyclone center. As before, we analyze the evolution of this airstream using pressure and PV.

a) Pressure

The south-north vertical section across the WCB region shows trajectories ascending almost in the whole region (Fig. 6.11a). A maximum ascent is found at upper levels to the north of the cyclone center, with a pressure change of more than 240 hPa in 24 h. This maximum change can be associated with a strong WCB outflow. The anticyclonic branch reaches probably higher levels, consistent with findings of Martínez-Alvarado et al. (2014).

In the future climate, this WCB branch will reduce its rate of change in pressure at the southern flank of the most vigorous ascent. This will lead to a narrower WCB branch, with the zone of strongest ascend shifted upward and slightly poleward.

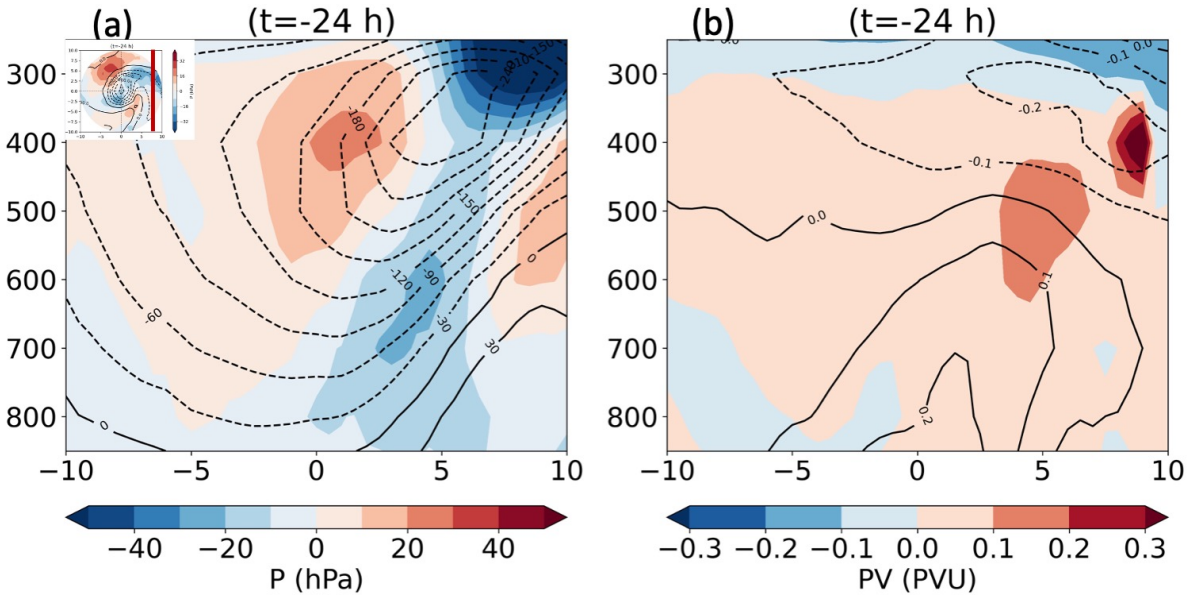

Figure 6.11: South-north vertical cross section through the WCB region [8^o longitude]. Shown are changes in time of (a) pressure and (b) PV along trajectories:[t=0]-[t=-24]. Present-day airstream changes (contours) and their future response (color shading).

b) PV

Fig. 6.11b shows PV production along trajectories between the surface and 500 hPa and PV destruction at upper levels. The region of strongest PV production is located close to the cyclone center, which is consistent with the region of diabatical PV production. At upper levels, the strongest PV destruction is located to the north of the cyclone center. This vertical cross-section exhibits a large area of PV destruction. Thus, the anticyclonic circulation generated by the east-flank WCB branch influences the upper-level downstream flow by amplifying the downstream ridge.

As the climate warms, an enhanced WCB-related PV production will dominate from near the surface up to 300 hPa (Fig. 6.11b). Note that some regions of WCB-related PV destruction will become regions of PV production at upper levels. PV destruction associated with the WCB outflow will move upward and poleward. This future configuration matches up with WCBs ascending faster in the future (Fig. 6.11a). A more vital WCB-related PV production coincides with more substantial precipitation in the warm region (chapter 4, Fig. 4.6). Therefore, the second branch of the WCB located to the east of the cyclone center will play an essential role in the extratropical cyclone dynamics and in the downstream flow in the warmer climate over the North Atlantic.

DI vertical cross section

The Lagrangian composite at 700 hPa and the north-south vertical cross-section shows a region of air parcels descending to the south of the cyclone center. Besides, the decrease of PV along the descending trajectories over this region indicates the presence of a dry intrusion, which can generate strong winds near the surface (Raveh-Rubin, 2017). To examine this dry slot in detail, we have constructed west-east vertical cross-sections 4^o southward of the cyclone center. As before, we analyze the evolution of this airstream using pressure and PV.

a) Pressure

The west-east vertical section across the dry intrusion (DI) region shows strong descent of air parcels almost the whole domain (Fig. 6.12a). A region of ascending air is located farther east of the cyclone center, which can be associated with the WCB. Two regions of strong descent are observed in the vertical cross-section. The first region is found farther west at low levels ($\sim$800 hPa). The second region is located to the east of the cyclone center at middle levels ($\sim$550 hPa). Thus, some DI trajectories arrive at the west of the cyclone moving southeast at low levels and others to the east of the cyclone, moving northeast close to the cyclone center. This is consistent with the cyclonic DI trajectories, which fan out as they descend behind the cold front (Browning, 1997). The cyclonic flow related to the DI contributes to a cloud-free region (Catto et al., 2010) and produces potential instability by wind shear (Raveh-Rubin, 2017).

In a warming climate, the DI trajectories at low levels to the west of the cyclone center will become weaker. In contrast, the trajectories at middle levels to the southeast of the cyclone center will become stronger. A more intense DI to the southeast of the cyclone center might generate conditions for stronger wind gusts near the surface.

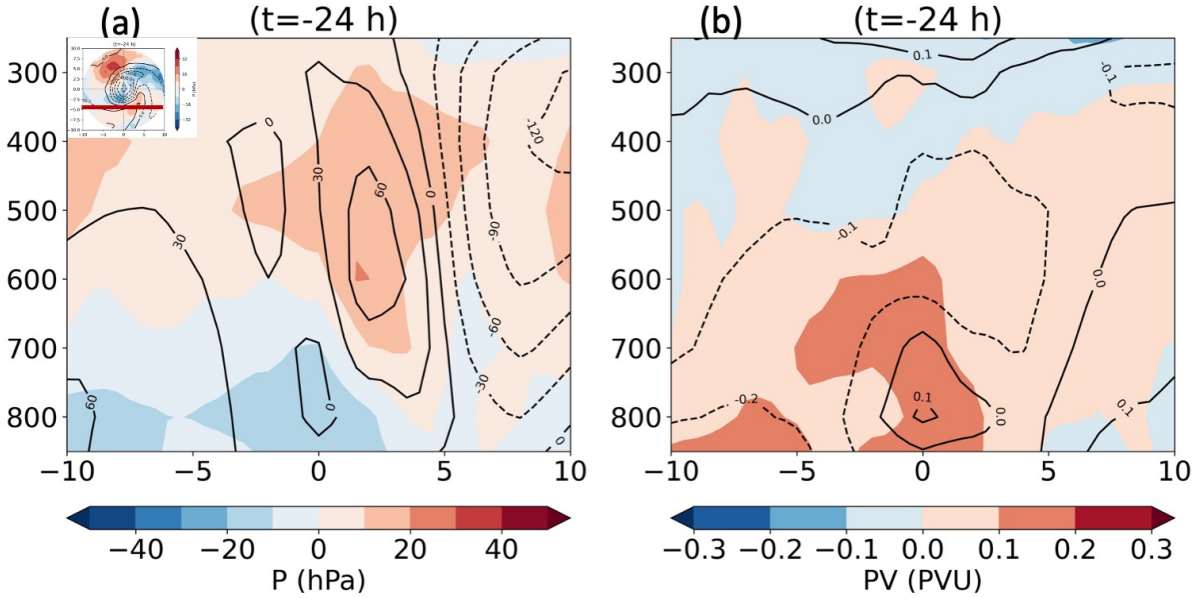

Figure 6.12: West-east vertical cross sections through the dry slot region [-4^o latitude]. Shown are changes in time of (a) pressure and (b) PV along trajectories:[t=0]-[t=-24]. Present-day airstream changes (contours) and their future response (color shading).

b) PV

Fig. 6.12b shows PV changes along trajectories associated with the DI regions. The most considerable PV destruction region is located at low levels to the west of the cyclone center (0.2 PVU in 24 h). DI trajectories southeast of the cyclone are associated with a smaller PV destruction; we can even observe PV production beneath that region. The PV production can be caused by the trajectories traveling at low levels and gaining PV through diabatic processes. Long-wave radiative cooling of the warm sector boundary layer might explain this PV production (Attinger et al., 2021).

Fig. 6.12b shows a generalized, more substantial PV increase along trajectories in a warming climate compared to present-day, such that there will be less PV destruction. Thus, an enhanced diabatic PV at low levels will influence the DI's evolution. PV along DI trajectories are projected to barely change to the west of the cyclone at low levels, and trajectories that arrive near the cyclone center are projected to have a more substantial diabatic PV production beneath, which might be associated with severe weather.

6.5 Discussion

We have used a lagrangian perspective to analyze the WCB, CCB and DI airstreams of extreme cyclones in the North Atlantic from October to March. 7-day backward trajectories have been computed at different pressure levels in the cyclone area. Firstly, we have

analyzed the levels of 700 hPa and 250 hPa in detail.

The temporal evolution of the trajectories has allowed us to identify the period of significant change, 24 h before the cyclone maximum intensity. During this 24 h period, trajectories ending at 700 tend to ascend, while trajectories ending at 250 have a more complex pathway.

Trajectory analysis at specific locations shows that the decreased PV anomaly to the south of the cyclone center in Fig. 5.2c results from a combined effect of a decreased climatological PV in the NA region and the origin of the air masses. They are traveling from lower latitudes and lower altitudes, resulting in the transport of air masses with lower PV towards the cyclone. Diabatic processes are projected to lead to amplified positive anomalies at the cyclone center, where no change in trajectory origin is expected. To the north of the cyclone center, trajectories will undergo significant diabatic heating during ascent from middle levels, which is evident in the θ evolution. PV destruction is observed before trajectories reach the level of 250 hPa.

Trajectories at low levels are mainly diabatically driven. In the future, the enhanced LH might dominate the PV production at the cyclone center, while to the south of the cyclone center, long-wave radiative cooling and turbulent mixing processes might play an important role in the PV production.

In the second analysis, we used Lagrangian composites to identify the regions of substantial diabatic PV changes in 24 h in the present-day climate and the future response. PV along trajectories ending at 700 hPa will have a more substantial diabatic PV production in most cyclone regions (except for the northwest region) at the end of the century. The more robust PV production follows a coma-shape over the warm region, with the strongest increase in the cyclone center. An enhanced PV production matches up with a more vigorous ascent in the WCB region.

At upper levels, the Lagrangian composites have a more complex pattern. In the future climate (Fig. 6.8e), less PV production along trajectories will cover most of the cyclone region (except for the northwest region). We argue that this pattern is due to the WCB outflow, which might have an enhanced diabatic PV production at middle levels but also an enhanced diabatic PV destruction reaching the upper levels.

Cross-sections at the cyclone center show that the LH increases from low to middle levels ($\sim$ 400 hPa). The more substantial diabatic processes in the WCB will contribute to the enhanced PV. Note that the PV reduction to the south of the cyclone center associated with the DI is projected to weaken. Enhanced PV production at the cyclonic branch of the WCB outflow will move upward and upstream of the cyclone center.

PV destruction associated with the so-called anticyclonic WCB outflow will move upward and poleward. A more robust WCB-related PV production coincides with more substantial precipitation in the warm region. Thus, WCB air parcels have a substantial increase

in PV production at middle levels and are associated with strong PV destruction at upper levels. Therefore, the second branch of the WCB located to the east of the cyclone center will play an essential role in the extratropical cyclone dynamics and the downstream flow in the warming climate over the North Atlantic.

PV along DI trajectories will barely change to the west of the cyclone at low levels while DI trajectories arriving near the cyclone center will have a stronger PV production beneath.

Computational restrictions of the Lagrangian analysis always arise as a limitation due to the high number of particles that compose the atmosphere (Schielicke, 2017). Apart from the above, an important limitation of this approach is that trajectories follow the resolved large-scale wind and do not capture fast convective motions. This might introduce an underestimation of the relevance of LH (Steinfeld and Pfahl, 2019).

In summary, this is the first study ever to look at a Lagrangian perspective of cyclone airstreams (based on trajectories) in climate change simulations. We have shown a more vigorous displacement of the WCB and DI airstreams, leading to a faster rolling up of these airstreams and stronger PV anomalies at low levels. At upper levels, the enhanced WCB will also experience a faster rolling up and is projected to lead an enhanced PV destruction downstream of the cyclone center.

7 Thermodynamic and dynamic contributions to the extratropical cyclones precipitation changes

The dynamic and thermodynamic contribution to extreme precipitation in a warming climate has been investigated in recent research (Sugiyama et al., 2010, Phibbs and Toumi, 2016, Pfahl et al., 2017, Zappa, 2019, Li and O'Gorman, 2020). The changes in dynamic contributions to precipitation extreme remain as an open question, and regional variability is found (Pfahl et al., 2017). However, the role of the cyclones in these extreme events is clear (Li and O'Gorman, 2020).

In chapter 4, we have shown a projected precipitation increase associated with extratropical cyclones. This increase is expected due to larger moisture availability in a warming climate. Stronger precipitation is projected at the cyclone center for both seasons, similar to previous studies (e.g. Pfahl et al., 2015, Yettella and Kay, 2017). However, we have also found an increase over the warm region in the winter months (October to March) which the enhanced moisture availability can not explain. Besides, we have noticed that the enhanced precipitation in the warm region will coincide with a stronger ascent. Given this correlation, in this chapter, we will explicitly decompose the precipitation into contributions from atmospheric thermodynamics and dynamics.

Thus, this chapter aims to find the contribution of dynamics and thermodynamics to future changes in cyclone precipitation. We again focus on the North Atlantic region and intense cyclones (10% strongest cyclones) in the extended winter (October-March).

7.1 Data and methods

Precipitation extremes scaling

Following Pfahl et al. (2017), we approximate the precipitation with a physical scaling diagnostic, which has been applied to evaluate extreme precipitation on a large scale in climate simulations (O'Gorman and Schneider, 2009, Sugiyama et al., 2010):

$$P_e \sim -\left\{ \omega_e \frac{dq_s}{dp}\bigg|_{\theta^*} \right\} \tag{11}$$

Here, the precipitation amount at each model grid point P_e is related to the corresponding vertical pressure velocity ω_e and the vertical derivative of the saturation specific humidity

$\frac{dq_s}{dp}$ at constant saturation equivalent potential temperature θ^*. $\{.\}$ represents a mass-weighted integral over the troposphere. The right-hand side of the equation 11 is an estimate of the column integrated net condensation rate (see Pfahl et al., 2017, for more details) under saturated conditions.

We compute the precipitation scaling for the 10 % strongest storms in the extended winter using 10 ensemble members from the CESM-LE. Similar to the composite analysis, a radial grid with the pole centered on the cyclone center is generated for each storm. The following fields are extracted at the time of maximum intensity to estimate the precipitation in each storm: surface pressure (2D), temperature and omega (14 pressure levels).

The temperature on pressure levels is used to obtain q_s from a modified Tetens formula (Simmons et al., 1999). The vertical integral is computed over all the levels with ascent ($\omega_e < 0$) from 1000 hPa up to 50 hPa at each grid point of the cyclone area. The resulting precipitation estimate for each storm is used to construct the mean composites for the present-day, the future climate, and by subtraction, the future response.

An advantage of this scaling analysis is that it can be used to decompose the change into thermodynamic and dynamic contributions. To this end, the thermodynamic scaling is computed with equation 11, but neglecting time variations in the vertical velocity. An averaged ω_e composite is obtained for intense cyclones in the present-day similar to Fig. 4.4c but for all pressure levels listed above. Then, at each grid point, ω_e is replaced by this average for both present-day and future climate, and the thermodynamic contribution to the projected scaling is obtained as the difference between the two scaling estimates obtained with constant ω_e.

Differences between the change in full and thermodynamic scaling are considered to provide the dynamic contribution change. They indicate regions where such future variations in ω_e are particularly relevant for the estimated precipitation response (Pfahl et al., 2017).

An alternative estimate of the dynamic contribution can be obtained by keeping temperature and surface pressure constant and varying the vertical velocity. Averaged temperature and surface pressure composites are obtained for intense cyclones in the present-day similar to the Fig. 4.4e but for all pressure levels listed above. Thus, the dynamic contribution is directly computed with the equation 11, but we neglect time variations in the temperature and surface pressure. The two estimates of the dynamic contributions (residual vs. direct estimate based on equation 11 and keeping temperature and surface pressure constant) are compared to obtain an additional check of the consistency of the decomposition.

7.2 Comparison of simulated precipitation and scaling estimate

The ability of the precipitation scaling to capture the present-day precipitation composite as well as its projected future change is shown in Fig. 7.1. In the present-day climate (contours in Fig. 7.1), the precipitation scaling tends to produce larger precipitation downstream and over the cold front (Fig. 7.1c). Through the absolute changes in precipitation (Fig.s 7.1a and 7.1b) we identify, in general, a similar structure, with the maximum increase located close to the cyclone center and over the warm region.

However, the precipitation scaling increase is more concentrated downstream, whereas the directly simulated precipitation increase is also high to the west of the cyclone center. In Fig. 7.1e, the overestimation downstream of the cyclone center and the underestimation to the west of the center are more evident.

Precipitation changes in percentage (Fig. 7.1b and 7.1d) show that the precipitation scaling reproduces adequately changes over the regions with large precipitation increase, for instance, the largest precipitation increase to the east of the cyclone center in the warm region (Fig. 7.1e). As expected, we found a larger positive bias, over the regions with low precipitation rate (upstream region and south of the cyclone center), because the assumptions underlying the scaling analysis, such as saturation over the entire atmospheric column, hold better in regions of strong precipitation. Note that a slight underestimation is located in the warm front zone.

Previous studies have suggested that a larger bias can result from the lack of the precipitation efficiency parameter (e.g., Singh and O'Gorman, 2013). Nevertheless, this term plays an essential role for convective precipitation extremes on short time scales and small spatial scales (Pfahl et al., 2017); and the CESM-LE model can not resolve these processes. We discuss this further in section 7.4.

Thus, we have demonstrated that the precipitation scaling can reproduce the main structural changes of the storm-scale precipitation, but also has some biases in regions of lower precipitation rates.

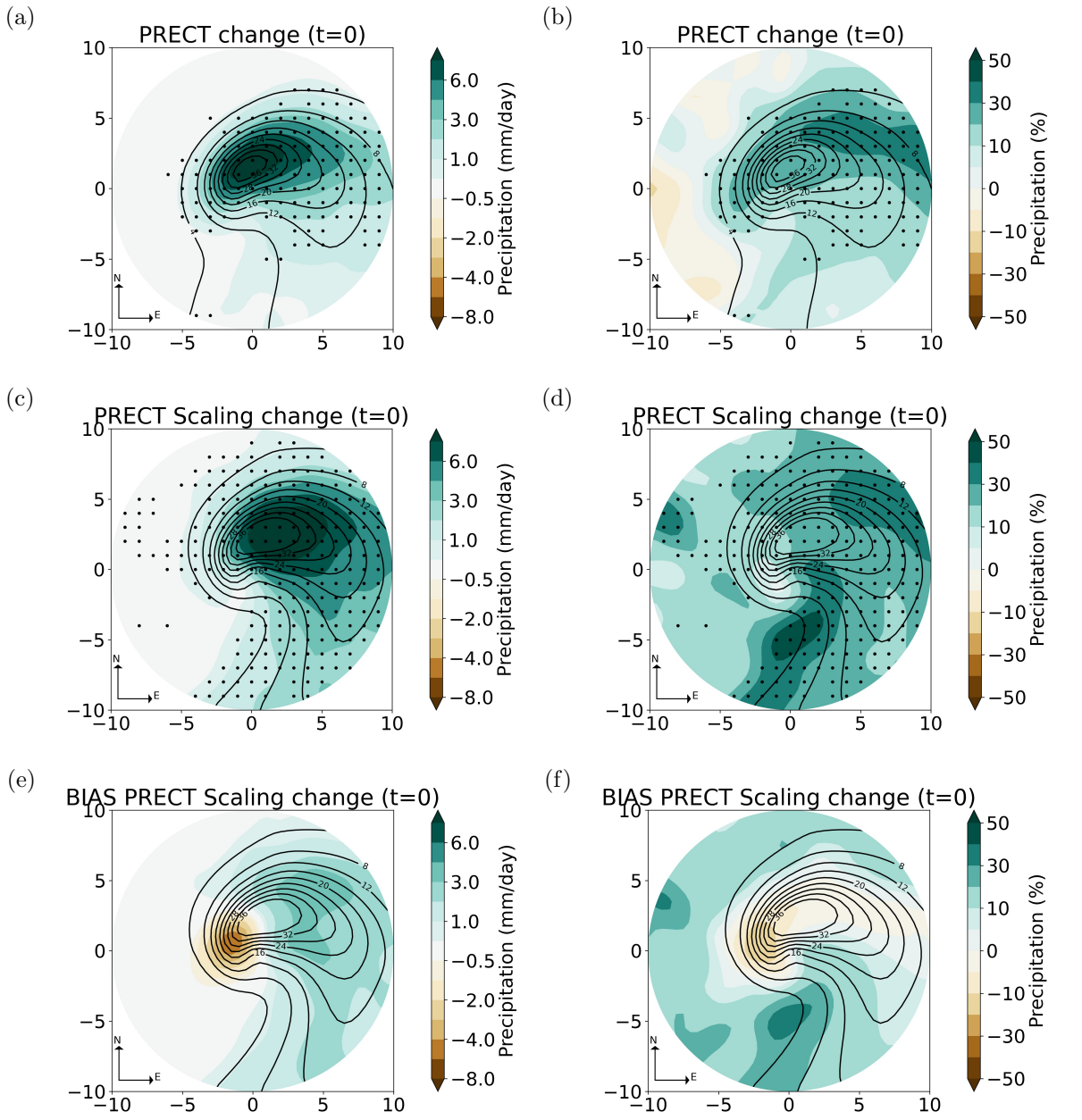

Figure 7.1: Present-day precipitation (contours) and its projected future change (colour shading) based on (a,b) direct model output and (c,d) the scaling estimate from equation 11, as well as (e,f) differences between scaling and model output. Panels (a,c,e) show the absolute change in mm/day, panels (b,d,f) the relative change in %. Stippling denotes regions of ensemble agreement on the sign of change, i.e., more than 80% of the ensemble members indicate a change of the same sign.

7.3 Dynamic and thermodynamic contributions to cyclone precipitation changes

Fig. 7.2 shows the thermodynamic and dynamic contributions to the projected changes in precipitation scaling. Thermodynamic contributions are responsible for most of the increase in the regions of high present-day precipitation rates (contours in Fig. 7.2). For instance, the coma-shape of the precipitation will be enhanced by these thermodynamic changes. Changes in percentage (Fig. 7.2b) indicate a maximum precipitation increase of 25% due to these thermodynamic changes, which is slightly lower than the estimated increase based on global-mean surface warming and the Clausius-Clapeyron equation obtained in chapter 4.

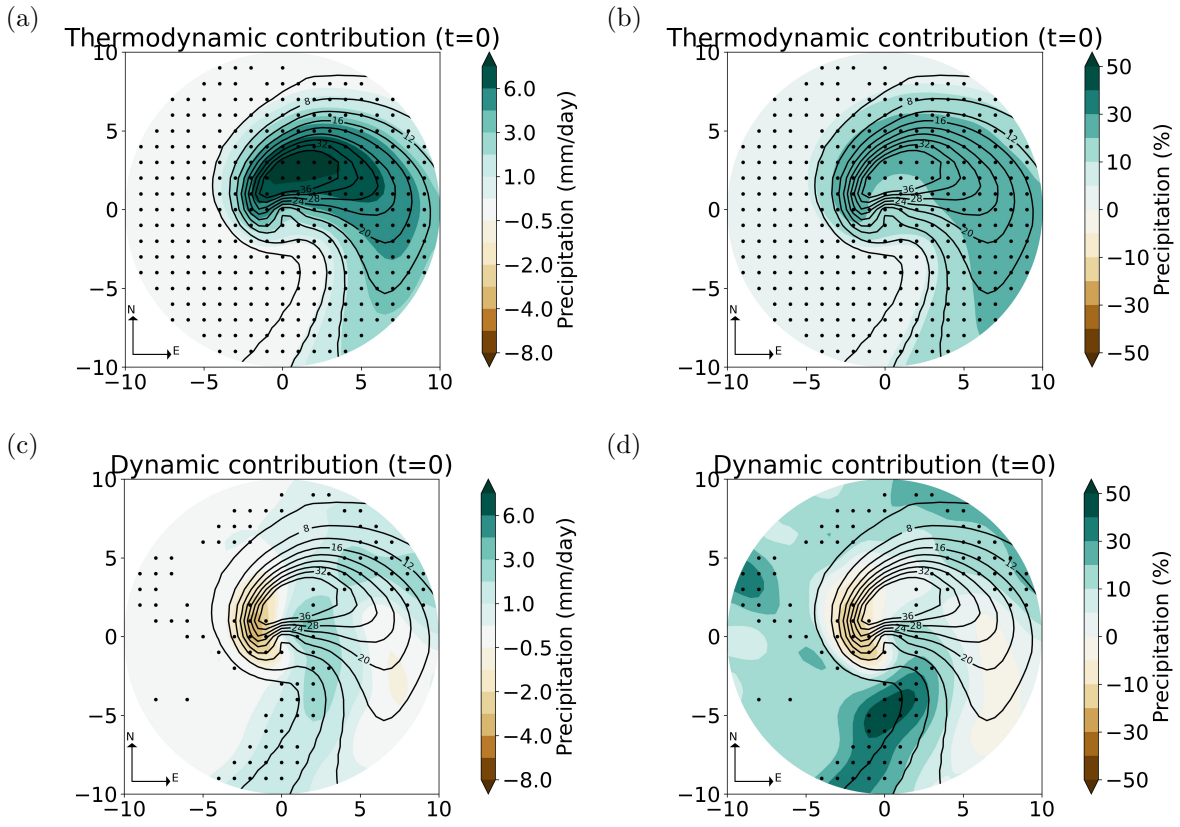

Figure 7.2: Present-day precipitation (contours) and its projected future change (color shading) by (a,b) thermodynamic and (c,d) dynamic contributions. Panels (a,c) show the absolute change in mm/day, panels (b,d) the relative change in %. Stippling denotes regions of ensemble agreement on the sign of change, i.e., more than 80% of the ensemble members indicate a change of the same sign.

The dynamic contribution is projected to produce a positive response downstream and a negative response upstream of the cyclone center (Fig. 7.2c). In particular, the dynamic contribution will be responsible for heavier precipitation in the frontal zones and weaker

precipitation directly to the west of the cyclone center. The weakening effect of the dynamic contribution to the west of the cyclone center compensates for the increase of the thermodynamic contribution, leading to a weaker response of the full scaling in this region (Fig. 7.1c).

Fig. 7.2d shows the dynamic contribution changes in percentage. A precipitation increase between 5% and 20% over the region of the warm front will be associated with the dynamics, whereas in the cold front area, the increase exceeds 50%. We have discussed that the bias is large over the cold frontal region. However, the dynamic contribution increase is even larger than the bias in some frontal regions (a difference of around 5%).

These results partly differ from the earlier study of Yettella and Kay (2017); they showed that precipitation increases associated with mid-latitude cyclones could be explained by thermodynamic changes only. Note that Yettella and Kay (2017) performed a regional analysis instead of a storm-scale analysis as we did. The relevance of the storm-scale analysis is outlined by Li and O'Gorman (2020); they suggested that extreme precipitation events in the extratropics are typically associated with precipitation structures in extratropical cyclones rather than gridpoint storms.

As described in methods, we have also computed the dynamic contribution by keeping temperature and surface pressure constant in equation 11 as an additional check of the consistency of the decomposition. Here, the dynamic response is lower in absolute and in percentage units. Hence, the influence of the dynamics to enhance the precipitation in the cold front region has to be taken with caution. However, the enhanced precipitation due to the dynamic contributions is still found in some frontal zones (increases between 5 to 20%). On the contrary, the decrease upstream of the cyclone center is more evident. The dynamic contribution response has a pattern similar to the vertical velocity response at 850 hPa (Fig. 4.6e), where significant changes occur close to the cyclone center, decrease to the west and increase to the east of the cyclone center. The latter extends to the warm front.

7.4 Discussion

In this chapter, the extreme precipitation scaling is used for the first time to analyze the precipitation changes associated with extratropical cyclones. In a warming climate, the 10% most intense storms over the North Atlantic have been investigated in the winter season. The precipitation scaling reproduces simulated precipitation changes reasonably well over the regions of heavy precipitation. However, precipitation intensity is overestimated over regions of low precipitation, for example, to the south of the cyclone center.

We have explored the thermodynamic and dynamic contributions to the full precipitation scaling response. Thermodynamic contributions are responsible for most of the precipitation increase to the north and downstream of the cyclone center. Dynamic contributions

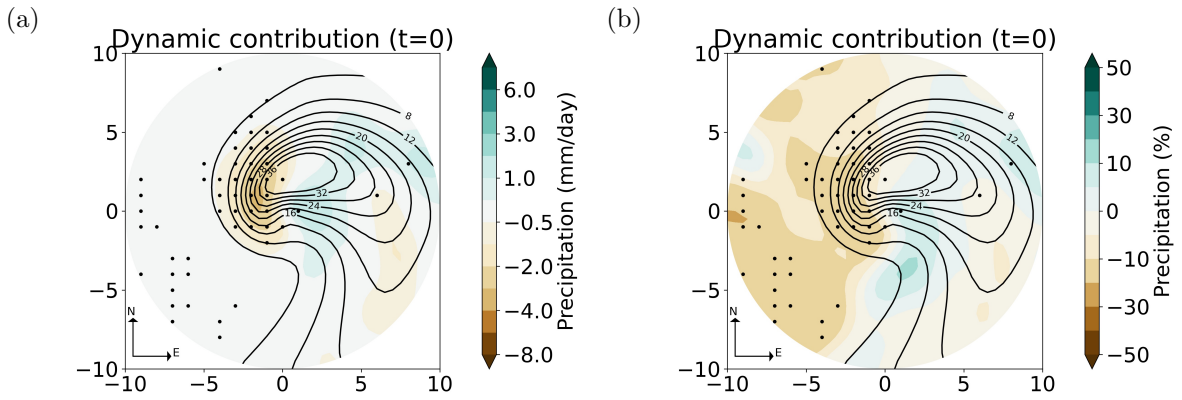

Figure 7.3: Present-day precipitation (contours) and its projected future change (color shading) by dynamic contribution (ω varying). Panel (a) shows the absolute change in mm/day and panel (b) the relative change in %. Stippling denotes regions of ensemble agreement on the sign of change, i.e., more than 80% of the ensemble members indicate a change of the same sign.

enhance the precipitation in the frontal regions and weaken the precipitation to the west of the cyclone center.

A poleward and downstream expansion of the precipitation associated with the warm front has been found in recent studies (Sinclair et al., 2020). Our results suggest that these changes are related to enhanced ascent (dynamic contribution) in this region. Sinclair et al. (2020) showed that such an increased ascent could be attributed to an increase in diabatic heating.

Increased latent heat as a driver of precipitation increase with a super-Clausius-Clapeyron rate through the dynamic contribution has also been found in regional experiments (Nie et al., 2018). However, the dynamic contribution changes are not straightforward in the mid-latitudes. The complexity of the dynamic tendency in extreme events is discussed by Norris et al. (2019) using the CESM-LE. For instance, a positive dynamic tendency is observed in the tropics, with a similar impact as the thermodynamics or even greater, resulting in a $> 25\%K^{-1}$ precipitation increase over the tropical eastern Pacific. On the contrary, in the mid-to-high latitudes, the influence of changes in dynamics is more negligible, so that the precipitation increase follows the Clausius-Clapeyron rate.

The present study has some caveats, as is described in the following. The scaling estimate has relatively large biases in some regions, most regions of small precipitation intensities. The main reason is that the scaling assumes saturation throughout the atmosphere. We have highlighted the relevance of the dynamic contribution to the precipitation increase over frontal precipitation. However, the two alternative estimates of the dynamic contributions shown in Figs. 7.2 and 7.3 have a different intensity pattern. The main differences are in the distribution and magnitude of the amplification in the frontal precipitation. On the contrary, the reduction to the west of the cyclone center is more robust across these

estimates.

In summary, we have shown that the scaling analysis that was originally developed for precipitation extremes can provide valuable insights into projected changes of cyclone related-precipitation, in particular in regions of intense precipitation near the cyclone center. Also, we found that future changes in vertical wind velocities, in addition to altered thermodynamic conditions, can lead to changes in precipitation in specific regions relative to the cyclone center, in particular upstream, where the reduced ascent is projected to partly compensate for the enhanced moisture availability, and potentially also near the cold and warm front.

8 Conclusion and outlook

8.1 Conclusions

In this thesis, an analysis of cyclone dynamics and wind changes in a warming climate has been performed with the help of coupled climate model simulations and a potential vorticity framework. A cyclone tracking scheme as well as composite, PV inversion, trajectory and precipitation scaling diagnostics have been applied to 10 CESM-LE ensemble members. The model reproduces cyclone frequencies over the North Atlantic well, in particular over the main storm track regions. Model biases are primarily associated with the representation of short-lived systems.

At the end of the century, projected changes in cyclone frequencies are relatively small, with a general tendency towards slight decreases in many regions. Nevertheless, for the 10% most intense cyclones, an eastward displacement of the main oceanic storm track over the eastern North Atlantic is projected, associated with an increase in cyclone track density over northwestern Europe. These findings on cyclone frequency changes are generally consistent with previous studies using other climate models and cyclone tracking approaches (Pinto et al., 2009, Ulbrich et al., 2009, Zappa et al., 2013). Also, projected cyclone intensity changes, measured in terms of lower-tropospheric maximum relative vorticity or wind speed, are relatively small, again consistent with previous studies (Zappa et al., 2013, Catto et al., 2019).

In spite of such small overall intensity changes, our composite analysis indicates structural changes in the typical wind and precipitation patterns associated with intense North Atlantic cyclones. In particular, an increase of wind velocities in the warm sector southeast of the cyclone center, potentially related to strengthening the low-level jet ahead of the cold front, and a southeastward broadening of the associated footprint of strong winds is projected. While some previous studies on future wind changes in cyclones have not detected such a robust change (Michaelis et al., 2017), consistent results regarding the broadening wind footprint have been obtained from idealized simulations (Sinclair et al., 2020) and a recent analysis of CMIP6 model projections (Priestley and Catto, 2022). Together with the eastward shift of storm tracks, this may lead to increased wind hazards in western Europe, which has also been seen in other model studies (Mölter et al., 2016).

In order to better understand the dynamical mechanisms behind these wind speed changes, a PV anomaly and inversion analysis have been conducted. PV inversion has been used previously to study future changes in cyclone propagation (Tamarin-Brodsky and Kaspi, 2017, Tamarin and Kaspi, 2017), but here it has been used for the first time for the investigation of future changes in the near-surface wind patterns associated with midlatitude cyclones. In agreement with many previous studies (Pfahl et al., 2015, Marciano et al., 2015, Michaelis et al., 2017, Zhang and Colle, 2018, Sinclair et al., 2020) we find an increase in lower-tropospheric PV near the cyclone center and fronts that is most likely due

to increased latent heating in a warmer and thus more humid climate (Büeler and Pfahl, 2019).

According to our PPVI analysis, this amplified low-level PV is associated with enhanced cyclonic wind velocities around the cyclone center, indicating that increased latent heating contributes to broadening the wind footprint in the warm sector. However, it is not the sole cause of this broadening, as also PV changes in the upper troposphere go along with an increase of south-westerly winds in this region. More specifically, a dipole change in upper-tropospheric PV with a projected PV increase near the cyclone center and a decrease to the south and southwest are associated with enhanced upper-level PV gradients in the region ahead of the cold front and thus increased poleward flow throughout the troposphere. In contrast to the warm region southeast of the cyclone center, where wind changes associated with upper- and lower-layer PV changes superimpose in a constructive way, these wind changes partly compensate each other upstream of the cyclone center, where net wind speed changes are thus smaller. Note that the projected wind increase in the warm sector is robust across the different cyclone intensity classes and ensemble members analyzed here and is also seen in the balanced wind response of the PV inversion. However, the PPVI does not exactly reproduce the full wind changes in a quantitative way, and the corresponding results should thus be interpreted with care.

In summary, the PV analysis performed in this study provides insights into the role of altered upper-tropospheric dynamics and increased latent heat release in a warmer climate for future changes in near-surface wind fields around extratropical cyclones. The projected broadening of the wind footprint southeast of the cyclone center that can be explained by a combination of these processes may have important consequences for future changes in wind hazards. This study thus contributes to reducing the uncertainties associated with future changes in near-surface winds in cyclones (cf. Catto et al., 2019) through improved process understanding.

In chapter 6, for the first time, a Lagrangian trajectory analysis has been applied to analyze typical air streams and determine the drivers of changes in PV anomalies in extratropical cyclones in a warmer future climate. This Lagrangian approach shows that the vertical motion along important air streams, in particular the warm conveyor belt but also parts of the Dry intrusion, is projected to amplify. Especially for the WCB, this amplification is directly related to enhanced diabatic heating. Trajectory analysis at specific locations shows that the decreased PV anomaly to the south of the cyclone center at upper levels (see again Fig. 5.2c) results from a combined effect of a decreased climatological PV in the North Atlantic region and the altered origin of the air masses, which originate from lower levels and more southerly latitudes. In contrast, the increase of PV anomalies at the cyclone center will likely be driven by enhanced diabatic heating throughout most of the troposphere. To the north of the cyclone center, trajectories experience significant diabatic heating during ascent, but also a PV decrease reaching the level of 250 hPa, leading to overall small changes of PV anomalies in the simulated future climate. Changes in diabatic heating play an important role for trajectories at low levels.

As mentioned before, precipitation is projected to increase in the entire cyclone region, according to our composite analysis. We have applied a precipitation scaling analysis to investigate the processes behind these changes. The full future precipitation response is decomposed into dynamic and thermodynamic contributions. This analysis shows that the future precipitation increase will generally be related to changes in thermodynamics, that is, the higher atmospheric moisture content in a warmer climate. The dynamic contribution amplifies the precipitation increase over frontal regions and reduces the intensity upstream of the cyclone center. However, in particular, the amplification over the frontal regions is associated with substantial uncertainties due to biases of the scaling approach and inconsistencies between the two different approaches to determine the dynamic contribution. Nevertheless, it is shown that a better representation of dynamic processes could improve the future projections of extreme precipitation on a storm-scale.

8.2 Outlook

The results from this thesis show that there is a range of options for future research. Here, we describe some of these options.

Cyclone identification method

In this study, the SLP contour method introduced by Wernli and Schwierz (2006) has been employed to identify cyclones. A complementary perspective of cyclone structures may be obtained by using other methods. We suggest identifying the NA cyclones in the CESM-LE simulations with the kinematic method described by Schielicke et al. (2016). A comparison of these two methods would be helpful to have a bigger picture of the storm tracks response in the NA as the planet warms. This complementary perspective is strongly suggested for the analysis of cyclone structure, for example, cyclone size and intensities (Schielicke et al., 2016).

PPVI complementary experiments

Regarding the PPVI tool, a complementary analysis can be the examination of the relation of PV anomalies to the cyclone wind field in summer and for the 10% strongest storms. However, as we mentioned before, the imperfect knowledge of boundary conditions leads to some errors in the PV inversion. The uncertainty is greater in the separation between low-level PV anomalies and lower boundary θ-anomalies (see the conclusions in chapter 5). Thus, we consider it a helpful step to first look at the definition of the boundary conditions. A set of experiments to find adequate boundary conditions at low levels might help to reduce the errors.

PV evolution along trajectories

The PV along trajectories has a complex evolution until they reach the level of 250 hPa. We suggest a study to quantify the latent heat contributions in the ascending airstream, similar to Steinfeld and Pfahl (2019). A complementary study can be conducted because the climatological PV decreases at upper levels. Thus, the final values are lower than the response of PV anomalies found in the Eulerian composites, which can lead to a confusing interpretation of the results. Thus, we suggest an explicit calculation of PV anomalies along the trajectories.

Dynamic contributions to cyclone-related precipitation

The scaling analysis points to a complex pattern of the dynamic contribution to future precipitation changes. Therefore, a more extensive analysis is suggested to better understand the processes behind extreme events. As a first stage, a new subset of data can be investigated, for example, the 1% strongest cyclones. Here, the increase in cyclone-related precipitation is expected to be larger, and it is shown that the precipitation diagnostic works well in heavy precipitation regions. Since the heaviest precipitation occurs before the cyclone maximum intensity, precipitation 12 hours prior to maximum intensity can also be examined. A second stage is associated with a numerical inversion of the quasi-geostrophic omega equation (Li and O'Gorman, 2020) at a storm-scale. This study could explain the changes in vertical velocity due to different physical contributions. Some studies have explored the inversion of this equation, but they compute the terms in idealized models (e.g., Sinclair et al., 2020) or at individual grid points (e.g., Li and O'Gorman, 2020)

A Unrotated vs rotated composites in the North Atlantic (ensemble number 1)

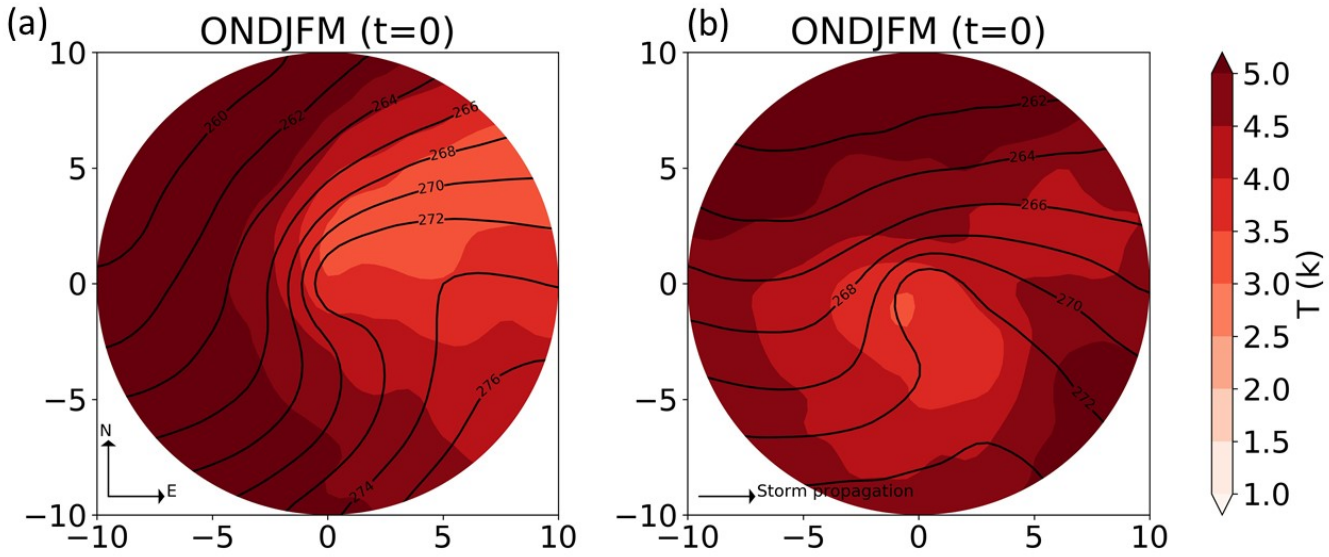

Figure A.1: Cyclone temperature composites response for winter in the North Atlantic. (a) Non-rotated and (b) rotated in the direction of the storm's displacement. Present-day mean is overlaid as black contour lines and future response is shaded. The composites are shown at the time of maximum intensity (time=0). Intense storms (10% strongest) are averaged for the ensemble member number 1 of the CESM-LENS dataset. Present-day: 361 storms and future climate: 312 storms.

B Composites for all cyclones in the North Atlantic (ensemble number 1)

B.1 Temporal evolution

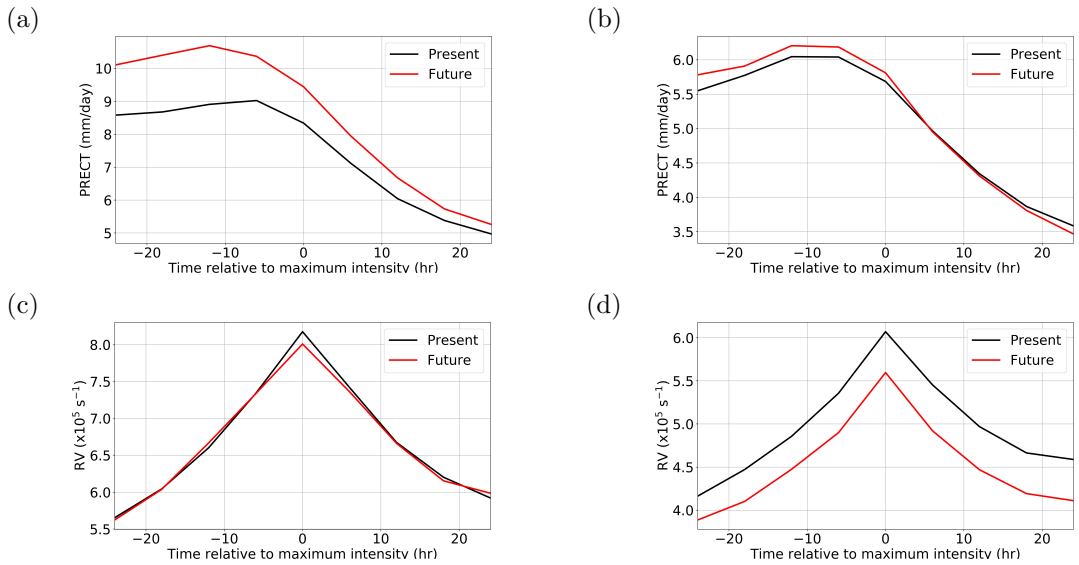

Figure B.1: (a,b)Precipitation and (c,d) relative vorticity composite cyclone lifecycles for (a,c) winter and (b,d) summer in the North Atlantic. The black line represents present (1990-2000) and the red line represents future (2091-2100). Precipitation is averaged within 5^o of the cyclone centre and relative vorticity within 2.5^o of the cyclone centre.

B.2 Intense - all cyclones difference

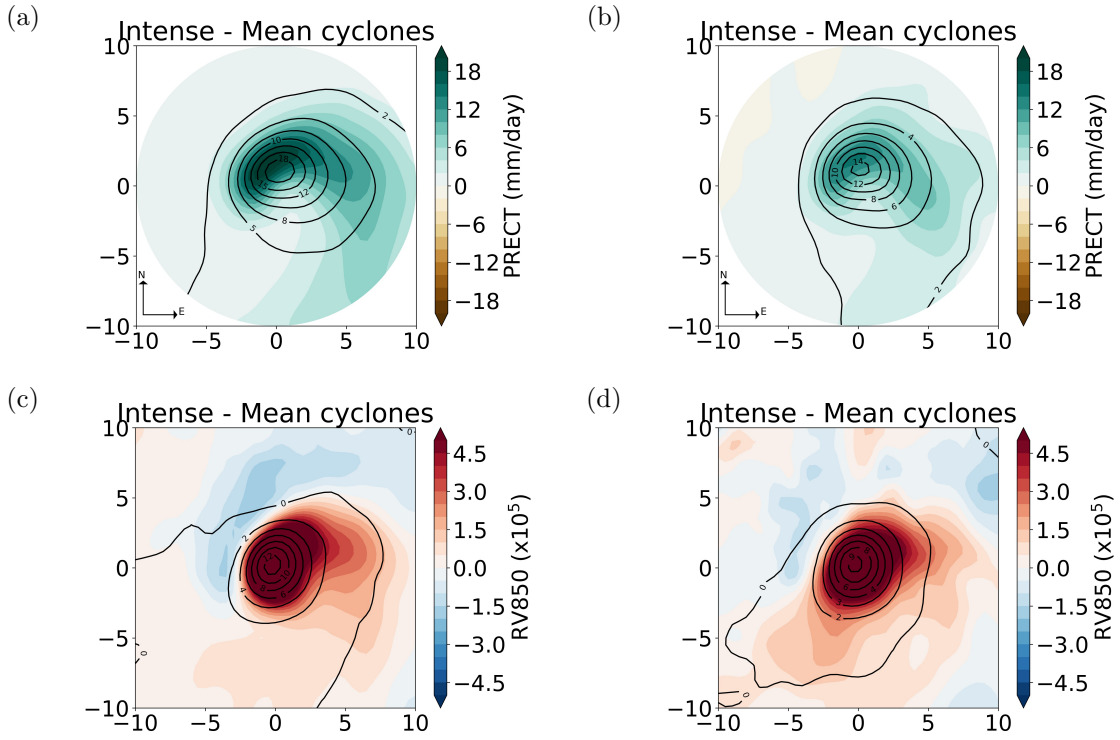

Figure B.2: Composites difference between intense and all cyclones in (a,b) precipitation and (c,d) relative vorticity for (a,c) winter and (b,d) summer in the North Atlantic. Present-day mean is overlaid as black contour lines. The composites are in the maximum intensity (time=0).

B.3 All cyclones response to the warming climate

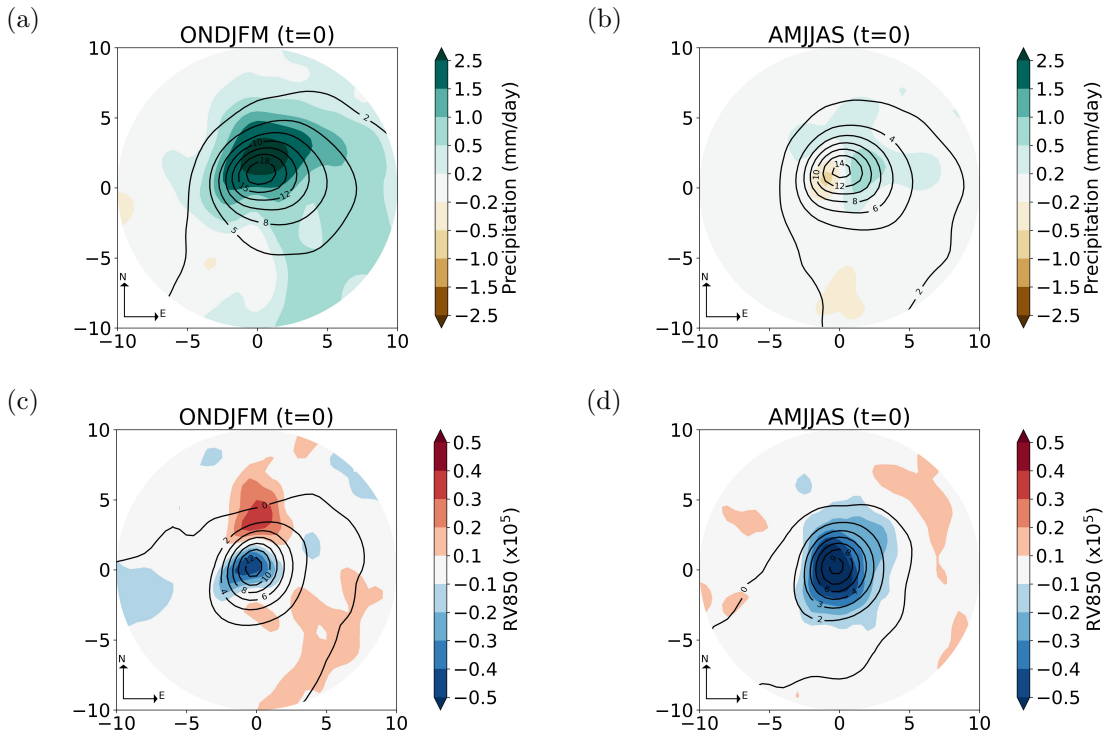

Figure B.3: Cyclone (a,b) precipitation and (c,d) relative vorticity composites response for (a,c) winter and (b,d) summer in the North Atlantic region. Present-day mean is overlaid as black contour lines. The composites are in the maximum intensity (time=0).

C PPVI supplement

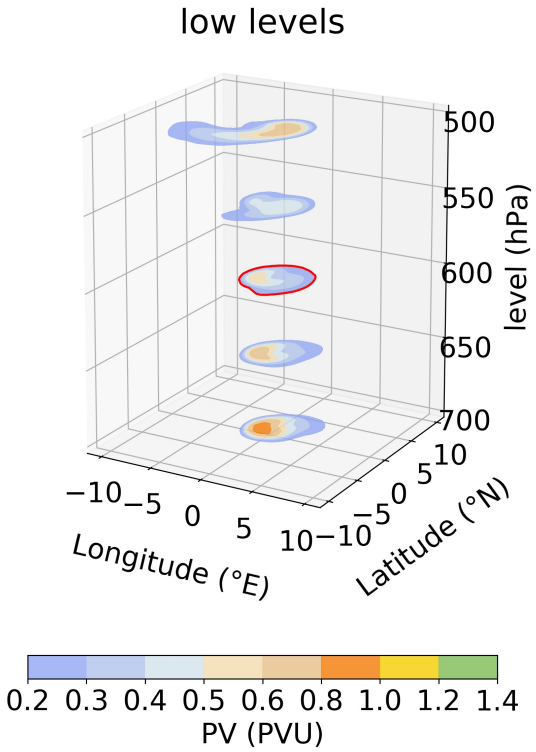

Figure C.1: Present-day composites of horizontal PV distribution at different levels for extreme cyclones. The separation level at 600 hPa is contoured in red. The composites are shown at the time of maximum intensity (time=0). Extreme cyclones are defined as the 1% strongest systems in terms of maximum RV850.

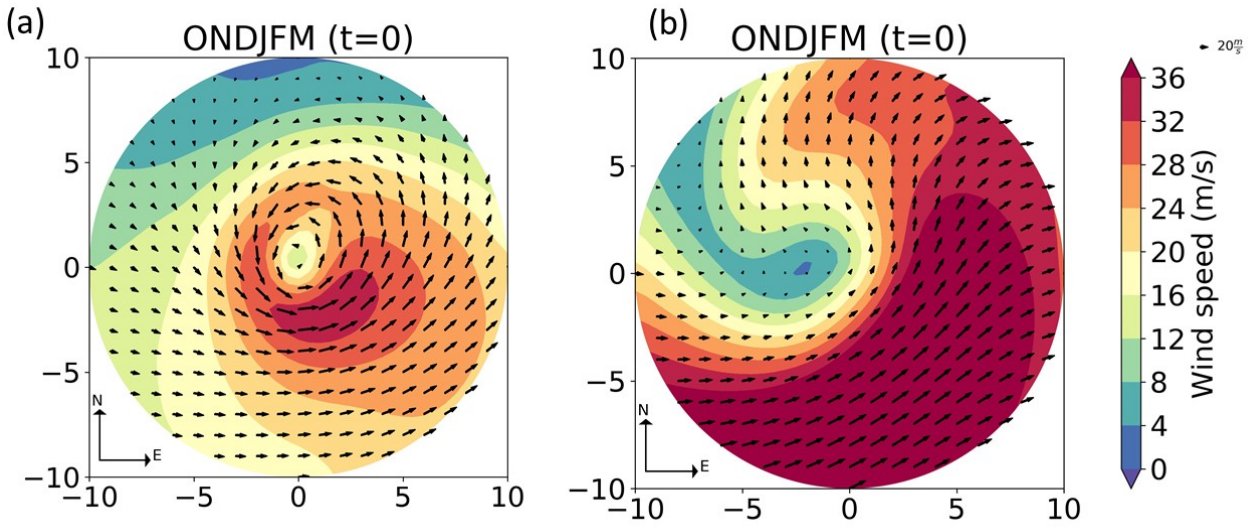

Figure C.2: Present-day composites for extreme cyclones of (a) wind speed at 850 hPa and (b) wind speed at 250 hPa for winter in the North Atlantic region. The composites are shown at the time of maximum intensity (time=0).

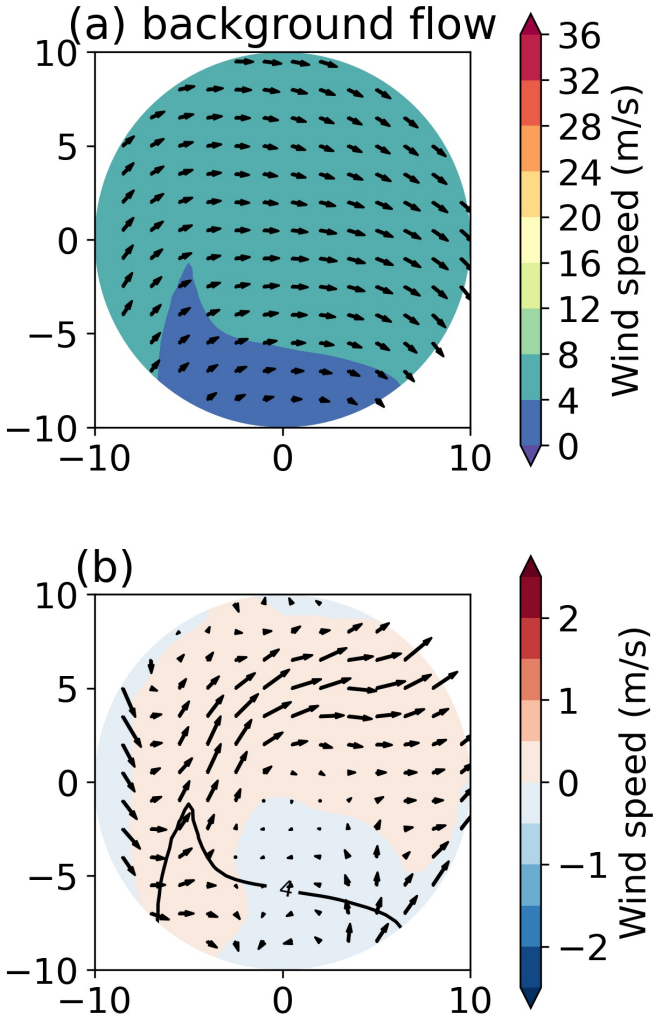

Figure C.3: Wind composites obtained from inverting the background PV at 850 hPa in (a) present-day climate and their (b) future change.

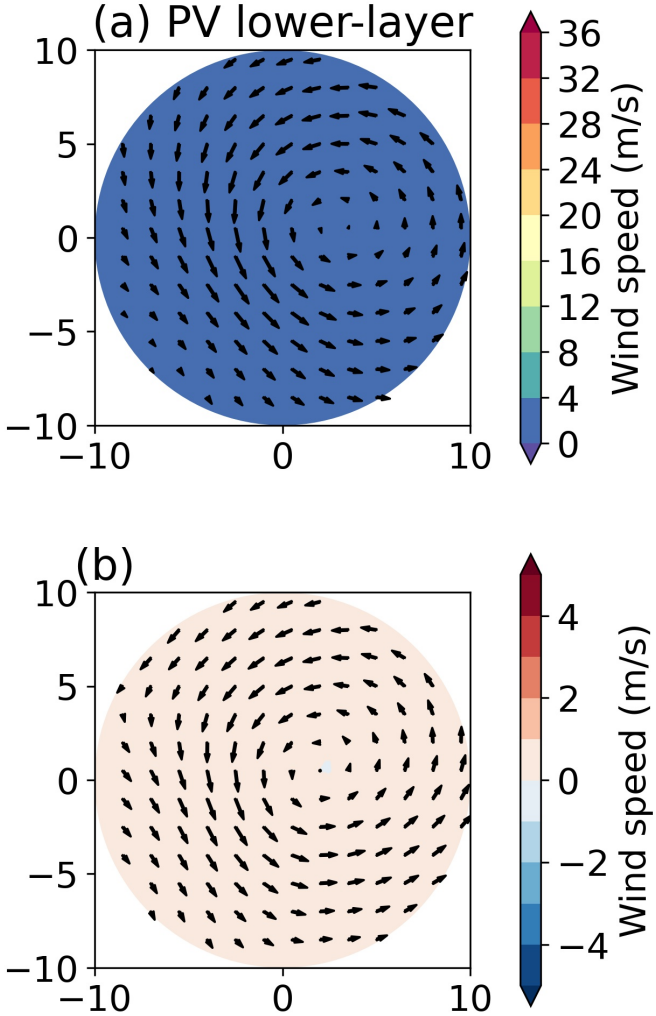

Figure C.4: Wind composites at 250 hPa in present-day climate (a) and their future change (b). The wind composite is obtained from inverting the lower-layer PV anomalies.

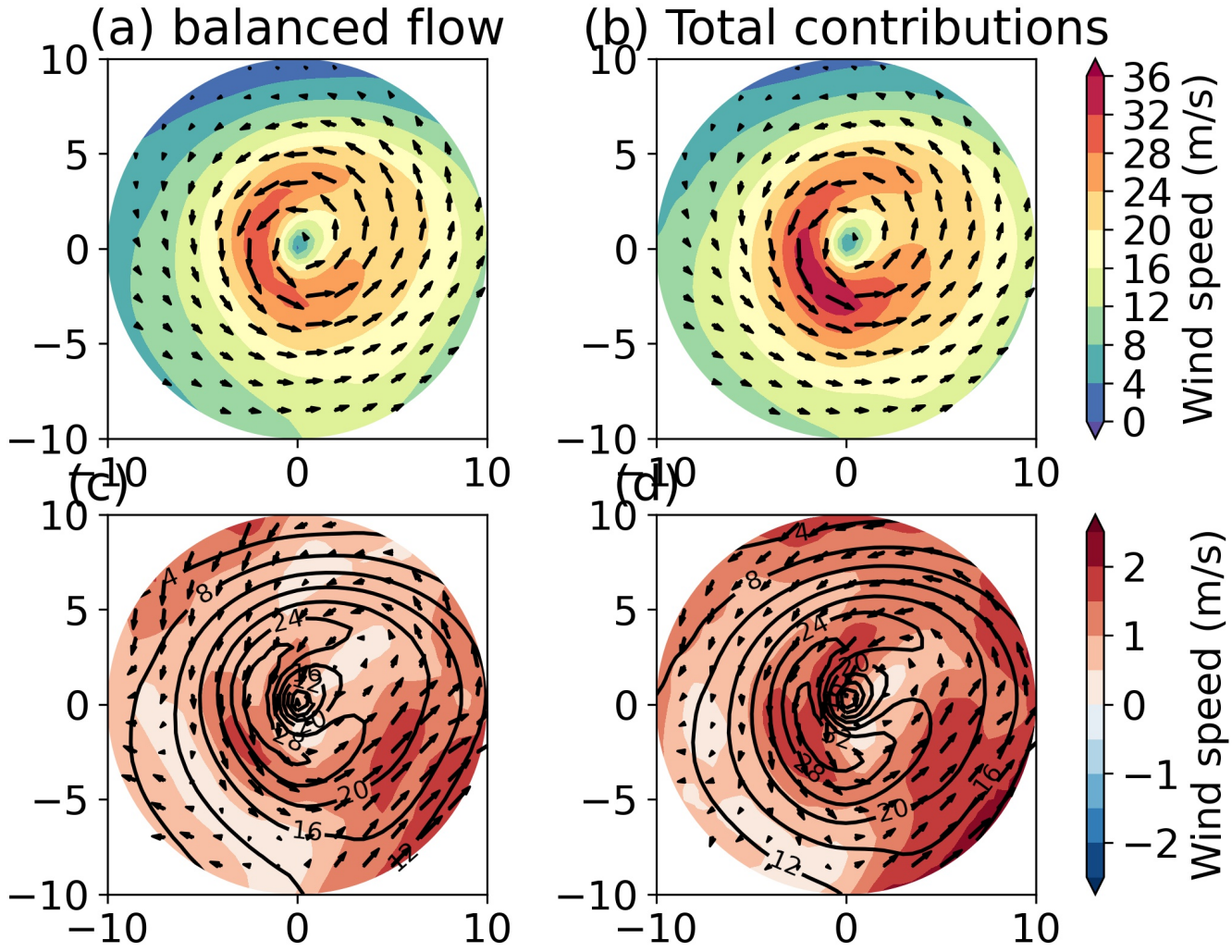

Figure C.5: Internal consistency of the wind flow at 850 hPa. The balanced flow (a,c) and the sum of the individual contributions (b, d) are compared in present-day climate (a, b) and their future change (c, d).

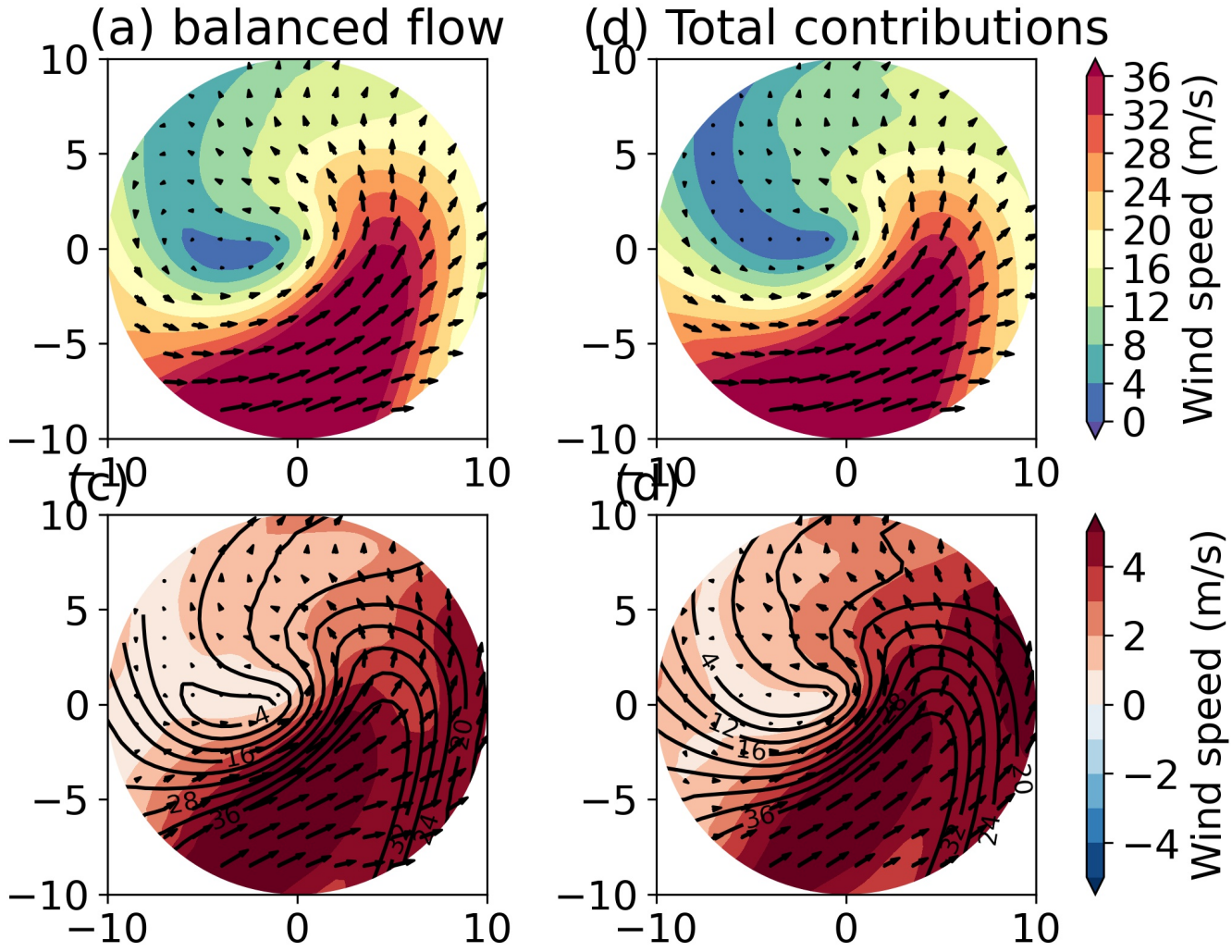

Figure C.6: Internal consistency of the wind flow at 250 hPa. The balanced flow (a, c) and the sum of the individual contributions (b, d) are compared in present-day climate (a, b) and their future change (c, d).

References

Ahmadi-Givi, F., Graig, G. and Plant, R. (2004). The dynamics of a midlatitude cyclone with very strong latent-heat release, *Quarterly Journal of the Royal Meteorological Society* **130**(596): 295–323.

Alpert, P., Osetinsky, I., Ziv, B. and Shafir, H. (2004). Semi-objective classification for daily synoptic systems: Application to the eastern mediterranean climate change, *International Journal of Climatology: A Journal of the Royal Meteorological Society* **24**(8): 1001–1011.

Attinger, R., Spreitzer, E., Boettcher, M., Wernli, H. and Joos, H. (2021). Systematic assessment of the diabatic processes that modify low-level potential vorticity in extratropical cyclones, *Weather and Climate Dynamics* **2**(4): 1073–1091.

Baatsen, M., Haarsma, R. J., Van Delden, A. J. and De Vries, H. (2015). Severe autumn storms in future western europe with a warmer atlantic ocean, *Climate Dynamics* **45**(3): 949–964.

Barnes, S. L. and Colman, B. R. (1993). Quasigeostrophic diagnosis of cyclogenesis associated with a cutoff extratropical cyclone-the christmas 1987 storm, *Monthly weather review* **121**(6): 1613–1634.

Bengtsson, L., Hodges, K. I. and Keenlyside, N. (2009). Will extratropical storms intensify in a warmer climate?, *Journal of Climate* **22**(9): 2276–2301.

Binder, H., Boettcher, M., Joos, H. and Wernli, H. (2016). The role of warm conveyor belts for the intensification of extratropical cyclones in northern hemisphere winter, *Journal of the Atmospheric Sciences* **73**(10): 3997–4020.

Bjerknes, J. (1919). On the structure of moving cyclones, *Monthly Weather Review* **47**(2): 95–99.

Bluestein, H. B. (1992). *Synoptic-dynamic Meteorology in Midlatitudes: Observations and theory of weather systems*, Vol. 2, Taylor & Francis.

Brayshaw, D. J., Hoskins, B. and Blackburn, M. (2008). The storm-track response to idealized sst perturbations in an aquaplanet gcm, *Journal of the Atmospheric Sciences* **65**(9): 2842–2860.

Brennan, M. J., Lackmann, G. M. and Mahoney, K. M. (2008). Potential vorticity (pv) thinking in operations: The utility of nonconservation, *Weather and forecasting* **23**(1): 168–182.

Brogli, R., Lund Sørland, S., Kröner, N. and Schär, C. (2021). Future summer warming pattern under climate change is affected by lapse-rate changes, *Weather and Climate Dynamics* **2**(4): 1093–1110.

Browning, K. (1997). The dry intrusion perspective of extra-tropical cyclone development, *Meteorological Applications* **4**(4): 317–324.

Browning, K. (2004). The sting at the end of the tail: Damaging winds associated with extratropical cyclones, *Quarterly Journal of the Royal Meteorological Society: A journal of the atmospheric sciences, applied meteorology and physical oceanography* **130**(597): 375–399.

Browning, K. A. (1986). Conceptual models of precipitation systems, *Weather and forecasting* **1**(1): 23–41.

Browning, K. A. (1990). Organization of clouds and precipitation in extratropical cyclones, *Extratropical cyclones*, Springer, pp. 129–153.

Büeler, D. and Pfahl, S. (2017). Potential vorticity diagnostics to quantify effects of latent heating in extratropical cyclones. part i: Methodology, *Journal of the Atmospheric Sciences* **74**(11): 3567–3590.

Büeler, D. and Pfahl, S. (2019). Potential vorticity diagnostics to quantify effects of latent heating in extratropical cyclones. part ii: Application to idealized climate change simulations, *Journal of the Atmospheric Sciences* **76**(7): 1885–1902.

Čampa, J. and Wernli, H. (2012). A pv perspective on the vertical structure of mature midlatitude cyclones in the northern hemisphere, *Journal of the atmospheric sciences* **69**(2): 725–740.

Campins, J., Genovés, A., Picornell, M. and Jansà, A. (2011). Climatology of mediterranean cyclones using the era-40 dataset, *International Journal of Climatology* **31**(11): 1596–1614.

Carlson, T. N. (1980). Airflow through midlatitude cyclones and the comma cloud pattern, *Monthly Weather Review* **108**(10): 1498–1509.

Catto, J. (2016). Extratropical cyclone classification and its use in climate studies, *Reviews of Geophysics* **54**(2): 486–520.

Catto, J., Jakob, C., Berry, G. and Nicholls, N. (2012). Relating global precipitation to atmospheric fronts, *Geophysical Research Letters* **39**(10).

Catto, J., Jakob, C. and Nicholls, N. (2015). Can the cmip5 models represent winter frontal precipitation?, *Geophysical Research Letters* **42**(20): 8596–8604.

Catto, J. L., Ackerley, D., Booth, J. F., Champion, A. J., Colle, B. A., Pfahl, S., Pinto, J. G., Quinting, J. F. and Seiler, C. (2019). The future of midlatitude cyclones, *Current Climate Change Reports* **5**(4): 407–420.

Catto, J. L. and Pfahl, S. (2013). The importance of fronts for extreme precipitation, *Journal of Geophysical Research: Atmospheres* **118**(19): 10–791.

Catto, J. L., Shaffrey, L. C. and Hodges, K. I. (2010). Can climate models capture the structure of extratropical cyclones?, *Journal of Climate* **23**(7): 1621–1635.

Chang, E. K., Guo, Y. and Xia, X. (2012). Cmip5 multimodel ensemble projection of storm track change under global warming, *Journal of Geophysical Research: Atmospheres* **117**(D23).

Chang, E. K., Guo, Y., Xia, X. and Zheng, M. (2013). Storm-track activity in ipcc ar4/cmip3 model simulations, *Journal of climate* **26**(1): 246–260.

Chang, E. K., Lee, S. and Swanson, K. L. (2002). Storm track dynamics, *Journal of climate* **15**(16): 2163–2183.

Charney, J. (1955). The use of the primitive equations of motion in numerical prediction, *Tellus* **7**(1): 22–26.

Charney, J. G. (1947). The dynamics of long waves in a baroclinic westerly current, *Journal of the Atmospheric Sciences* **4**(5): 136–162.

Clark, P. A. and Gray, S. L. (2018). Sting jets in extratropical cyclones: A review, *Quarterly Journal of the Royal Meteorological Society* **144**(713): 943–969.

Colle, B. A., Booth, J. F. and Chang, E. K. (2015). A review of historical and future changes of extratropical cyclones and associated impacts along the us east coast, *Current Climate Change Reports* **1**(3): 125–143.

Crezee, B., Joos, H. and Wernli, H. (2017). The microphysical building blocks of low-level potential vorticity anomalies in an idealized extratropical cyclone, *Journal of the Atmospheric Sciences* **74**(5): 1403–1416.

Dacre, H. F. and Gray, S. L. (2013). Quantifying the climatological relationship between extratropical cyclone intensity and atmospheric precursors, *Geophysical Research Letters* **40**(10): 2322–2327.

Dacre, H., Hawcroft, M., Stringer, M. and Hodges, K. (2012). An extratropical cyclone atlas: A tool for illustrating cyclone structure and evolution characteristics, *Bulletin of the American Meteorological Society* **93**(10): 1497–1502.

Davis, C. A. (1992). Piecewise potential vorticity inversion, *Journal of the atmospheric sciences* **49**(16): 1397–1411.

Davis, C. A. and Emanuel, K. A. (1991). Potential vorticity diagnostics of cyclogenesis, *Monthly weather review* **119**(8): 1929–1953.

Day, J. J., Holland, M. M. and Hodges, K. I. (2018). Seasonal differences in the response of arctic cyclones to climate change in cesm1, *Climate dynamics* **50**(9-10): 3885–3903.

Dee, D. P., Uppala, S., Simmons, A., Berrisford, P., Poli, P., Kobayashi, S., Andrae, U., Balmaseda, M., Balsamo, G., Bauer, d. P. et al. (2011). The era-interim reanalysis: Configuration and performance of the data assimilation system, *Quarterly Journal of the royal meteorological society* **137**(656): 553–597.

Deveson, A., Browning, K. and Hewson, T. (2002). A classification of fastex cyclones using a height-attributable quasi-geostrophic vertical-motion diagnostic, *Quarterly Journal of the Royal Meteorological Society: A journal of the atmospheric sciences, applied meteorology and physical oceanography* **128**(579): 93–117.

Dixon, M., Thorpe, A. and Browning, K. (2003). Layer-wise attribution of vertical motion and the influence of potential-vorticity anomalies on synoptic development, *Quarterly Journal of the Royal Meteorological Society: A journal of the atmospheric sciences, applied meteorology and physical oceanography* **129**(591): 1761–1778.

Donat, M. G., Leckebusch, G. C., Pinto, J. G. and Ulbrich, U. (2010). European storminess and associated circulation weather types: future changes deduced from a multi-model ensemble of gcm simulations, *Climate Research* **42**(1): 27–43.

Ertel, H. (1942). Ein neuer hydrodynamischer wirbelsatz, *Met. Z.* **59**: 277–281.

Flaounas, E., Gray, S. L. and Teubler, F. (2021). A process-based anatomy of mediterranean cyclones: from baroclinic lows to tropical-like systems, *Weather and Climate Dynamics* **2**(1): 255–279.

Funatsu, B. M. and Waugh, D. W. (2008). Connections between potential vorticity intrusions and convection in the eastern tropical pacific, *Journal of the atmospheric sciences* **65**(3): 987–1002.

Gastineau, G. and Soden, B. J. (2009). Model projected changes of extreme wind events in response to global warming, *Geophysical Research Letters* **36**(10).

Grams, C. M., Wernli, H., Böttcher, M., Čampa, J., Corsmeier, U., Jones, S. C., Keller, J. H., Lenz, C.-J. and Wiegand, L. (2011). The key role of diabatic processes in modifying the upper-tropospheric wave guide: a north atlantic case-study, *Quarterly Journal of the Royal Meteorological Society* **137**(661): 2174–2193.

Grise, K. M. and Polvani, L. M. (2014). The response of midlatitude jets to increased co2: Distinguishing the roles of sea surface temperature and direct radiative forcing, *Geophysical Research Letters* **41**(19): 6863–6871.

Harley, M. D., Turner, I. L., Kinsela, M. A., Middleton, J. H., Mumford, P. J., Splinter, K. D., Phillips, M. S., Simmons, J. A., Hanslow, D. J. and Short, A. D. (2017). Extreme coastal erosion enhanced by anomalous extratropical storm wave direction, *Scientific reports* **7**(1): 1–9.

Harrold, T. (1973). Mechanisms influencing the distribution of precipitation within baroclinic disturbances, *Quarterly Journal of the Royal Meteorological Society* **99**(420): 232–251.

Hawcroft, M. K., Shaffrey, L. C., Hodges, K. I. and Dacre, H. F. (2016). Can climate models represent the precipitation associated with extratropical cyclones?, *Climate Dynamics* **47**(3): 679–695.

Hawcroft, M., Shaffrey, L., Hodges, K. and Dacre, H. (2012). How much northern hemisphere precipitation is associated with extratropical cyclones?, *Geophysical Research Letters* **39**(24).

Hawcroft, M., Walsh, E., Hodges, K. and Zappa, G. (2018). Significantly increased extreme precipitation expected in europe and north america from extratropical cyclones, *Environmental research letters* **13**(12): 124006.

Hewson, T. D. and Neu, U. (2015). Cyclones, windstorms and the imilast project, *Tellus A: Dynamic Meteorology and Oceanography* **67**(1): 27128.

Hodges, K. (1999). Adaptive constraints for feature tracking, *Monthly Weather Review* **127**(6): 1362–1373.

Holton, J. and Hakim, G. (2012). An introduction to dynamic meteorology, *American Journal of Physics* **88**.

Hoskins, B. (1997). A potential vorticity view of synoptic development, *Meteorological Applications* **4**(4): 325–334.

Hoskins, B. J. and Hodges, K. I. (2002). New perspectives on the northern hemisphere winter storm tracks, *Journal of the Atmospheric Sciences* **59**(6): 1041–1061.

Hoskins, B. J., McIntyre, M. E. and Robertson, A. W. (1985). On the use and significance of isentropic potential vorticity maps, *Quarterly Journal of the Royal Meteorological Society* **111**(470): 877–946.

Hoskins, B. J. and Valdes, P. J. (1990). On the existence of storm-tracks, *Journal of Atmospheric Sciences* **47**(15): 1854–1864.

Hoskins, B., Pedder, M. and Jones, D. W. (2003). The omega equation and potential vorticity, *Quarterly Journal of the Royal Meteorological Society* **129**(595): 3277–3303.

Houze Jr, R. A. (2014). *Cloud dynamics*, Academic press.

IPCC (2014). Climate change 2014: Synthesis report. contribution of working groups i, ii, and iii to the fifth assessment report of the intergovernmental panel on climate change, *Technical report*, [The Core Writing Team, RK Pachauri, L. Meyer (eds.)]. IPCC, Geneva, Switzerland, 151 pp.

Kar-Man Chang, E. (2018). Cmip5 projected change in northern hemisphere winter cyclones with associated extreme winds, *Journal of Climate* **31**(16): 6527–6542.

Kay, J. E., Deser, C., Phillips, A., Mai, A., Hannay, C., Strand, G., Arblaster, J. M., Bates, S., Danabasoglu, G., Edwards, J. et al. (2015). The community earth system model (cesm) large ensemble project: A community resource for studying climate

change in the presence of internal climate variability, *Bulletin of the American Meteorological Society* **96**(8): 1333–1349.

Klawa, M. and Ulbrich, U. (2003). A model for the estimation of storm losses and the identification of severe winter storms in germany, *Natural Hazards and Earth System Sciences* **3**(6): 725–732.

Lackmann, G. (2011). *Midlatitude synoptic meteorology*, American Meteorological Society.

Lackmann, G. M. (2002). Cold-frontal potential vorticity maxima, the low-level jet, and moisture transport in extratropical cyclones, *Monthly Weather Review* **130**(1): 59–74.

Lamarque, J.-F., Bond, T. C., Eyring, V., Granier, C., Heil, A., Klimont, Z., Lee, D., Liousse, C., Mieville, A., Owen, B. et al. (2010). Historical (1850–2000) gridded anthropogenic and biomass burning emissions of reactive gases and aerosols: methodology and application, *Atmospheric Chemistry and Physics* **10**(15): 7017–7039.

Lamarque, J.-F., Kyle, G. P., Meinshausen, M., Riahi, K., Smith, S. J., van Vuuren, D. P., Conley, A. J. and Vitt, F. (2011). Global and regional evolution of short-lived radiatively-active gases and aerosols in the representative concentration pathways, *Climatic change* **109**(1-2): 191.

Laurila, T. K., Gregow, H., Cornér, J. and Sinclair, V. A. (2021). Characteristics of extratropical cyclones and precursors to windstorms in northern europe, *Weather and Climate Dynamics* **2**(4): 1111–1130.

Leckebusch, G. C., Koffi, B., Ulbrich, U., Pinto, J. G., Spangehl, T. and Zacharias, S. (2006). Analysis of frequency and intensity of european winter storm events from a multi-model perspective, at synoptic and regional scales, *Climate Research* **31**(1): 59–74.

Leckebusch, G. C. and Ulbrich, U. (2004). On the relationship between cyclones and extreme windstorm events over europe under climate change, *Global and planetary change* **44**(1-4): 181–193.

Li, M., Woollings, T., Hodges, K. and Masato, G. (2014). Extratropical cyclones in a warmer, moister climate: A recent atlantic analogue, *Geophysical Research Letters* **41**(23): 8594–8601.

Li, Z. and O'Gorman, P. A. (2020). Response of vertical velocities in extratropical precipitation extremes to climate change, *Journal of Climate* **33**(16): 7125–7139.

Lin, N., Marsooli, R. and Colle, B. A. (2019). Storm surge return levels induced by mid-to-late-twenty-first-century extratropical cyclones in the northeastern united states, *Climatic change* **154**(1): 143–158.

Liu, X., Liu, Y., Wang, X. and Wu, G. (2020). Large-scale dynamics and moisture sources of the precipitation over the western tibetan plateau in boreal winter, *Journal of Geophysical Research: Atmospheres* **125**(9): e2019JD032133.

Madonna, E., Wernli, H., Joos, H. and Martius, O. (2014). Warm conveyor belts in the era-interim dataset (1979–2010). part i: Climatology and potential vorticity evolution, *Journal of climate* **27**(1): 3–26.

Marciano, C. G., Lackmann, G. M. and Robinson, W. A. (2015). Changes in us east coast cyclone dynamics with climate change, *Journal of Climate* **28**(2): 468–484.

Martin, J. E. (1998). The structure and evolution of a continental winter cyclone. part i: Frontal structure and the occlusion process, *Monthly weather review* **126**(2): 303–328.

Martin, J. E. (2006). *Mid-latitude atmospheric dynamics: a first course*, John Wiley & Sons.

Martínez-Alvarado, O., Gray, S. L., Hart, N. C., Clark, P. A., Hodges, K. and Roberts, M. J. (2018). Increased wind risk from sting-jet windstorms with climate change, *Environmental research letters* **13**(4): 044002.

Martínez-Alvarado, O., Joos, H., Chagnon, J., Boettcher, M., Gray, S., Plant, R., Methven, J. and Wernli, H. (2014). The dichotomous structure of the warm conveyor belt, *Quarterly Journal of the Royal Meteorological Society* **140**(683): 1809–1824.

Martius, O., Pfahl, S. and Chevalier, C. (2016). A global quantification of compound precipitation and wind extremes, *Geophysical Research Letters* **43**(14): 7709–7717.

Mbengue, C. and Schneider, T. (2013). Storm track shifts under climate change: What can be learned from large-scale dry dynamics, *Journal of Climate* **26**(24): 9923–9930.

McTaggart-Cowan, R., Gyakum, J. and Yau, M. (2003). Moist component potential vorticity, *Journal of the atmospheric sciences* **60**(1): 166–177.

Meinshausen, M., Smith, S. J., Calvin, K., Daniel, J. S., Kainuma, M., Lamarque, J.-F., Matsumoto, K., Montzka, S., Raper, S., Riahi, K. et al. (2011). The rcp greenhouse gas concentrations and their extensions from 1765 to 2300, *Climatic change* **109**(1-2): 213.

Messmer, M., Raible, C. C. and Gómez-Navarro, J. J. (2020). Impact of climate change on the climatology of vb cyclones, *Tellus A: Dynamic Meteorology and Oceanography* **72**(1): 1–18.

Michaelis, A. C., Willison, J., Lackmann, G. M. and Robinson, W. A. (2017). Changes in winter north atlantic extratropical cyclones in high-resolution regional pseudo–global warming simulations, *Journal of Climate* **30**(17): 6905–6925.

Mölter, T., Schindler, D., Albrecht, A. T. and Kohnle, U. (2016). Review on the projections of future storminess over the north atlantic european region, *Atmosphere* **7**(4): 60.

Moon, W., Manucharyan, G. E. and Dijkstra, H. A. (2022). Baroclinic instability and large-scale wave propagation on planetary-scale atmosphere, *Quarterly Journal of the Royal Meteorological Society* .

Müller, A., Niedrich, B. and Névir, P. (2020). Three-dimensional potential vorticity structures for extreme precipitation events on the convective scale, *Tellus A: Dynamic Meteorology and Oceanography* **72**(1): 1–20.

Neu, U., Akperov, M. G., Bellenbaum, N., Benestad, R., Blender, R., Caballero, R., Cocozza, A., Dacre, H. F., Feng, Y., Fraedrich, K. et al. (2013). Imilast: A community effort to intercompare extratropical cyclone detection and tracking algorithms, *Bulletin of the American Meteorological Society* **94**(4): 529–547.

Nie, J., Sobel, A. H., Shaevitz, D. A. and Wang, S. (2018). Dynamic amplification of extreme precipitation sensitivity, *Proceedings of the National Academy of Sciences* **115**(38): 9467–9472.

Norris, J., Chen, G. and Neelin, J. D. (2019). Thermodynamic versus dynamic controls on extreme precipitation in a warming climate from the community earth system model large ensemble, *Journal of Climate* **32**(4): 1025–1045.

O'Gorman, P. A. (2010). Understanding the varied response of the extratropical storm tracks to climate change, *Proceedings of the National Academy of Sciences* **107**(45): 19176–19180.

O'Gorman, P. A. and Schneider, T. (2008). Energy of midlatitude transient eddies in idealized simulations of changed climates, *Journal of climate* **21**(22): 5797–5806.

O'Gorman, P. A. and Schneider, T. (2009). The physical basis for increases in precipitation extremes in simulations of 21st-century climate change, *Proceedings of the National Academy of Sciences* **106**(35): 14773–14777.

Pfahl, S., Madonna, E., Boettcher, M., Joos, H. and Wernli, H. (2014). Warm conveyor belts in the era-interim dataset (1979–2010). part ii: Moisture origin and relevance for precipitation, *Journal of Climate* **27**(1): 27–40.

Pfahl, S., O'Gorman, P. A. and Fischer, E. M. (2017). Understanding the regional pattern of projected future changes in extreme precipitation, *Nature Climate Change* **7**(6): 423–427.

Pfahl, S., O'gorman, P. A. and Singh, M. S. (2015). Extratropical cyclones in idealized simulations of changed climates, *Journal of Climate* **28**(23): 9373–9392.

Pfahl, S. and Sprenger, M. (2016). On the relationship between extratropical cyclone precipitation and intensity, *Geophysical Research Letters* **43**(4): 1752–1758.

Pfahl, S. and Wernli, H. (2012). Quantifying the relevance of cyclones for precipitation extremes, *Journal of Climate* **25**(19): 6770–6780.

Phibbs, S. and Toumi, R. (2016). The dependence of precipitation and its footprint on atmospheric temperature in idealized extratropical cyclones, *Journal of Geophysical Research: Atmospheres* **121**(15): 8743–8754.

Pinto, J. G., Bellenbaum, N., Karremann, M. K. and Della-Marta, P. M. (2013). Serial clustering of extratropical cyclones over the north atlantic and europe under recent and future climate conditions, *Journal of geophysical research: Atmospheres* **118**(22): 12–476.

Pinto, J. G., Gómara, I., Masato, G., Dacre, H. F., Woollings, T. and Caballero, R. (2014). Large-scale dynamics associated with clustering of extratropical cyclones affecting western europe, *Journal of Geophysical Research: Atmospheres* **119**(24): 13–704.

Pinto, J. G. and Ludwig, P. (2020). Extratropical cyclones over the north atlantic and western europe during the last glacial maximum and implications for proxy interpretation, *Climate of the Past* **16**(2): 611–626.

Pinto, J. G., Ulbrich, U., Leckebusch, G., Spangehl, T., Reyers, M. and Zacharias, S. (2007). Changes in storm track and cyclone activity in three sres ensemble experiments with the echam5/mpi-om1 gcm, *Climate Dynamics* **29**(2): 195–210.

Pinto, J. G., Zacharias, S., Fink, A. H., Leckebusch, G. C. and Ulbrich, U. (2009). Factors contributing to the development of extreme north atlantic cyclones and their relationship with the nao, *Climate dynamics* **32**(5): 711–737.

Pithan, F., Shepherd, T. G., Zappa, G. and Sandu, I. (2016). Climate model biases in jet streams, blocking and storm tracks resulting from missing orographic drag, *Geophysical Research Letters* **43**(13): 7231–7240.

Priestley, M. D. K. and Catto, J. L. (2022). Future changes in the extratropical storm tracks and cyclone intensity, wind speed, and structure, *Weather and Climate Dynamics* **3**(1): 337–360.
URL: *https://wcd.copernicus.org/articles/3/337/2022/*

Raible, C. C., Messmer, M., Lehner, F., Stocker, T. F. and Blender, R. (2018). Extratropical cyclone statistics during the last millennium and the 21st century, *Climate of the Past* **14**(10): 1499–1514.

Räisänen, J. (1995). Factors affecting synoptic-scale vertical motions: A statistical study using a generalized omega equation, *Monthly weather review* **123**(8): 2447–2460.

Rantanen, M., Räisänen, J., Lento, J., Stepanyuk, O., Räty, O., Sinclair, V. A. and Järvinen, H. (2017). Ozo v. 1.0: software for solving a generalised omega equation and the zwack–okossi height tendency equation using wrf model output, *Geosci. Model Dev* **10**: 827–841.

Raveh-Rubin, S. (2017). Dry intrusions: Lagrangian climatology and dynamical impact on the planetary boundary layer, *Journal of Climate* **30**(17): 6661–6682.

Raveh-Rubin, S. and Wernli, H. (2016). Large-scale wind and precipitation extremes in the mediterranean: dynamical aspects of five selected cyclone events, *Quarterly Journal of the Royal Meteorological Society* **142**(701): 3097–3114.

Reboita, M. S., Reale, M., da Rocha, R. P., Giorgi, F., Giuliani, G., Coppola, E., Nino, R. B. L., Llopart, M., Torres, J. A. and Cavazos, T. (2021). Future changes in the wintertime cyclonic activity over the cordex-core southern hemisphere domains in a multi-model approach, *Climate Dynamics* **57**(5): 1533–1549.

Rivière, G., Gilet, J.-B. and Oruba, L. (2013). Understanding the regeneration stage undergone by surface cyclones crossing a midlatitude jet in a two-layer model, *Journal of the atmospheric sciences* **70**(9): 2832–2853.

Roberts, J., Champion, A., Dawkins, L., Hodges, K., Shaffrey, L., Stephenson, D., Stringer, M., Thornton, H. and Youngman, B. (2014). The xws open access catalogue of extreme european windstorms from 1979 to 2012, *Natural Hazards and Earth System Sciences* **14**(9): 2487–2501.

Schemm, S. and Wernli, H. (2014). The linkage between the warm and the cold conveyor belts in an idealized extratropical cyclone, *Journal of the Atmospheric Sciences* **71**(4): 1443–1459.

Schielicke, L. (2017). *Scale-dependent identification and statistical analysis of atmospheric vortex structures in theory, model and observation*, PhD thesis, Freie Universität Berlin.

Schielicke, L., Névir, P. and Ulbrich, U. (2016). Kinematic vorticity number–a tool for estimating vortex sizes and circulations, *Tellus A: Dynamic Meteorology and Oceanography* **68**(1): 29464.

Schneider, T., O'Gorman, P. A. and Levine, X. J. (2010). Water vapor and the dynamics of climate changes, *Reviews of Geophysics* **48**(3).

Schultz, D. M. (2001). Reexamining the cold conveyor belt, *Monthly Weather Review* **129**(9): 2205–2225.

Schultz, D. M., Bosart, L. F., Colle, B. A., Davies, H. C., Dearden, C., Keyser, D., Martius, O., Roebber, P. J., Steenburgh, W. J., Volkert, H. et al. (2019). Extratropical cyclones: a century of research on meteorology's centerpiece, *Meteorological monographs* **59**: 16–1.

Seiler, C. (2019). A climatological assessment of intense extratropical cyclones from the potential vorticity perspective, *Journal of Climate* **32**(8): 2369–2380.

Seiler, C., Zwiers, F., Hodges, K. I. and Scinocca, J. (2018). How does dynamical downscaling affect model biases and future projections of explosive extratropical cyclones along north america's atlantic coast?, *Climate dynamics* **50**(1): 677–692.

Sepp, M. and Jaagus, J. (2011). Changes in the activity and tracks of arctic cyclones, *Climatic Change* **105**(3): 577–595.

Shapiro, M. A. and Keyser, D. (1990). Fronts, jet streams and the tropopause, *Extratropical cyclones*, Springer, pp. 167–191.

Shaw, T., Baldwin, M., Barnes, E., Caballero, R., Garfinkel, C., Hwang, Y.-T., Li, C., O'Gorman, P., Rivière, G., Simpson, I. et al. (2016). Storm track processes and the opposing influences of climate change, *Nature Geoscience* **9**(9): 656.

Sherwood, S., Roca, R., Weckwerth, T. and Andronova, N. (2010). Tropospheric water vapor, convection, and climate, *Reviews of Geophysics* **48**(2).

Simmons, A., Untch, A., Jakob, C., Kållberg, P. and Unden, P. (1999). Stratospheric water vapour and tropical tropopause temperatures in ecmwf analyses and multi-year simulations, *Quarterly Journal of the Royal Meteorological Society* **125**(553): 353–386.

Sinclair, V., Rantanen, M., Haapanala, P., Räisänen, J., Järvinen, H. et al. (2020). The characteristics and structure of extra-tropical cyclones in a warmer climate, *Weather and Climate Dynamics* .

Singh, M. S. and O'Gorman, P. A. (2013). Influence of entrainment on the thermal stratification in simulations of radiative-convective equilibrium, *Geophysical Research Letters* **40**(16): 4398–4403.

Škerlak, B. (2014). *Climatology and process studies of tropopause folds, cross-tropopause exchange, and transport into the boundary layer*, PhD thesis, ETH Zurich.

Slater, T. P., Schultz, D. M. and Vaughan, G. (2015). Acceleration of near-surface strong winds in a dry, idealised extratropical cyclone, *Quarterly Journal of the Royal Meteorological Society* **141**(689): 1004–1016.

Slater, T. P., Schultz, D. M. and Vaughan, G. (2017). Near-surface strong winds in a marine extratropical cyclone: acceleration of the winds and the importance of surface fluxes, *Quarterly Journal of the Royal Meteorological Society* **143**(702): 321–332.

Sprenger, M., Fragkoulidis, G., Binder, H., Croci-Maspoli, M., Graf, P., Grams, C. M., Knippertz, P., Madonna, E., Schemm, S., Škerlak, B. et al. (2017). Global climatologies of eulerian and lagrangian flow features based on era-interim, *Bulletin of the American Meteorological Society* **98**(8): 1739–1748.

Sprenger, M. and Wernli, H. (2015). The lagranto lagrangian analysis tool–version 2.0, *Geoscientific Model Development* **8**(8): 2569–2586.

Steinfeld, D. (2019). *The role of latent heating in atmospheric blocking: climatology and numerical experiments*, PhD thesis, ETH Zurich.

Steinfeld, D., Boettcher, M., Forbes, R. and Pfahl, S. (2020). The sensitivity of atmospheric blocking to upstream latent heating–numerical experiments, *Weather and Climate Dynamics* **1**(2): 405–426.

Steinfeld, D. and Pfahl, S. (2019). The role of latent heating in atmospheric blocking dynamics: a global climatology, *Climate Dynamics* **53**(9): 6159–6180.

Stoelinga, M. T. (1996). A potential vorticity-based study of the role of diabatic heating and friction in a numerically simulated baroclinic cyclone, *Monthly weather review* **124**(5): 849–874.

Sugiyama, M., Shiogama, H. and Emori, S. (2010). Precipitation extreme changes exceeding moisture content increases in miroc and ipcc climate models, *Proceedings of the National Academy of Sciences* **107**(2): 571–575.

Tamarin-Brodsky, T. and Kaspi, Y. (2017). Enhanced poleward propagation of storms under climate change, *Nature geoscience* **10**(12): 908–913.

Tamarin, T. and Kaspi, Y. (2016). The poleward motion of extratropical cyclones from a potential vorticity tendency analysis, *Journal of the Atmospheric Sciences* **73**(4): 1687–1707.

Tamarin, T. and Kaspi, Y. (2017). The poleward shift of storm tracks under global warming: A lagrangian perspective, *Geophysical Research Letters* **44**(20): 10–666.

Teubler, F. and Riemer, M. (2016). Dynamics of rossby wave packets in a quantitative potential vorticity–potential temperature framework, *Journal of the Atmospheric Sciences* **73**(3): 1063–1081.

Tochimoto, E. and Niino, H. (2016). Structural and environmental characteristics of extratropical cyclones that cause tornado outbreaks in the warm sector: A composite study, *Monthly Weather Review* **144**(3): 945–969.

Tous, M., Zappa, G., Romero, R., Shaffrey, L. and Vidale, P. L. (2016). Projected changes in medicanes in the hadgem3 n512 high-resolution global climate model, *Climate Dynamics* **47**(5-6): 1913–1924.

Ulbrich, U., Leckebusch, G. C., Grieger, J., Schuster, M., Akperov, M., Bardin, M. Y., Feng, Y., Gulev, S., Inatsu, M., Keay, K. et al. (2013). Are greenhouse gas signals of northern hemisphere winter extra-tropical cyclone activity dependent on the identification and tracking algorithm?, *Meteorologische Zeitschrift* **22**(1): 61–68.

Ulbrich, U., Leckebusch, G. and Pinto, J. G. (2009). Extra-tropical cyclones in the present and future climate: a review, *Theoretical and Applied Climatology* **96**(1-2): 117–131.

Wernli, B. H. and Davies, H. C. (1997). A lagrangian-based analysis of extratropical cyclones. i: The method and some applications, *Quarterly Journal of the Royal Meteorological Society* **123**(538): 467–489.

Wernli, H., Dirren, S., Liniger, M. A. and Zillig, M. (2002). Dynamical aspects of the life cycle of the winter storm 'lothar'(24–26 december 1999), *Quarterly Journal of the Royal Meteorological Society: A journal of the atmospheric sciences, applied meteorology and physical oceanography* **128**(580): 405–429.

Wernli, H. and Schwierz, C. (2006). Surface cyclones in the era-40 dataset (1958–2001). part i: Novel identification method and global climatology, *Journal of the atmospheric sciences* **63**(10): 2486–2507.

Willison, J., Robinson, W. A. and Lackmann, G. M. (2013). The importance of resolving mesoscale latent heating in the north atlantic storm track, *Journal of the Atmospheric Sciences* **70**(7): 2234–2250.

Willison, J., Robinson, W. A. and Lackmann, G. M. (2015). North atlantic storm-track sensitivity to warming increases with model resolution, *Journal of Climate* **28**(11): 4513–4524.

Yettella, V. and Kay, J. E. (2017). How will precipitation change in extratropical cyclones as the planet warms? insights from a large initial condition climate model ensemble, *Climate Dynamics* **49**(5-6): 1765–1781.

Zappa, G. (2019). Regional climate impacts of future changes in the mid–latitude atmospheric circulation: a storyline view, *Current Climate Change Reports* **5**(4): 358–371.

Zappa, G., Shaffrey, L. C., Hodges, K. I., Sansom, P. G. and Stephenson, D. B. (2013). A multimodel assessment of future projections of north atlantic and european extratropical cyclones in the cmip5 climate models, *Journal of Climate* **26**(16): 5846–5862.

Zhang, Z. and Colle, B. A. (2018). Impact of dynamically downscaling two cmip5 models on the historical and future changes in winter extratropical cyclones along the east coast of north america, *Journal of Climate* **31**(20): 8499–8525.

Acknowledgments

I would like to thank Prof. Stephan Pfahl for giving me the opportunity to work in his group and I also thank him for the guidance, the hours of discussion and the comments on my project. I thank Dr. Franzi Teubler for sharing me her PPVI code and her availability to discuss my results. Thanks to Dr. Micheal Sprenger for providing the code for post-processing and evaluation of cyclone dynamics. I am grateful to Urs Beyerle (ETH Zurich) for performing the CESM-LE reruns. I acknowledge the HPC service of ZEDAT, Freie Universität Berlin, for providing computational resources. I am very grateful to Prof. Joaquim Pinto for acting as external referee of my thesis.

I thank Dr. Lisa Schielicke for all the hints and comments during my Ph.D. I also thank Patricia Margerison for all the support, kindness and understanding before and when I arrived in Berlin, thanks for helping me settle in Berlin. I thank my colleagues at the Institute of Meteorology for always being open to talk, support and invite me to having lunch, Thomas, Gregor, Joschua, Ingo, Oscar, Jana, Florian, George, Patrick, Angela thank you!

I thank my family, Narciso, Juve, Ana, Arendy for always trusting and supporting me. I would like to thank Karen for encouraging me to keep going and for her patience. I thank my friends in Germany and in Mexico, for making this path easier, with talks and healthy meetings, Ale, Ana Ceres, Dani, Carlos, Raúl, Franzi, Oscar, Martha, Ana Karen thank you!

Declaration of authorship

I hereby declare that the report submitted is my own unaided work. All direct or indirect sources used are acknowledged as references. I am aware that the Thesis in digital form can be examined for the use of unauthorized aid and in order to determine whether the report as a whole or parts incorporated in it may be deemed as plagiarism. For the comparison of my work with existing sources I agree that it shall be entered in a database where it shall also remain after examination, to enable comparison with future Theses submitted. Further rights of reproduction and usage, however, are not granted here. This paper was not previously presented to another examination board and has not been published.

Berlin,

Edgar Dolores Tesillos